Summer 2012

# Analysis of retinal vessel networks using quantitative descriptors of vascular morphology

Vinayak Shivkumar Joshi
*University of Iowa*

# ANALYSIS OF RETINAL VESSEL NETWORKS USING QUANTITATIVE DESCRIPTORS OF VASCULAR MORPHOLOGY

by

Vinayak Shivkumar Joshi

An Abstract

Of a thesis submitted in partial fulfillment of the
requirements for the Doctor of Philosophy
degree in Biomedical Engineering
in the Graduate College of
The University of Iowa

July 2012

Thesis Supervisor: Professor Michael D. Abràmoff
Professor Joseph M. Reinhardt

## ABSTRACT

Abnormalities in the vascular pattern of a retina, such as morphologic changes in vessel shape, branching pattern, width, tortuosity, or the appearance of retinal lesions, may be associated with the occurrence of retinopathies or cardiovascular diseases. Thus, an automated quantitative analysis of changes in vessel morphology may help indicating the clinical signs of aforementioned retinopathies, describing their early occurrence or severity. The responses obtained from different types of retinal vessels, i.e., arteries and veins, may be variable to retinopathies and their measurement may lead to a more precise diagnosis compared to that by the average response accounted for the entire vessel network.

I propose a set of automated methods in order to analyze the retinal vessel network and to quantify its morphologic properties with respect to arteries and veins, in two-dimensional color fundus images. The analytical methods include; 1) Formation of a well connected vessel network, 2) Structural mapping of a vessel network, 3) Artery-venous classification, and 4) Blood vessel hemorrhage detection. The quantification methods include vessel morphology analysis based on the measurement of tortuosity, width, branching angle, branching coefficient, and fractal dimension. The aforementioned morphologic parameters are measured with respect to arteries and veins separately in a vessel network. The methods are validated with the manually annotated retinal fundus images as a ground truth.

The major contribution of this thesis includes the development of automated

methods for; 1) Identification and separation of retinal vessel trees for individual vessel analysis, 2) Automated quantification of morphologic characteristics of retinal vessels for quick and precise measurement, 3) Automated quantification of vessel morphology with respect to arteries and veins, and 4) Analysis of two datasets, a) malarial retinopathy subject dataset, b) longitudinal study dataset.

The ability of the automated methods to quantify the retinal vessel specific properties may enable the individual vessel analysis as an alternative to a time-consuming and subjective clinical evaluation, or to a quantitative morphology characterization averaged over the entire vessel network. The objective evaluation may indicate the progression of retinopathies precisely and may help characterizing normal and abnormal vascular patterns with respect to arteries and veins. This may enable a quick diagnosis, treatment availability, prognosis, and facilitation of clinical health-care procedures in remote areas.

Abstract Approved: _____
Thesis Supervisor

_____
Title and Department

_____
Date

# ANALYSIS OF RETINAL VESSEL NETWORKS USING QUANTITATIVE DESCRIPTORS OF VASCULAR MORPHOLOGY

by

Vinayak Shivkumar Joshi

A thesis submitted in partial fulfillment of the
requirements for the Doctor of Philosophy
degree in Biomedical Engineering
in the Graduate College of
The University of Iowa

July 2012

Thesis Supervisor: Professor Michael D. Abràmoff
Professor Joseph M. Reinhardt

Graduate College
The University of Iowa
Iowa City, Iowa

CERTIFICATE OF APPROVAL

---

PH.D. THESIS

---

This is to certify that the Ph.D. thesis of

Vinayak Shivkumar Joshi

has been approved by the Examining Committee for the thesis requirement for the Doctor of Philosophy degree in Biomedical Engineering at the July 2012 graduation.

Thesis Committee: _____
Michael D. Abràmoff, Thesis Supervisor

_____
Joseph M. Reinhardt

_____
Mona K. Garvin

_____
Todd E. Scheetz

_____
Edwin L. Dove

## ACKNOWLEDGEMENTS

First of all, I would like to thank my advisors, Dr. Joseph Reinhardt and Dr. Michael Abràmoff for their patient guidance and valuable support throughout my study. I am greatly indebted to them for their inspiring and encouraging words and the wealth of brilliant ideas they provided during the research. I truly appreciate the help from Dr. Mona Garvin, who offered a valuable guidance in utilizing the graph algorithm knowledge into a retinal image analysis, owing to her experience and expertise. I would like to thank Dr. Todd Scheetz and Dr. Edwin Dove for their brilliant research ideas and the continued guidance throughout the program. I am grateful to Dr. Richard Maude for providing the malarial retinopathy image dataset, and a guidance in automated malarial retinopathy detection study. I would like to thank my colleague Mr. Mark Christopher for offering a great help with the ground truth generation for the validation purpose. I successfully utilized the 'Truthmarker software' designed by him for the manual annotation of retinal images. I am also thankful to Ms. Salma Bengali for providing a valuable help with the ground truth generation. In addition, I would like to thank Dr. Milan Sonka and Dr. Punam Saha for their valuable suggestions for my research.

This research was funded by the Veterans Administration Center of Excellence for Prevention and Treatment of Visual Loss, NIH grants EY017066 and EB004640, the University of Iowa and Research to Prevent Blindness, NY, Department of Veterans Affairs, Iowa city, Iowa. The malarial retinopathy image data collection was

funded by a Research Fellowship from the British Infection Society (RJM) and the Wellcome Trust of Great Britain (grant number 077166/Z/05/Z).

I enjoyed working with my colleague Dr. Xiayu Xu and discussing different ophthalmic research aspects with her. I would like to thank her for the valuable contribution to my research through the bright research ideas and a necessary help. I am also grateful to Dr. Sangyeol Lee for his guidance on retinal image registration and analysis. Thanks to my labmates Kai Ding, Tarunashree Yavarna, PanFang Hua, KaiFang Du, Sandeep Boddu, Richard Amendola, for being helpful and kind.

Finally, last but not the least, I would like to extend special thanks to my parents, Maya Joshi and Shivkumar Joshi, and my sister Prajaktaa Gore, for their love and support throughout this process.

I am also thankful to the people whom I did not mention, but have a valuable contribution in this research.

## ABSTRACT

Abnormalities in the vascular pattern of a retina, such as morphologic changes in vessel shape, branching pattern, width, tortuosity, or the appearance of retinal lesions, may be associated with the occurrence of retinopathies or cardiovascular diseases. Thus, an automated quantitative analysis of changes in vessel morphology may help indicating the clinical signs of aforementioned retinopathies, describing their early occurrence or severity. The responses obtained from different types of retinal vessels, i.e., arteries and veins, may be variable to retinopathies and their measurement may lead to a more precise diagnosis compared to that by the average response accounted for the entire vessel network.

I propose a set of automated methods in order to analyze the retinal vessel network and to quantify its morphologic properties with respect to arteries and veins, in two-dimensional color fundus images. The analytical methods include; 1) Formation of a well connected vessel network, 2) Structural mapping of a vessel network, 3) Artery-venous classification, and 4) Blood vessel hemorrhage detection. The quantification methods include vessel morphology analysis based on the measurement of tortuosity, width, branching angle, branching coefficient, and fractal dimension. The aforementioned morphologic parameters are measured with respect to arteries and veins separately in a vessel network. The methods are validated with the manually annotated retinal fundus images as a ground truth.

The major contribution of this thesis includes the development of automated

methods for; 1) Identification and separation of retinal vessel trees for individual vessel analysis, 2) Automated quantification of morphologic characteristics of retinal vessels for quick and precise measurement, 3) Automated quantification of vessel morphology with respect to arteries and veins, and 4) Analysis of two datasets, a) malarial retinopathy subject dataset, b) longitudinal study dataset.

The ability of the automated methods to quantify the retinal vessel specific properties may enable the individual vessel analysis as an alternative to a time-consuming and subjective clinical evaluation, or to a quantitative morphology characterization averaged over the entire vessel network. The objective evaluation may indicate the progression of retinopathies precisely and may help characterizing normal and abnormal vascular patterns with respect to arteries and veins. This may enable a quick diagnosis, treatment availability, prognosis, and facilitation of clinical health-care procedures in remote areas.

## TABLE OF CONTENTS

## LIST OF TABLES

Table

## LIST OF FIGURES

Figure

# CHAPTER 1
# INTRODUCTION

## 1.1 Physiology of a retina

To study the effects of retinopathies and other systemic diseases on the retina and its vasculature, one needs to understand the detailed architecture of retina and ocular structures. The schematic (Fig. 1.1(a)) shows different ocular structures and retina which is positioned on the back side of the eye, covering it from inside. Retinal membrane consists of nerve cells which are sensitive to light and are classified into two types, viz., rods and cones. The nerve cells are the mediators between optical signals received at the retina, and part of the central nervous system dealing with the visual senses. Rod cells are responsible for black and white vision, the peripheral vision and the vision in dim lighting conditions, whereas the cone cells deal with both black/white and the color vision. Cones are present in the ocular structure known as

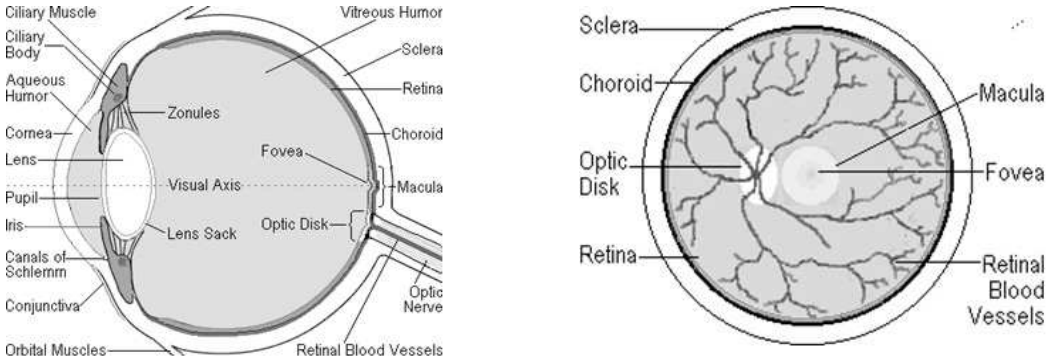


Figure 1.1: The eye: a) Side view, [1], b) Rear view, [1]

fovea, which develops the high visual acuity in the central vision [1][13].

The retinal vasculature (Fig. 1.1(b)) and the neuronal network organized on the retina are responsible for blood circulation in the inner retina and nervous system signal transmission, respectively. Development of a vasculature on the retina is dependent upon the growth of ocular structures and nervous system during the embryonic stage, along with the oxygen requirements and presence of vasoactive growth factors such as VEGF [14].

The retinopathies or the diseases may affect the retina through the abnormal blood circulation in the vasculature. These diseases are mainly classified into two types: Retinal abnormalities which may be accounted as ischemic diseases, vessel occlusions, hemodynamic diseases, retinal stresses, radiation damages and inflammation [15]. The other type is regarded as the causes of abnormal blood circulation produced in the retina due to the systemic dysfunctions. Metabolic behaviors which get affected through diseases such as diabetes, hypertension, cardiovascular diseases, cancers and blood infections, produce detrimental effects on the entire system including the retina and its circulation [1][13][16].

## 1.2 Retinal disorders (Retinopathies)

### 1.2.1 Diabetic retinopathy

Diabetes mellitus affects large content of population in United States every year. It is a systemic disease which also affects the retinal vasculature leading to a retinopathy called diabetic retinopathy (DR). According to recent statistics, the number of patients affected with DR reached 23 million in year 2007 in United States

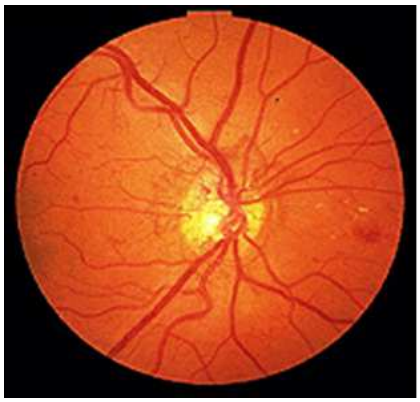

Figure 1.2: Fundus image of a patient with diabetic retinopathy [2]

population. Diabetes is defined as the inability of metabolic system to control the blood sugar levels appropriately which results into a hyperglycemia. Since the microvascular structures in the retina are vulnerable to high blood sugar levels, they are severely damaged. The pericyte cells which support the vessel walls die and vessel walls become fragile and permeable [1] [2].

There are two stages of diabetic retinopathy. The primary stage is called non-proliferative DR and the secondary or advanced stage is known as proliferative DR [16].

During the non-proliferative (NPDR) stage, the retinal blood vessels cannot withstand the high concentration of glucose and other sugars such as fructose in the blood, and get damaged. It significantly damages the mural cells which form an interior lining of vessels, the basement membrane and endothelial cell lining, all of which help forming a blood retinal barrier and prevent the leakage of blood. Due to the deterioration of mural cells and endothelial lining, blood vessel walls become

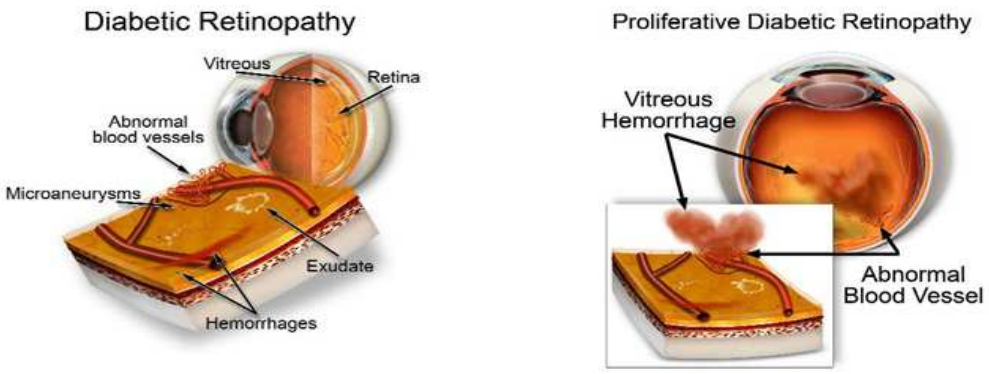


Figure 1.3: DR: a) Non-proliferative [3], b) Proliferative [3]

fragile and ultimately break down or leak. Leakage from blood vessels may lead to various pathological conditions like blood hemorrhages, lipid and protein fluid leakage or deposits known as hard exudates, accumulation of fluid called edema, and a capillary blockage called cotton wool spots. It may also form tiny capillary wall swellings known as microaneurysms, which may be a strong indicator of diabetic retinopathy [3][14]. It may result into a formation of scar tissues which cause retinal detachment by contraction or retinal traction [1][13][16][17]. Fig. 1.3(a) shows various conditions resulting from non-proliferative diabetic retinopathy.

Non-proliferative DR conditions advance to a Proliferative DR (PDR) stage, resulting into retinal ischemia and hence the poor nourishment of retina. Due to the regulatory responses exhibited by body, the unnourished areas send the nourishment signals for the oxygen supply, may be in terms of growth factors such as VEGF. It results into a development of new blood vessels on the retina by the process known as Neovascularization [3][16][17].

The new blood vessels formed in this process are not normal but are weak and fragile. They may form on the retinal surface or sometimes on the ocular structure known as an iris, in the vitreous humour. These blood vessels may break down, leak or bleed and may result into a fibrovascular proliferation (Fig. 1.3(b)). It forms the scar tissues which may cause the retinal detachment. When these vessels form on the iris (rubeosis) [3], they can block the filter responsible for the fluid drainage from the eye. It causes the pressure increase inside the eye resulting into a secondary or a neovascular glaucoma causing blindness [13][14][18].

### 1.2.2 Retinopathy of prematurity

The retinopathies discussed so far are known to be caused due to the environmental factors. Some of the retinal diseases are congenital which are present on the retina right at the birth. Retinopathy of prematurity (ROP) or the retrolental fibroplasia (RLF), is one of the congenital diseases observed in premature babies. Other factors which contribute to the progress of ROP are anemia, respiratory problems, blood transfusions and low birth weight [16].

Normally the retinal development occurs in in-utero and in-term, and the development is completed at birth or in couple more weeks after the birth. But in case of pre-term infants, the retinal development is not completed at the birth time and the vascularization is hampered before the full growth. The retinal vessel growth is disorganized and then develops abnormally (Fig. 1.4(a)). Since the blood vessel growth is stopped pre-maturely, the peripheral retina is deficient of oxygen and nutrients, and the body supports the growth of new blood vessels (neovascularization) as a recovery

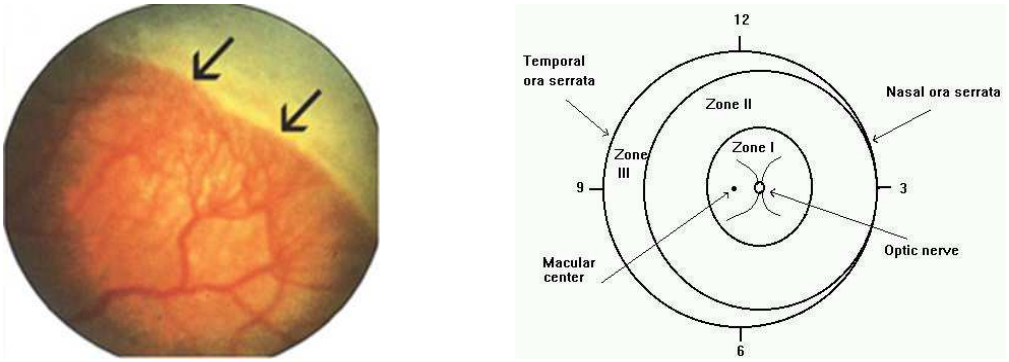


Figure 1.4: ROP: a) ROP signs [4], b) ICROP classification system [1]

mechanism [4]. These blood vessels are abnormal and may result into a fibrovascular proliferation. They leak or bleed and may produce scars and fibrous tissues on the retina. These scars may pull the retina out, causing the retinal detachment.

The International Classification of Retinopathy of Prematurity (ICROP) is the classification system developed for ROP which determines the severity stages of ROP and its progression. It considers several factors such as the disease location in zones (I,II,III) (Fig. 1.4(b)), disease severity in stages from 1 to 5, the circumferential expansion of ROP in terms of clock hours (1-12), and the progression of a plus disease [16]. The presence of a plus disease can be detected by the increased vessel dilatation and tortuosity near to the posterior pole of retina, which may suggest the increased blood flow in the retinal circulation, and confirm the ROP status [1].

### 1.2.3 Malarial retinopathy

#### 1.2.3.1 Rationale behind the malarial retinopathy diagnosis

A relatively higher proportion of misdiagnosis of cerebral malaria (CM) and the associated diseases is the most prevalent cause of mortality in African children in countries such as Ghana, Gambia, Malawi, Kenya and parts of Asia and Thailand (Fig. 1.5). It is reported that 90% of mortality cases in African children result from malaria, which is more than 2 million deaths every year [19][20]. A strong factor behind the high mortality rate due to CM is the high percentage of its misdiagnosis with other concurrent diseases. The malarial cases occur in regions where other concurrent diseases have equivalent spread. Thus, even if the clinical definitions of malaria and malarial coma are satisfied, the other causes of coma cannot easily be excluded. World health organization (WHO) criteria for the diagnosis of malaria require the detection of parasitemia, severe anemia, respiratory distress, unconsciousness and exclusion of other causes, which often becomes difficult due to the following reasons. A commonly used diagnostic sign of severe malaria, i.e., presence of plasmodium falciparum parasitemia is insufficient by itself to confirm the presence of CM, since parasitemia is diagnosed as a sign in other concurrent diseases, (prevalence of parasitemia is around 70%) and parasitemia may not always be the reason behind malaria [21][22][23][24]. Other clinical signs of severe malaria are non-specific (respiratory distress, anemia, jaundice) and may overlap with signs for other diseases such as pneumonia and non-malarial coma [6][24].

In order to increase the sensitivity of the diagnostic test for cerebral malaria


Figure 1.5: Regions affected with cerebral malaria, Travel Medicine Alliance eUpdate - health news and information for international travellers, August 2008

the, detection of malarial retinopathy (MR) is proposed in which its presence and severity are associated with the death risk and the length of malarial coma due to cerebral malaria. MR distinguishes cerebral malaria from other diseases as well as the non-malarial comas with the set of unique diagnostic features not observed in other diseases [6][20][23]. Patients with parasitemia but no MR were reported to have causes of death other than malaria such as pneumonia, Reye's syndrome, CNS injuries and head trauma [21][22][23]. For parasitemic patients, MR increases the specificity of diagnosis from 60% to 100%, the positive predictive value (PPV) and negative predictive value (NPV) above 90% [5]. The studies have reported 100% specificity and 95% sensitivity of MR detection for the diagnosis of cerebral malaria [21].

The correlation of cerebral pathologies with those occurring on a retina is an important factor. Retina is a part of a central nervous system in the embryonic aspects and hence it shares the similar architecture and microcirculation activities as that in

the cerebral system which is the embryonic extension of a cerebral cortex. Hence the histological features observed on retina such as sequestration of red blood cells (RBC) due to mature CM parasites (detected as retinal whitening) may suggest the similar activities in the brain [5]. The retinal whitening as a result of ischemia, filling defects, impaired blood retina barrier, capillary non-perfusion, and number and size of retinal hemorrhages in MR correlate with the cerebral non perfusion and number of hemorrhages in cerebral circulation (Spearman's correlation=0.8) [25]. Thus, the diagnosis based on retinal signs of MR may suggest the parallel activities taking place in cerebral vessels and hence may confirm the presence or severity of cerebral malaria.

Severe malaria may result into a neurological disability in children, coma and even death if the timely treatment is not available [19][20]. The secondary reason behind the high mortality rate due to CM is the dearth of available neurodiagnostics, ophthalmologists, limited laboratory support, and less electroencephalography use in the affected regions [21], which results into an inadequate and non-specific treatment of cerebral malaria. In order to decrease the death risk, the diagnosis and the associated treatment must be applied immediately within few hours of indication, when most of the deaths take place. Therefore a quick and an automated method may help providing the diagnosis results immediately irrespective of the presence of a specialist physician or the required laboratory support [19][23]. The automated evaluation of retinal fundus images may quickly diagnose the cause of the illness and the intensive supportive interventions such as anti-malarial drugs may be applied immediately to prevent the death of a patient [23].

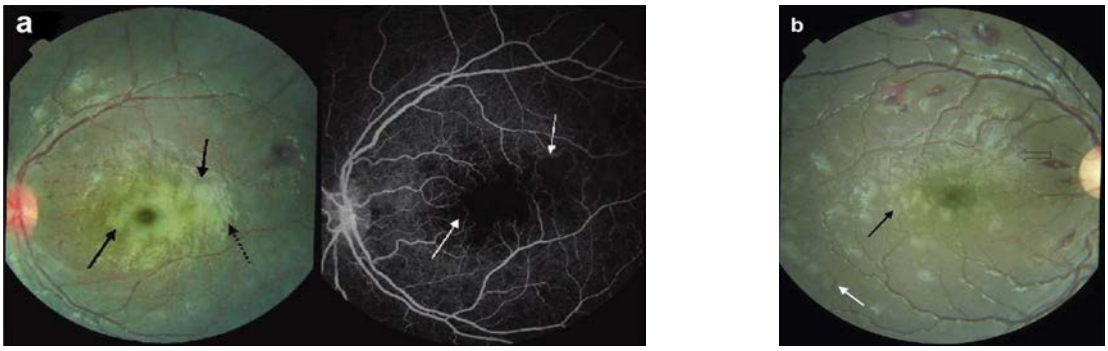


Figure 1.6: Retinal whitening: a: Paired retinal fundus image and FA image [5], b: retinal fundus image [6]; Retinal whitening (solid black arrows: fig.a), capillary non-perfusion (white arrows: fig.a) with unaffected foveola, peripheral whitening (white arrow: fig.b), glare artifact (dashed black arrow: fig.a)

#### 1.2.3.2 Pathologic signs of malarial retinopathy

The retinal whitening may be observed as a patchy opacification of retina near to macula but sparing the central fovea, called macular whitening, or at the peripheral retina outside the temporal arcades known as the peripheral whitening (Fig. 1.6) [19][20][21][23][24][26]. The reason behind its occurrence is mostly due to the metabolic or hypoxic stress on retina suggesting abnormal tissue perfusion such as capillary non-perfusion, filling defect and impaired integrity of blood retina barrier [5][21][22]. The whitening is less brightly white, with no demarcated edges and more widely distributed as compared to the cotton wool spots. It is similar in appearance with the ischemic whitening such as that occurring due to the vessel occlusion, with the sequestration of infected erythrocytes [6][19][27][21][22]. The detection of retinal whitening resulting from the retinal hypoxia and ischemia suggests the occurrence of similar activities in the brain, in cerebral malaria [22][23][24]. Therefore, the treat-

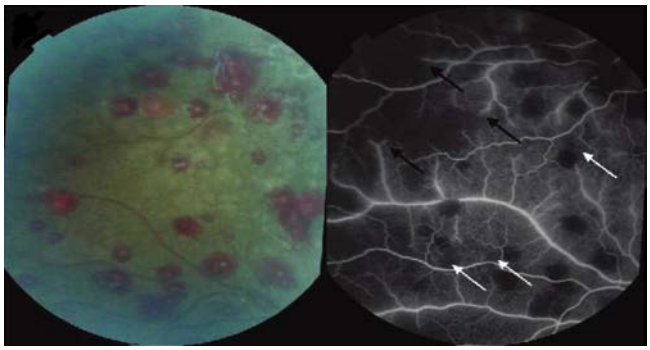

Figure 1.7: Paired retinal fundus image and FA image [5]; White centered hemorrhages show the blocked fluorescence and the black and white arrows show the areas of non-perfusion

ment suggesting a cure to a hypoxia and to improve the tissue perfusion may be beneficial [5].

The hemorrhages are white centered, intra-retinal blot hemorrhages or flame and large hemorrhages (Fig. 1.7), which may number more than 120 in severe CM compared to the number of hemorrhages in non-CM cases [6][22][24][25]. Their number suggests the fatality and length of coma in malaria, as they correlate with the number of hemorrhages occurring in cerebral vessels (Spearman's correlation = 0.8 as reported in [25]). The retinal hemorrhages are histopathologically similar to the ring hemorrhages in brain [6][19][22][23][25][27]. Absence of retinal hemorrhages correlates for 100% of cases with the absence of cerebral hemorrhages [25]. As a result, the absence of retinal hemorrhages precludes the possibility of MR or cerebral malaria as reported in [20][25][26][27][28]. MR hemorrhages are often associated with the presence of a thrombus in a small vessel at the center of a hemorrhage which creates a white spot (Roth spot) in the middle and these hemorrhages are rarely seen in


Figure 1.8: Vessel abnormalities: a: Paired retinal fundus image and FA image [5]; b: retinal fundus image [5]; a) Whitened retinal vessels in the area of retinal whitening suggest the occlusion of vessels resulting into a non-perfusion. The vessels are red in color till the point of occlusion, b) Discoloration of vessels with resulting orange/white color and tramlining on large vessels.

diseases other than CM [22][23]. The plasmodium falciparum parasites become mature to cause the sequestration of RBCs in endothelial linings of deep capillaries and venules in organ systems such as cerebral and retinal vascular networks which gives rise to a thrombus resulting into a blood hemorrhage [22][27].

Vessel abnormalities are observed as the discoloration of peripheral retinal vessels to orange and white appearance, orange and white tramlining within larger vessels, corresponding to a narrow blood column in fundus images [21][24][27] or as a dense mottling in fluorescence angiography images [5], (Fig. 1.8). The segmental change in color from red to orange/white suggests the presence of dehemoglobinized RBCs containing mature, pigmented, plasmodium falciparum parasite and the color pigment represents the by-product of hemoglobin degradation, also called the malaria pigment [21][22][23][27]. The sequestration may transform into a vessel occlusion and the resultant non-perfusion or ischemia [29]. The vessel abnormalities are more

common to veins rather than arteries [5][23]. A statistically significant correlation exists between the stage of parasitic maturation in fundus and that in the brain [27][29]. Hence the retinal vessel abnormalities in MR suggest the sequestration of parasitized RBCs on retina as well as in the brain, in cerebral malaria [27]. The retinal whitening, roth spot hemorrhages and vessel abnormalities are the pathological signs unique to MR and CM suggesting a strong correlation between MR and severe cerebral malaria [6][5][19][24][27][28].

## 1.3 Retinal imaging

### 1.3.1 Retinal color fundus imaging

Several imaging techniques are available for imaging the fundus of a patient to be screened. The choice of an imaging method depends upon the type of pathology under study. Digital color fundus photography and fluorescence angiography are the commonly used methods for imaging retinal blood vessels. Fluorescence angiography is used depending upon the patient's age and its physical response to it. As there is a possibility of allergic reactions to the patients, and the reports of mortality rates of 1:222000 with the use of FA [30], color fundus imaging is most commonly used for the large population studies.

In color fundus imaging, the images can be obtained with natural dilation of pupil (non-mydriatic) or the artificial dilation (mydriatic) with a drug called tropicamide. Mydriatic images provide better contrast and image quality since sufficient light is allowed to pass through the pupil, but may be associated with patient discomfort. The camera specifications in terms of resolution and field of view (FOV) are

used depending upon the requirement of the pathology to be detected, part of the retina to be imaged and the measurement accuracy required. The FOVs with angular measurements of 35, 40 or 60 degrees have been reported. Smaller FOV covers relatively less retinal area therefore one may have to image the different parts of retina from different viewing angles and register them. As the FOV increases, the part of retina imaged by the camera appears distorted in the image, due to the hemispherical shape of retina, i.e., conversion from three-dimensional hemispherical retina to two-dimensional image surface.

The images obtained from different sites, captured with different FOVs, can be resized to the standard FOV by a method such as cubic spline interpolation [31][32][33]. Resolution of a camera can vary from, e.g. low-768x576 to high-2948x1536 values for different cameras. High resolution camera images are recommended for detecting pathologies with increase in specificity [34]. They are important especially for an application of size measurements such as vessel width measurement [35]. The high resolution images require significantly large storage space which may limit the data transmission capabilities. Therefore a data compression technique such as a JPEG compression is applied to the image. JPEG compression causes the loss of data and may produce significant errors in the parameter measurements such as vessel width or in vessel segmentation by producing the jagged/distorted appearance of vessels [33][35]. Therefore, the JPEG compression parameters should be adjusted so as to compromise between storage/transmission requirements and the image quality.

The color fundus images are obtained using a predefined protocol. Commonly,

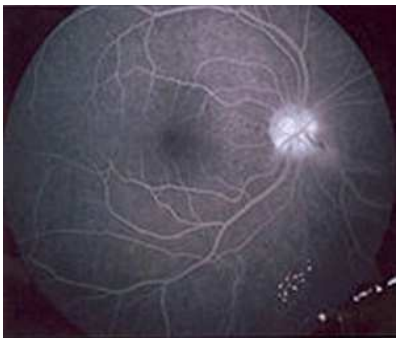

Figure 1.9: Fluorescence (through vessels) captured during FA [1]

for the retinopathy screening, four images are obtained for each patient, two images each eye, one with optic disc (OD) at center and the other with fovea at center. The clinically accepted standard for retinal imaging is known as seven standard-field fundus photographs obtained by certified photographers. The photographs are captured with seven fields on the fundus marked according to their clinical significance. This method is highly accurate, however it may not always be used for large screening population.

### 1.3.2 Fluorescein angiography

Fluorescein angiography (FA) is a standard imaging technique used on a large scale for retinal imaging (Fig. 1.9). FA is a valuable imaging modality due to its property to detect even a minute leakage in the retinal blood vessel wall. Unbound fluorescein cannot permeate the blood retinal barrier due to the impermeability property of the barrier. Whenever the unbound fluorescein content is imaged outside the blood vessel barrier, the leakage in the barrier can be detected. This is how the FA stands important in diagnosing the neovascularization in choroidal layer and ischemic

regions on the retina, e.g., at macula [7].

FA is used for a diagnostic purpose in which the conclusions are based on the presence of hypofluorescence or hyperfluorescence [1][16]. Hypofluorescence is observed in case of vessel occlusion, hemorrhage, vessel blocking such as capillary blockage, whereas the hyperfluorescence occurs due to the leakage, abnormal blood vessel growth (neovascularization), aneurysm formation, staining, and transmission problems.

FA may be used for functional imaging as the fluorescein dye is in motion with the blood flow. It may show the blood movement, blood perfusion and leakage, if any. Hence it can be used to determine the dynamic changes such as defects in the blood flow or circulation. It can determine the blood accumulation at the occlusion site and if synchronized with time, it can detect approximately the blood flow per unit time at the same site. FA can also be utilized to determine the fluid balance in circulation, which may not be obtained with other techniques.

FA may not provide accurate results in detecting retinal swelling/thickening which is prominently observed on the damaged retina than in the area of fluid accumulation. As the FA results get affected with the interference from fluid accumulation, it may not be a good choice for detecting the retinal thickening.

### 1.3.3 Optical Coherence tomography

Optical coherence tomography (OCT) is based on optical imaging, used specifically for optically scattering media. It is mostly used for three dimensional imaging giving quality images with high resolution up to micrometers (axial resolution: 1 to

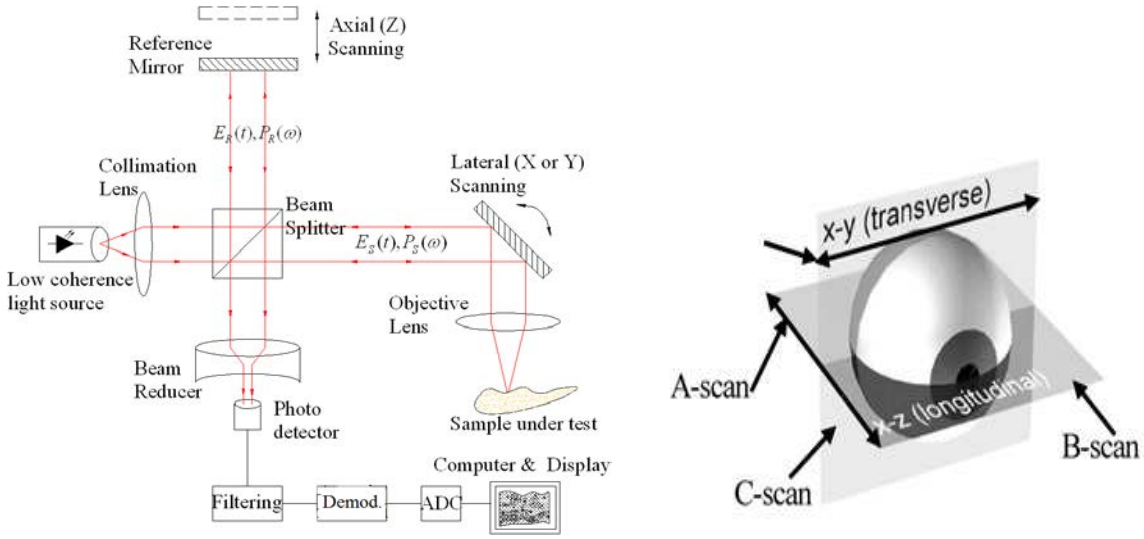


Figure 1.10: OCT: a) Setup [1] b) Imaging protocols

15 micrometer) and relatively high penetration depth (millimeter). As the retinal structures are of minuscule sizes, they require a high resolution imaging system to acquire desired quality images. OCT is a commonly used, highly reliable diagnostic imaging method used for geometrical measurements of retinal structures such as retinal thickness in diabetic edema and retinal swelling [7].

The principle of OCT is based on optical reflecting properties of the specimen to be imaged (ocular structure). The light is projected on the specimen and the time of flight of the reflected light is measured to determine the location of various structures in the specimen. Since the time of flight cannot be measured directly due to the minuscule specimen dimensions and high velocity of light, OCT employs a low coherence interferometry technique (Fig. 1.10(a)). The beam of light to be projected on the specimen is split into two parts with the help of a beam-splitter. Part of

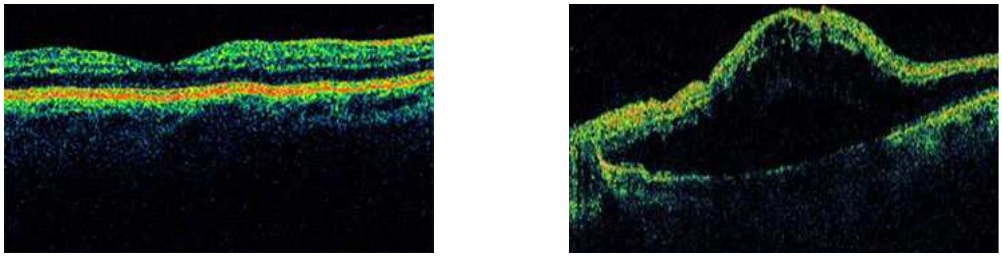

Figure 1.11: OCT images: a) OCT of a normal retina [7], b) OCT for detecting the retinal swelling [7]

the light is projected on the true specimen and the other part is projected on the reference mirror, also known as reference arm. The light rays get reflected back from the specimen of interest (at different optical interfaces), and also from the reference arm. Both the light rays combine to form an interference pattern only when the light rays travelling on both the paths are coherent, i.e. optical path difference between two light rays is very small or close to zero. This gives the modulated interference pattern for which the amplitude is dependent upon the optical path difference between the two light rays. OCT setup uses the low coherence interferometer such as Michaelson's interferometer [1].

OCT measures the time of flight of a light ray reflected from different optical interfaces in the specimen. Measuring this time interval gives the spatial dimension such as location or depth of the interface (structures) in the specimen, called the A-scan. Position of the A-scan gives the location and its strength gives the reflecting properties of the interface. A lateral combination of consecutive, axial A-scans gives the two-dimensional (cross-section) image called the B-scan. Next step is to register

number of B-scans to construct a three-dimensional structure of the specimen. C-scan is the cross sectional image of the specimen at the desired depth (Fig. 1.10(b)). OCT measurements are carried out either in time domain or frequency domain [1][16][7]. Fig. 1.11(a) shows the B-scan for a normal retina and Fig. 1.11(b) shows the B-scan for abnormal retinal swelling [7].

## 1.4 Organization of the Thesis

This thesis is divided into 4 chapters. The rest of the thesis is organized as follows:

Chapter 2 presents the background on the retinal image analysis using variety of automated and semi-automatic techniques. It includes the description of crucial steps in retinal image analysis, such as image preprocessing, image quality analysis, vessel segmentation, detection of retinal anatomic features, retinal lesion detection, and vessel morphology analysis. It also discusses pros and cons of variety of methods proposed in the literature. This chapter also describes the significance of thesis work through the development of new methods in order to advance the field of retinal image analysis.

Chapter 3 presents the automated methods developed for the research thesis for retinal vessel structure analysis and morphology measurement. For each method, the section describes algorithm development, validation dataset, results, its contribution over previous methods and its limitations. It also presents the results of the longitudinal study dataset analysis. Chapter 3 presents the methods published or in the process of publication as follows:

1. Joshi, V., Garvin, M.K., Reinhardt, J.M., Abramoff, M.D.: Identification and reconnection of interrupted vessels in retinal vessel segmentation. In IEEE, ISBI, Image Segmentation Methods, FR-PS3a.7, Chicago (2011) 1416-1420

1. Joshi, V., Garvin, M.K., Reinhardt, J.M., Abramoff, M.D.: Automated method for identification and artery-venous classification of vessel trees in retinal vessel networks. Submitted to IEEE Transactions on Medical Imaging (2012)

1. Joshi, V., Reinhardt, J.M., Abramoff, M.D.: Automated measurement of retinal blood vessel tortuosity. In Proc. SPIE Medical Imaging, Computer-Aided Diagnosis, 7624, 76243A, San Diego (2010)

1. Joshi, V., Tang, L., Garvin, M.K., Reinhardt, J.M., Maude, R.J., Abramoff, M.D.: Automated detection of malarial retinopathy associated retinal hemorrhages. Submitted to Investigative ophthalmology and Visual science (2012)

Chapter 4 concludes the thesis and proposes some interesting aspects of the future research.

# CHAPTER 2
# BACKGROUND

## 2.1 Automated retinal image analysis

The retinal abnormalities are the precursors of various retinopathies as well as cardiovascular diseases. With routine eye-checkup, early diagnosis of the retinopathy, and the on-schedule treatment may prevent its development. Very first stages of the disease may be clinically asymptomatic and hence the early diagnosis is required to refer the patients with the high probability of retinopathy for the further diagnosis, and screen out the patients with no pathologies detected. The retinopathies such as diabetic retinopathy (DR) are identified based on the measurement of morphologic changes in retinal vessels or by the presence of retinal lesions. In the routine checkup, it is done manually by an ophthalmologist. But considering the large population of patients to be screened and non-uniform availability of eye specialists in the country (remote areas), an alternative to this problem is required. With the use of various image processing algorithms, I make an effort to find an automated, optimal, highly accurate, and relatively less time consuming solution to this problem. An image processing method for the assessment of retinopathies consists of a step by step procedure described as follows considering diabetic retinopathy as an illustration (Fig. 2.1).

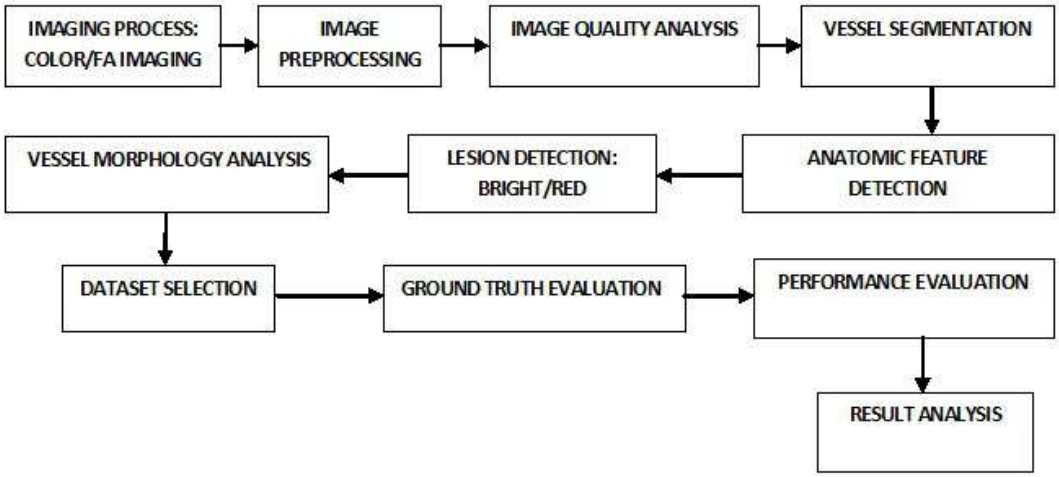


Figure 2.1: A flow-chart explaining a stepwise procedure for an automated retinal image analysis

### 2.1.1 Image preprocessing

Image preprocessing includes the image enhancement procedures such as contrast enhancement, image sharpness enhancement, correction of non-uniform illumination, standardization of the images obtained from different sources (FOV standardization), FOV/background matching, and resizing of the image to a standard size. The contrast enhancement technique using adaptive histogram equalization is suggested in [36][37]. For low quality/degraded images due to non-uniform illumination, shade correction using average/median filter or the image restoration techniques have been proposed in [38][39][40][41]. Different noise removal techniques have been reported such as morphological opening or filtering [42].

### 2.1.2 Image quality analysis

The image datasets for DR screening are obtained from different locations, image capturing sites, with different cameras and photographers with varied levels of skills, and it produces a large variation in the images obtained in terms of illumination scheme, sharpness, contrast, focus and FOV. For an automated analysis of such images, one needs to determine the quality of each image in order to obtain reliable and robust estimates of pathological signs. The method reported in [43] determines the image quality based on the detection of relatively darker structures such as blood vessels by matched filtering and by K-means clustering, which is claimed be related to the image focus and image sharpness. The image quality also depends upon the contrast and the color saturation which is not considered in this work. Another method presented in [44] uses global edge and intensity information forming a mean template histogram from a small set of good quality images, and the histogram of each image under analysis is compared with the template to determine its quality, however it fails to account for large variation in images. A method [45] represents segmentation of vessels to quantify the detection of small vessels around macula and to detect other retinal sub-structures to estimate the image quality. It is based on the assumption that the small vessels near to the macula become hardly visible even with little degradation of image quality. A technique proposed in [31] named as image structure clustering, determines the image quality based on the presence of significant sub-structures and their respective positions on the retina, using a set of Gaussian filters. The filter responses are taken into account to classify the image as low quality

or a good quality image. This method is limited in identifying the image as a low quality image if any of the retinal structures is not detected, such as undetected fovea due to low contrast or its occlusion by pathologic lesions, and the non-standard photography. The method [45] sounds reasonable as it detects the image quality based on smaller vessels near to the macula irrespective of the contrast level at the macula and in addition it implements the notion described in [31] to determine the relative ratios and distance constraints of the retinal sub-structures which cannot completely be occluded by pathologies or photographic defects.

### 2.1.3 Vessel segmentation

Segmentation of a vascular structure is the heart of retinal image analysis system and important for many purposes such as sub-structure detection (optic disc and fovea), lesion detection (especially for red lesions as they are often confused with the vessels), and morphology measurements. Choosing the best segmentation algorithm is a critical task and it is application dependent. The accuracy of morphologic measurements is highly dependent upon the accuracy of the vessel segmentation method and is often affected by vessel segmentation noise and vessel interruptions, especially for width and tortuosity measurements. The choice of vessel segmentation method is based on the diagnostic application, morphologic parameters to be evaluated, accuracy requirement, and tolerance to imaging defects.

Several methods were reported for vessel segmentation based on the property of a vessel cross section that approximates the Gaussian profile [35][46]. The method [35] utilizes the maximum likelihood model fitting approach using the Gaus-

sian model, but may need manual editing and the technique may fail for the vessels with higher or lower width for which the constant Gaussian standard deviation is approximated. A method proposed by [46] uses matched filtering with the convolution kernel at each point on the vessel at different orientations, but happens to be highly sensitive to standard deviation and kernel parameters. The method is slow as it includes the convolution for 12 different orientations. It also suffers from interrupted vessel segmentation and false detection of vessels with varying widths and orientation. A method proposed in [47] uses scale space analysis based features such as first and second derivative of the intensity image, and segments with the region growing approach. The topological information deals well with the low contrast and non-uniform intensity images ensuring the vessel connectivity and the scale space representation handles the varying widths of vessels. A supervised method such as [48] and the one using pixel classification with Gaussian filter set and kNN classifier [33] have been proposed which show promising segmentation results. They need a large training dataset and work with statistical probabilities rather than the objective reasoning base. The other supervised method based on ridge detection is proposed, which extracts the ridges in the image approximating the vessel centerlines [49]. This method is based on identification of a ridge based line elements and their classification as vessel or non-vessel. Due to the probabilistic nature of classifying elements based on a feature vector, this method does not ensure the connectivity of vessels.

The methods based on mathematical morphology (MM) work out to be faster and noise resistant compared to the supervised methods, as the vascular shape is

known a priori, which is piecewise linear [42][50]. The method [50] based on MM and cross-curvature evaluation gives encouraging results, but the results are based on the fluorescence angiograms rather than the color images. A method [51] uses vessel centerline extraction based on differential directional operators and the region growing scheme. This method suffers from vessel interruptions and undersegmentation of vessels due to low contrast and non-uniform illumination. A method reported in [30] uses MM techniques to extract the linear shapes of vessel along with the derivative operators to utilize the Gaussian profile information. The disadvantage of MM methods is its dependency upon the choice of structuring elements, neighborhoods and window sizes which are constrained by the vessel features such as tortuosity and noise [30][50].

Several vessel tracking methods were reported. The article [52] proposes the intensity based Gaussian model fitting approach for vessel tracking. A method [53] uses a vessel tracking based on Canny edge detection, whereas Cree et al. [54] estimate the two-dimensional non-linear least squares fit model to track the vessels. Kochner et al. [55] propose a use of steerable filters to develop the tracking algorithm. These methods may suffer from low contrast, vessel interruption, model break-down at the junction of vessels, and may produce erroneous results for small vessels or tortuous vessels. The article [56] detects the branching and crossing points and corrects the false vessel detections. Many of the vessel tracking methods may not be able to deal with vessel interruptions properly and they either result into false detections or discontinuous vessel segments, though method [56] solves this problem up to some

extent. The vessel interruption problem may be solved with the ridge detection based graph search approach described in the thesis [57], as explained in chapter 3. Tracking methods cannot differentiate between an artery and a vein and hence may not help determining the vessel type specific properties such as arterial tortuosity or venous width [58]. These methods may not be able to identify vessel generations, i.e., the parent vessel for every bifurcation and vice versa, hence cannot map a vessel tree in which all the branches correspond to a single parent vessel. The vessel analysis may be improved by a method proposed in the thesis [59] known as structural mapping, as explained in chapter 3. Using the vessel structural mapping method, the parent vessel and its branches could be identified separately and labeled. The artery-vein separation may thus be obtained by analyzing the vessel trees separately, as proposed in the thesis [59], explained in chapter 3. The color features extracted from each vessel tree and the fuzzy C-means clustering algorithm used for classification, provide two separate classes describing the vessels as arteries or veins, as will be explained later.

### 2.1.4 Detection of retinal anatomic features

The detection of anatomic features in the eye, i.e., optic disk (OD), fovea, and retinal vasculature, is an important step due to various reasons:

1) To analyze the clinical significance of the lesion location with respect to the retinal sub-structure, e.g., the distance of a lesion from fovea may indicate the severity or threat to the vision [60][61].

2) To assess the image quality by detecting the anatomic structures and confirming

the field definition [45].

3) To assess the image clarity, contrast and intensity variations [45].

4) To prevent the false vessel detection during the vessel segmentation, the sub-structures should be detected and masked.

5) The OD, fovea and vasculature detection may possibly be used for registration of images at coarser levels, for the same patient over successive visits [62]. The OD can also be used as a calibrator for determining the image dimensions.

In summary, this step is an automated image grading algorithm to decide whether or not the image can be used for further analysis [63].

Several methods were proposed for sub-structure detection based on the intensity information, such as contrast or brightness of the optic disk, and the low intensities at fovea. Few methods propose the detection of sub-structures based exclusively on their geometry such as shape, e.g., using the Hough transform [55][64]. A method for OD detection at the highest concentration of endpoints of blood vessels has been proposed, but the highest concentration can occasionally be found somewhere else than at the OD [41]. A recently proposed method detects the elliptical vascular arch and identifies the OD near to one of the vertices of the major axis of ellipse and the fovea at the approximate location between the OD center and the ellipse center [63][65]. It is insensitive to the local feature changes and invariant to the image rotation. A method presented in [32] uses a set of points which are fit to the retinal image and their distribution model is analyzed to locate the anatomical structures. To position the points correctly, the model estimates the global properties

based on vascular arch and local properties based on the neighborhood structure at that point. The other method presented by the same group [66] has described the detection of optic disc location by k-nearest neighbor regression method based on vasculature detection which defines the local feature measurements. The performance of the methods [32][63][66] is encouraging and the choice of a method depends upon the application at hand.

### 2.1.5 Retinal lesion detection

The retinal lesions in case of DR can be classified into two types depending upon their appearance, viz., bright lesions and red lesions. Bright lesions are further classified into three types, viz., hard exudates, cotton wool spots, whereas the red lesions are classified into microaneurysms, hemorrhages and microvascular abnormalities. For the literature evaluation, I focus on the methods for the detection of retinal hemorrhages as a background on new hemorrhage detection algorithm I propose.

#### 2.1.5.1 Red lesion detection

The lesions are red in color appearance. They are classified into three types, viz., microaneurysms, hemorrhages and microvascular abnormalities. Microaneurysms are known to be the explicit signs of DR and their presence directly confirms the occurrence of DR without the identification of any other lesions [67]. Microaneurysms are formed due to the dilatations of the blood vessel capillaries, which appear as small and round red dots.

Hemorrhages are formed due to the blood leakage in vessels and could be

classified into dot, blot, and flame hemorrhages. A technique based on RRGS and binary thresholding detects the microaneurysms, hemorrhages and vasculature from the green color channel and removes the vasculature afterwards. Remaining structures in the image are considered to be the red lesions [68]. These methods work solely with the intensity based approach [67] and may lack in differentiating between the red lesions and nearby nerve fibers, interrupted blood vessels, especially the smaller blood vessels [69]. Few supervised algorithms were reported for red lesion detection, based on a neural network approach [48] or based on pixel classification with selected features [38]. The feature set includes intensity, shape, and size based features for vasculature and lesions. The vasculature detection is of foremost importance and it should be accurately identified so as not to miss any red lesions when the vasculature is removed. The unique technique [38] utilizes is the hybrid approach for red lesion detection which compares and combines the results from mathematical morphology based methods [39][68][70][71] and a supervised learning method.

### 2.1.6 Vessel morphology analysis

For the retinal vessel analysis, I select five morphologic properties which may undergo modification in the presence of a retinopathy or a systemic disease. In order to describe its significance, we proceed with the example of diabetic retinopathy (DR) and the morphologic changes it may bring to the retinal vessel structure.

DR may be identified by the presence of retinal lesions or the morphologic modifications in retinal vessels. The features utilized for differentiation and detection of retinal lesions are often based on their luminance, local contrast and intensity

properties [62]. These features may be affected by the imaging defects such as noise, low contrast, non-uniform illumination and low intensity. Furthermore, the lesions may be confused with other retinal structures by image processing algorithms. The nerve fibers, interrupted blood vessels, laser treatment scars, optic disc dots can be falsely detected as red lesions or exudates and result into false positives [69][67]. Similarly, the red lesions connected or near to the vasculature represent the false negatives. Since the fundus photography only samples a small part of retina (One-field and two-field photography) it may miss the localized presence of lesions [45].

The pathological factors associated with diabetes such as diabetes duration, high A1C levels, high blood pressure affect the microvascular structure irrespective of occurrence of DR which suggests the presence of microvascular abnormalities even before the occurrence of clinical pathologies such as lesions [10]. Potentially, the vessel abnormalities may be the precursors of diabetic retinopathy lesions that are commonly detected.

Therefore, we focus on the following properties of retinal vessels which describe the morphology of individual vessel as well as that of a vessel network.

1) Vessel tortuosity

2) Vessel width

3) Branching angle

4) Branching coefficient

5) Fractal dimension

Figure 2.2: Increased vessel tortuosity and vessel dilatation in a patient with severe NPDR [8]

#### 2.1.6.1 Vessel tortuosity

The physiological relationship between diabetic retinopathy and vessel tortuosity may be described as follows. The retinal vessel tortuosity may be defined as a measure of curvature and twists or kinks produced in the vessel course (Fig. 2.2). It may be associated with the average internal transmural blood pressure (BP) [72], but it does not show significant increase till the critical pressure is reached, and shows highly proportional increase after the critical point [72]. Therefore at higher transmural pressures, vessel tortuosity is a more sensitive indicator of the increased BP and related hemodynamic changes in retinal vessels. These pressure ranges are often obtained in diabetes due to its relation with hypertension [72][73][74], with systolic BP above 140 mm Hg. and dystolic BP above 90 mm Hg.

The tissue perfusion and the peripheral resistance are the two major factors responsible for structural changes in vasculature leading to a vessel tortuosity [75]. It responds to the adaptive changes due to the hemodynamic and metabolic stimuli. The

formation of artery-venous collaterals, anastomosis and angiogenesis as a response to ischemia may result into a tortuous course opted by vessels. Vessel occlusion and inflammation may affect the retinal blood circulation and produce tortuosity. The DR is associated with the degeneration of retinal vessel walls and changes in their elastic properties, which can lead to a vessel tortuosity [76]. The study [73] reports that even a single inhomogeneity occurring at the blood vessel wall triggers the tortuosity which increases with the inner pressure. Thus the presence of hypertension [74], and vessel wall inhomogeneity resulting from microvascular degeneration and atherosclerosis, may suggest the estimation of the retinal vessel tortuosity for DR diagnosis (Fig. 2.2) [73].

The clinical studies describing the relation between diabetic retinopathy and vessel tortuosity are as follows. The vessel tortuosity, specifically the arteriolar (small vessels) tortuosity increases with the high blood flow, angiogenesis, vessel occlusion and hypertension which accompany DR [77][78][79]. The studies also report the changes in vessel tortuosity due to the presence of diabetes related factors like HbA1c levels (disturbed endothelium) and disease duration [10][80]. Article [81] focuses on the effects of oxygen tension on the venous tortuosity, and concludes that the diabetic veins adapt more easily and frequently to the oxygen tension and blood flow changes, compared to the normal veins. The smaller vessels often get affected by blood flow, blood pressure and toruosity for which I propose to include the entire vessel network into analysis with no bias for larger vessels or the bias for region of interest.

The previous approaches explored for the quantification of retinal vessel tortu-

osity may be described as follows. The quantitative analysis of changes in geometric or morphologic pattern followed by the vessel course, determines the numerical measure of tortuosity of a vessel, called the tortuosity index (TI). Few of the methods proposed for the tortuosity estimation may be limited in considering the important parameters involved in tortuosity measurement, i.e., curvature sign change and the magnitude of curvature of the vessel. These methods are based solely on the conventional arc to chord ratio technique [30][82], solely on the number of direction changes in vessel course [83], or solely on the integral curvature estimation [84] to measure the tortuosity. They may not be able to imitate the clinical perception of tortuosity. Therefore, a metric formulating these individual parameters together may improve the measurement performance [85]. A method proposed in literature estimates the vessel tortuosity according to the Fourier analysis of segments perpendicular to the vessel centerline [86], or the other one which uses the polynomial spline fitting [79]. However, the techniques based on global tortuosity measurement do not correlate well with the human perception, as compared to the techniques considering contributions of the local tortuosities [82]. A method presented in [87] considers the arc to chord ratio and the curvature sign change based on the local tortuosity contributions but does not take into account the magnitude of curvature of the vessel. This method correlates well with the human perception of tortuosity, but falls short in determining the appropriate tortuosity for constant curvature vessels and vessels with equal arc to chord ratios. A method proposed in [76] is based on estimating the tortuosity of vessels in proportion with the local thickness of the vessel. This method estimates

the average of the two curvature values obtained at two boundary points at the cross section of the vessel.

#### 2.1.6.2 Vessel width

The physiological relationship between diabetic retinopathy and vessel width may be described as follows. The structural modification in retinal vessels occurs due to the hemodynamic and metabolic stimuli which change the blood flow dynamics producing number of stresses on vessel walls and may destroy the auto-regulatory mechanisms [77]. The vessel width increases with wall shear stress (blood flow) and the vessel wall thickness increases with the circumferential wall stress (intravascular pressure). The blood flow and pressure ranges related to the vascular width increase are often obtained in DR due to its relation with the hypertension [72][73][74]. The smaller vessel (venules) dilatation and elongation in DR resulting into an increase in hydrostatic pressure (Starling's law) has been reported causing the diabetic edema [81]. The width increase has also been reported in diabetes for carotid artery [77] and the vessels of conjunctiva [78] as the effect of increased transmural pressure. The dilatation of blood vessels in these ocular structures suggests the need of investigation of changes in width of retinal vessels in presence of diabetes and DR.

The clinical studies describing the relation between diabetic retinopathy and vessel width are as follows. The studies reported in [10][80][88][89] analyze the geometric changes in retinal microvasculature in type 1 diabetes. They report the smaller venous length to width ratio (LDR) or increased venous width with increased systolic BP, and higher arteriolar LDR or decreased arteriolar width with increased choles-

terol level. Both the factors are related to the disturbed auto-regulation function of arterioles due to diabetes and higher blood pressure observed in hyper-perfusion and hypertension. The tissue hypoxia and ischemia increase the venular width and decrease the arteriolar width [90]. The hypertensive vascular changes and atherosclerotic changes are related to narrower arteries, endothelial dysfunctions and inflammation changes with wider veins, all of which are indicators of incident DR [91]. The studies in [91][92][93] report the increase in the venular width and decrease in mean arterial width with the duration and severity of diabetes. The study in [90] with 3368 participants reports the association of severe non-proliferative DR (NPDR) with wider venular widths and incident/mild NPDR with wider arterial widths as compared to non-diabetics or diabetics without DR. The dilatation and elongation of smaller vessels at the onset of diabetic macular edema has also been reported in [81]. This study also reports the constriction of arterioles and venules on the photocoagulation treatment of edema, i.e., the reverse effect which may be of a prognostic significance.

The previous approaches explored for the determination of retinal vessel width may be described as follows. A width measurement can be obtained by measuring the standard deviation of Gaussian model fit at the vessel cross section or by using the measure of isotropic contrast at the vessel centerline and at the edges [82]. These methods require adequate contrast between the vessel and the background and may suffer from non-uniform illumination. A method proposed in [30] measures the minimum of the widths computed at different orientations at a point on a vessel centerline, between the vessel edges. An algorithm proposed in [94] determines the

vessel width as the distance between points at which the one dimensional intensity profile marks half of the maximum intensity value to both sides of the center point. Lowell et al. proposed a method based on two-dimensional difference of Gaussian model optimized to obtain a fit to the two-dimensional intensity profile of a vessel segment [95]. A method [96] reports the vessel width as the width of the rectangle fit to the one-dimensional vessel profile so that the rectangle area becomes equal to the profile area. The method reported by Al-Diri et al. uses a growing ribbon of twins active contour model with two pairs of contours for estimating the vessel edges [97]. A recently proposed method by our group estimates the vessel width by means of a two-slice three-dimension surface segmentation problem and determines an optimal surface by a graph search [98].

#### 2.1.6.3 Branching angle

The physiological relationship between diabetic retinopathy and branching angle may be described as follows. Retinal branching/ bifurcation angle is defined as ($\Theta 1 + \Theta 2$), as an angle between two daughter vessels at the bifurcation (Fig. 2.3(a)) [80][88][99]. The optimum bifurcation angle between the vessel branches is formed so as to achieve the fastest transport of blood for the least amount of work. Branching angles are related to energy spent in blood transport, the diffusion distance and the efficiency of flow, for which the optimum value of angle is $72^\circ$ [10][88]. This efficiency reduces if the bifurcation angles become too large. The vessel bifurcation occurs mostly as a result of retinal ischemia and the requirement of a tissue perfusion [88]. The deviation of branching angle measurement from the optimum may suggest

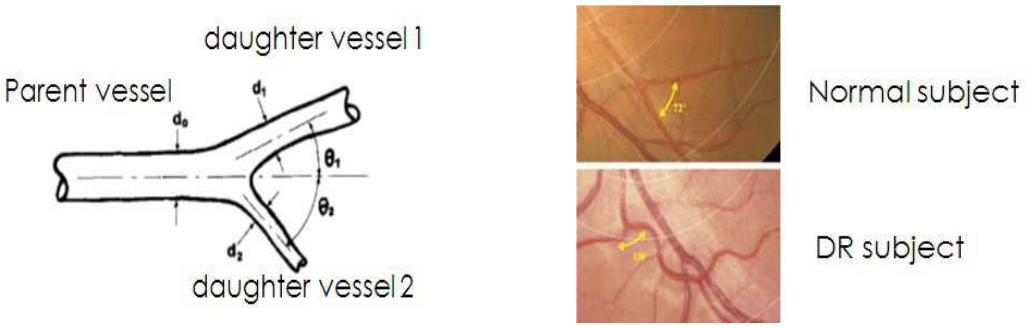


Figure 2.3: Branching angle and branching coefficient: a) Measurements [9] , b) deviation from optimal branching angle measurement in normal (72°), to higher branching angle measurement (130°) in DR [10]

the abnormalities in the branching architecture caused by a disease (Fig. 2.3(b)) [10][92][93].

The clinical studies describing the relation between diabetic retinopathy and branching angle are as follows. Branching angles often get impaired in hypertension and disturbed blood flow such as in diabetes and DR [10]. The studies report an increase in the number of obtuse angles formed at the branching, i.e., increase in the average bifurcation angle in a network with the diabetes severity [92][93]. Larger bifurcation angles are related to the decreased blood flow and smaller bifurcation angles with aging and hypertension [80][88][100]. Another study reports larger arteriolar branching angles suggesting the disturbed blood flow, endothelial dysfunction and hypoxia with longer diabetes duration in type 1 diabetes and DR [10]. As highly severe stages of NPDR are related to increased blood flow and the hypertension, decreased bifurcation angles are also reported with it [10].

#### 2.1.6.4 Branching coefficient

The physiological relationship between diabetic retinopathy and branching coefficient may be described as follows. The diametric measurements obtained from the fundus images at different magnifications, with different imaging defects and resolutions may not be able to provide an accurate estimation of a width, hence the use of dimensionless quantity called branching coefficient is proposed. The relative widths of parent and the daughter vessels are compared in terms of quantitative metrices such as Area ratio or Expansion factor $\beta = [(d_1^2+d_2^2)/d_0^2]$ and the Asymmetry ratio $\alpha = [d_2^2/d_1^2]$ [9][99], where $d_0$ is a parent vessel width, $d_1$ is larger width of one of the daughter vessels and $d_2$ is smaller width of the other daughter vessel, as shown in (Fig. 2.3(a)). The optimum value of $\beta$ is determined as 1.0082, as the optimum width of daughter vessel is estimated as 71% of the parent vessel in a healthy blood vessel system, according to the laws of fluid dynamics [101].

The vascular structure is organized in such a way that the shear stresses and work done due to the blood flow are minimized [80]. The vessel network arrangement is based on Murray's law (Murray, 1926) such that the maximum circulatory efficiency with minimal energy losses across the vascular network can be achieved if the width of blood vessel is proportional to the cube root of the blood flow [9][10][88][102][103]. Due to the variation in hemodynamic parameters in diseases, the modified network structure deviates from its geometric ideal and the measurement of such parameters may provide the quantitative assessment of the deformed vessel structure. The energy expenditure increases or efficiency decreases with too large or too small width of

daughter vessels with respect to the parent vessel [10][80][88]. A suboptimal (abnormal) branching geometry is associated with increased work done for blood transport, energy loss, and uneven shear stresses observed in DR [9][10]. The vessel width changes with blood pressure and the peripheral resistance, which in a way changes the branching coefficient [88]. Therefore, the deviation of branching coefficient is associated with endothelial dysfunctions as well as the increased transmural pressure, as observed in diabetes [88].

The previous approaches explored for the determination of branching coefficient are as follows. The retinal branching coefficient (also known as bifurcation optimality or measured in terms of a junction exponent) is defined as $d_1^x + d_2^x = d_0^x$ where $d_1$ and $d_2$ are the widths of daughter vessels and $d_0$ is width of a parent vessel at the bifurcation, with junction exponent x [10][99]. Arterial widths conform to the optimality coefficient (junction exponent with optimal value x=3) at the branching point to optimize the circulatory efficiency and to maintain the constant shear stress in case of healthy subjects [10][88], but it deviates for subjects with hemodynamic abnormalities such as hypertension, atherosclerosis and peripheral vascular diseases related to the abnormal endothelial function which are commonly observed in DR [10][80][88][89]. High cholesterol in type 1 diabetes also affects the venular branching coefficient [10]. As a common procedure, the junction component is calculated from the iterative measurements of parent and daughter vessel widths and the lookup tables, and hence it may be considered sensitive to bias, image quality and width measurement noise [89].

A new parameter, optimality ratio $\gamma = [(d_1^3 + d_2^3)/2 * d_0^3]^{0.33})$ has been defined in [89] equivalent to the junction exponent, which is significantly less sensitive to the diametric measurement noise and bifurcation asymmetry. The article also states that the deviation from optimality ratio value for arterial bifurcations (for symmetrical optimal bifurcation $\gamma = 0.7937$ or x=3) predicts the endothelial dysfunction in diabetes [89][104]. The study reported in [88] derives another branching optimality measurement parameter given as $\rho = [(d_0^3 - (d_1^3 + d_2^3))^{0.33}]/d_0$ which measures the deviation of optimality parameter from normal value of zero [88]. Use of $\rho$ minimizes the error produced in the width measurements, as compared to the junction exponent x.

#### 2.1.6.5 Fractal dimension

Fractal dimension ($D_f$) is determined for the vascular structure which maintains the pattern of self-similarity despite of the magnification level or the scale, in which higher values (between 1 and 2) reflect more complex and dense vessel structure [11][102][105][106][107]. The complexity of retinal vessel network cannot be quantified accurately using Euclidean geometric parameters and hence its characteristic dimensions are determined in terms of fractional powers which describe the non-Euclidean shapes [106][107]. The natural fractals deviate from the ideal fractals and their fractal behavior is limited to a definite scale range. In other words, the $D_f$ estimates not only the filling of the embedding space but the degree or the kind of vascular branching with which the space is filled up [107]. This also allows the comparison of different $D_f$ values as they lie in the same scale range [108]. The scale range of vascular structure

is based on the image resolution, FOV, and method of vessel segmentation.

The clinical studies describing the relation between diabetic retinopathy and fractal dimension are as follows. Fractal dimension significantly increases with the occurrence of hyperglycemia in type 1 diabetes and hence with the severe NPDR or the neovascularization (NV) in severe PDR [11][102][106][107], which suggests the increased complexity of retinal vascular structure. The severity of neovascularization can be quantified more accurately in terms of fractals instead of determining the width or the retinal area covered by the NV vessels [107][108]. A study suggests that the increased $D_f$ is not necessarily the result of proliferative changes (NV) but may be due to the NPDR. Thus, $D_f$ is sensitive to early DR even before the occurrence of PDR [106]. The increased $D_f$ may also suggest the artery-venous differentiation in hypoxic demand to increase the blood flow and tissue perfusion in the network [106]. The studies reported in [10][105][108][109][110], suggest the probability of DR occurrence due to the presence of smaller fractal dimensions with which effectively less area of the retina is covered by the microvasculature leading to the increased risk of occurrence of proliferative retinopathy due to ischemia. Thus, the result explains the relation between $D_f$ and early occurrence of the incident retinopathy. This may suggest that the fractal dimension deviation from normal in both directions, may predict either the cause of the incident retinopathy or its resulting effect. A study [108] also suggests the reduction in $D_f$ as the after-treatment effects.

The previous approaches explored for the determination of fractal dimension are as follows. For the fractal dimension measurement, box-counting method [11][106],

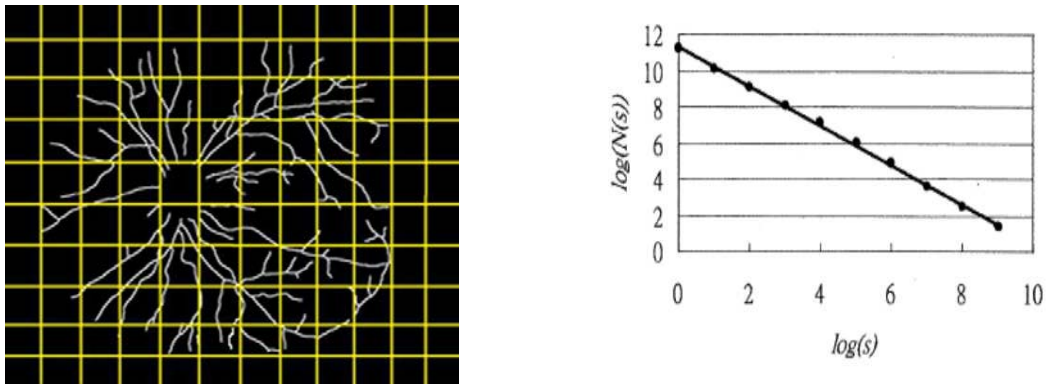


Figure 2.4: $D_f$ analysis: a) Box counting, b) $D_f$ is a slope Db of graph of log2(Ns) vs. log2(s) [11]

sandbox method [108], density-density correlation method [107][108], and the multifractal analysis [110] is used. Initially, image noise, image artifacts, and isolated non-vascular lesions are removed from the vessel segmentation image [33]. The vessel reconnection algorithm is applied to the vessel segmentation image to obtain a connected vessel network [57], as explained in chapter 3. The studies [108][109][110] report that the $D_f$ calculation is independent of the vessel thickness, and the vessel skeleton is more sensitive to the variation in $D_f$. Therefore, the vessel skeletonization is applied [11][106].

In the box-counting method, the image is divided into number of boxes with equal sizes s (Fig. 2.4(a)). The number of boxes which contain any vessel section is counted as $N_s$. The procedure is repeated for box sizes from 1 to $2^k$ pixels where k=0,1,2,3... and $2^k \leq$ size of the image and the corresponding Ns are obtained. For the regression plot of $\log_2 Ns$ vs. $\log_2 s$, a straight line is fitted to the scattered data points using linear regression (Fig. 2.4(b)). According to the Mandelbrot's power

law $N_s = K * s^{-D}$ for each element in the set [11] [107], the slope of the fitted line is determined which gives the fractal dimension of the vascular structure as, $Db = \lim_{s \to 0} \frac{\log_2 Ns}{\log_2 s}$.

## 2.2 Application and Significance of Thesis Work

Retinal vessel network is the only micro-circulation network in a human body which may be imaged non-invasively as a part of an in-vivo analysis. The aforementioned retinopathies and the cardiovascular dysfunctions affect structural as well as the morphologic configuration of the retinal vessel network. Therefore, the automated assessment of morpholoy of retinal vascular beds may help diagnosing the early occurrence or the severity of retinal diseases. The two-dimensional retinal images obtained by color fundus imaging may be utilized for the computer-aided diagnosis using the automated methods described in this research thesis.

The most valuable contribution of this research is the method developed for structural mapping of retinal vessel network [59], as explained in chapter 3. It separates the interwined retinal vessel trees into vessel structures with primary vessel and the corresponding branches. This mapping may be highly useful in the morphologic analysis of individual vessel trees and their classification into arteries and veins. The morphologic changes may be prominent to the arteries or to the veins which may necessitate the classification of vessels into arterial and venous trees with the respective assessment [59], as explained in chapter 3. In our knowledge, this aspect is the very first effort towards the vessel specific structural analysis of retinal blood vessel network.

The vessel segmentation of retinal vessels may not completely segment the entire vessel and as a result a single vessel is split into two or more vessel segments. Such segmentation errors may occur due to shortcomings in the image processing algorithms, and can be exacerbated by image acquisition defects such as imaging noise, low contrast and artifacts [33][49][111]. The quantitative assessment of the interrupted vasculature may produce measurements that are not representative of the underlying anatomy, especially for measurements describing the vessel shape such as tortuosity or those describing the structure such as branching angles. Therefore, the method developed for identification and reconnection of retinal vessel interruptions may allow the formation of a connected vessel network and the measurement of a true morphology of vessels [57], as explained in chapter 3.

The diseases such as diabetic retinopathy (DR) may be identified by the presence of retinal lesions. The features utilized for differentiation and detection of lesions are often based on luminance, local contrast and intensity properties [62]. These features may be affected by imaging defects such as noise, low contrast, non-uniform illumination, and low intensity. Furthermore, the pathological factors associated with diabetes such as diabetes duration, high A1C levels, high blood pressure affect the microvascular structure irrespective of occurrence of DR which suggests the presence of microvascular abnormalities even before the occurrence of lesions [10]. Potentially, the vessel abnormalities may be the precursors of diabetic retinopathy lesions that are commonly detected. Thus, I develop a set of algorithms measuring the morphologic properties of retinal vessels which includes a newly proposed method for tortuosity es-

timation [112] as explained in chapter 3, and quantitative assessment of other factors such as vessel width, branching angle, branching coefficient, and fractal dimension. These methods when implemented on the structurally mapped artery-venous network, may provide a set of morphologic measurements specific to vessels types and vessel generations in a network. This automated tool may provide a set of numerical values representing the present anatomic state of retinal vasculature.

A strong factor behind the high mortality rate due to cerebral malaria (CM) is the high percentage of its false and delayed diagnosis, and inadequate treatment facilities. The clinical definitions of malarial retinopathy (MR), such as retinal hemorrhages may be highly correlated with the signs of cerebral malaria. However, the diagnosis of malarial retinopathy is based on clinical or visual signs and subjective evaluation of patient's retina. Therefore, I develop an automated algorithm which detects the presence and severity of hemorrhage formation specific to the malarial retinopathy [113], as explained in chapter 3. The hemorrhage detection system may be the first effort towards the development of an automated tool providing quick and specific diagnosis of MR irrespective of the available laboratory facilities.

I apply the aforementioned methods on two datasets, viz., a longitudinal study dataset and a malarial retinopathy subject dataset. In the longitudinal study dataset, I measure the vessel morphology properties in fundus images of subjects, available across four time intervals. The behavior of morphologic changes is observed across four time-points with respect to the vessel types (arteries and veins), as well as the vessel generations. The malarial retinopathy subject dataset is utilized to detect

the presence of blood hemorrhages by the automated method. The results of the experiments are presented.

The major contribution of this thesis includes the development of automated methods for; 1) Identification and separation of retinal vessel trees for individual vessel analysis, 2) Automated quantification of morphologic characteristics of retinal vessels for quick and precise measurement, 3) Automated quantification of vessel morphology with respect to arteries and veins, and 4) Analysis of two datasets, a) malarial retinopathy subject dataset, b) longitudinal study dataset.

The ability of the automated methods to quantify the retinal vessel specific properties may enable the individual vessel analysis as an alternative to a time-consuming and subjective clinical evaluation, or to a quantitative morphology characterization averaged over the entire vessel network. The objective evaluation may indicate the progression of retinopathies precisely and may help characterizing normal and abnormal vascular patterns with respect to arteries and veins. This may enable a quick diagnosis, treatment availability, prognosis, and facilitation of clinical health-care procedures in remote areas.

# CHAPTER 3
# METHOD AND MATERIALS

## 3.1 Research objectives and a rationale

Abnormalities in the vascular pattern of a retina such as morphologic changes in vessel shape, branching pattern, width, tortuosity, or the appearance of retinal lesions may be associated with the occurrence of retinopathies or cardiovascular diseases. Thus, an automated quantitative analysis of changes in vessel morphology may help indicating the clinical signs of aforementioned retinopathies, describing their early occurrence or severity. The responses obtained from different types of retinal vessels, i.e., arteries and veins, may be variable to retinopathies and their measurement may lead to a more precise diagnosis compared to that by the average response accounted for the entire vessel network. The objective of this research thesis is to develop a set of automated methods for analyzing the retinal vessel network to provide its morphologic description. Specifically, I propose to measure automatically the vessel specific geometric descriptors of the retinal vasculature, and to detect the presence of retinal lesions, in order to characterize normal and abnormal vascular patterns describing the retinopathy signs.

### 3.1.1 Specific Aims

A1. To develop a set of automated methods to correct for interrupted vessel segmentation, identification, and artery-venous classification, of retinal vessels.

A2. To develop a set of automated methods to measure the morphologic properties of retinal vessels such as width, tortuosity, branching pattern, and fractal dimension to aid the procedure for the retinopathy diagnosis.

A3. To develop an automated method describing the presence of blood vessel hemorrhages, in order to differentiate between normal subjects and those with high probability of malarial retinopathy.

A4. To evaluate the accuracy of proposed algorithms on respective datasets, consisting of subjects with a longitudinal study data, and subjects previously diagnosed with malarial retinopathy.

I propose a set of automated methods in order to analyze the retinal vessel network and to quantify its morphologic properties with respect to arteries and veins, in two-dimensional color fundus images. The analytical methods include; 1) Formation of a well connected vessel network, 2) Structural mapping of a vessel network, 3) Artery-venous classification, and 4) Blood vessel hemorrhage detection. The quantification methods include vessel morphology analysis based on the measurement of tortuosity, width, branching angle, branching coefficient, and fractal dimension. The aforementioned morphologic parameters are measured with respect to arteries and veins separately in a vessel network. The methods are validated with the manually annotated retinal fundus images as a ground truth. The ability of our methods to quantify the vessel specific properties may enable the individual vessel analysis as an alternative to a time-consuming and subjective clinical evaluation, or to a quantitative morphology characterization averaged over the entire vessel network.

## 3.2 Identification and reconnection of interrupted vessels in retinal vessel segmentation

### 3.2.1 Introduction

Morphologic assessment of the retinal vessel network has the potential to provide insight into retinal diseases. Clinicians visually inspect the eye fundus for the diagnosis and assessment of retinal dysfunctions such as diabetic retinopathy, retinopathy of prematurity and systemic abnormalities such as cardiovascular diseases [30],[104]. Several important morphologic characteristics of retinal vessel structure have been described in the literature including vessel width, tortuosity, branching angle and the artery to vein diameter ratio [112],[86],[114].

Identifying the vessel network in retinal fundus images usually involves the following steps: The first step in such an analysis is vessel segmentation [33][49][51][54]. This step may not completely segment the entire vessel and as a result a single vessel is split into two or more vessel segments as illustrated in (Fig. 3.1). Such segmentation errors may occur due to shortcomings in the image processing algorithms, and can be exacerbated by image acquisition defects such as imaging noise, low contrast and artifacts [33][49][111]. The quantitative assessment of the interrupted vasculature may produce measurements that are not representative of the underlying anatomy, especially for measurements describing the vessel shape such as tortuosity or those describing the structure of vessel network such as branching angles.

There is a dearth of methods for reconnecting the interrupted vessel segments to obtain a connected vessel structure. A method described in [56] identifies the

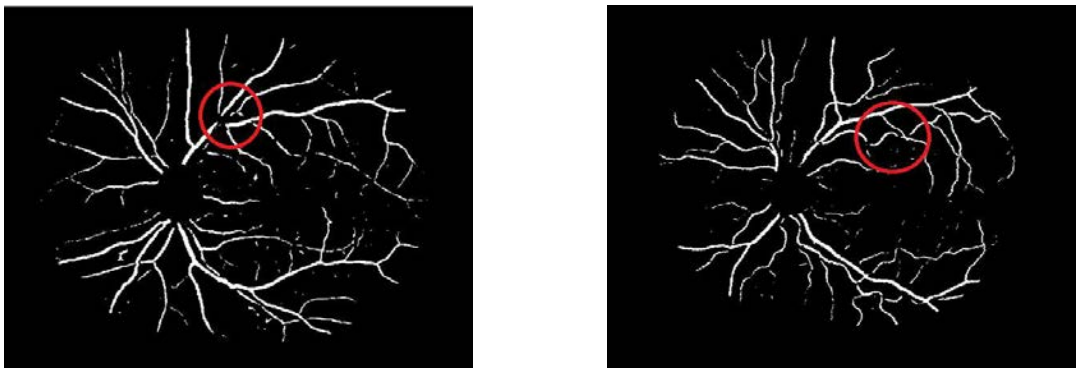

Figure 3.1: Interrupted vessel segmentation

disconnected vessel segments which are assumed to be facing each other and have similar morphologic properties at the respective end points, viz. diameter, direction, intensity and distance between two end points. The algorithm connects the vessel segment end points based on scoring functions that exceed a certain threshold. A supervised method presented in [111] uses two separately trained classifiers for segmenting narrow and large width vessels. It utilizes dynamic programming to connect the interrupted vessels and determines the validity of connection based on a supervised cost function. The reconnection method for cerebral vessel segmentation in three-dimensional MRA images is explained in [115]. The primary vasculature and the interrupted vessel segments are identified and are reconnected using a graph search based on vesselness parameters. The final segmentation is obtained using a level set method. However, the method is tested on only 2 MRA images.

The methods [111][56] may be limited by the parameters utilized for the identification of vessel interruption location. The distance parameter may limit the extent

of region inside of which two end points are considered eligible for reconnection and may not be able to reconnect two segments interrupted with longer gaps. It may also restrict the connection of two end points belonging to the same vessel but with differing properties such as abrupt direction change at the interruption, change in diameters or intensities at two end points due to low contrast or non-uniform illumination effects, which may result in the end points of vessel segments eligible for the true reconnection, to be matched incorrectly or vice versa.

A method could be developed based on finding the connecting vessel path which exists with low gray scale pixel intensities on the vessel segmentation image, and therefore shows the interruption when the image is thresholded for binarization. This method may be able to find a connecting path independent of the matching criteria between two end points at the location of interruption.

Therefore, I develop an automated method for identification of vessel interruptions in two-dimensional vessel segmentation images and propose a graph search algorithm for the reconnection process. I introduce the method and evaluate it on a dataset of 25 retinal vessel segmentation images. I present the results in terms of a performance index that measures the reconnection performance of the automated method with respect to the manual reconnection process.

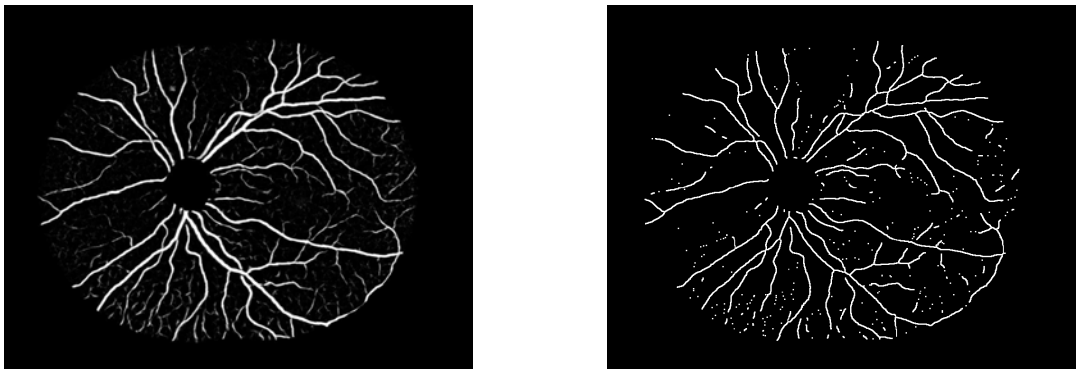

Figure 3.2: Image preprocessing: a) Vessel segmentation, b) Vessel network skeleton

### 3.2.2 Method

#### 3.2.2.1 Identification of the primary vasculature and interrupted vessel segments.

The retinal blood vessel segmentation is obtained from the color fundus image using a previously published method developed by our group [33]. This is a supervised method based on a pixel classification approach that uses a Gaussian filter set for feature extraction. Each pixel in the fundus image is classified with a kNN classifier to produce vessel segmentation in terms of a gray level vessel probability map. In the vessel segmentation image (Fig. 3.2(a)) the region of optic disc is masked to avoid morphologic complications due to irregular and highly tortuous blood vessels at the optic disc.

The vessel probability map is binarized using Otsu thresholding method [116]. The binarized image is processed using morphologic operations, viz., skeletonization, thinning, and spur removal to produce a vessel network skeleton [117] (Fig. 3.2(b)).

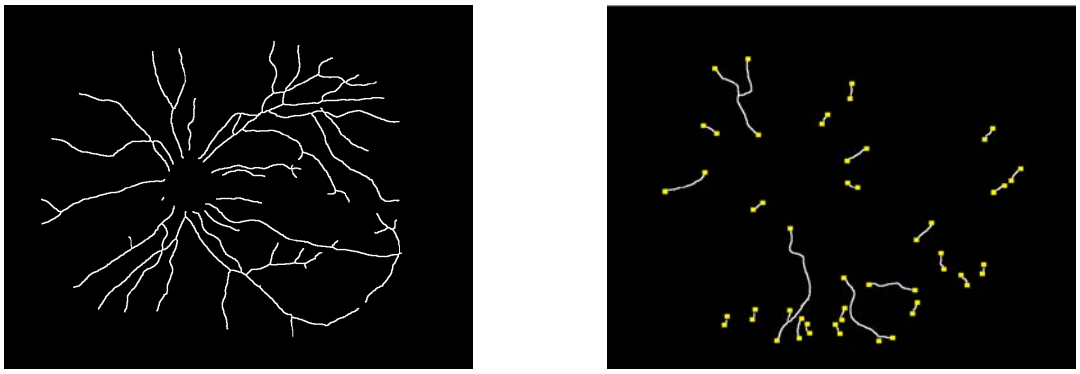

Figure 3.3: Separation of vessel network: a) Primary vessel network, b) Interrupted vessel segments with end points marked in yellow

The primary vasculature and the interrupted vessel segments are identified as follows. A depth first search (DFS) approach is used to traverse the skeletonized vessel tree completely, in order to identify the primary vessel network, as shown in (Fig. 3.3(a)). Once the primary vessel network is identified, it is masked from the vessel network skeleton (Fig. 3.2(b)), to obtain the vessel segments not connected to the primary structure. A connected component analysis is utilized to filter out the disconnected vessel segment skeletons with size less than 10 pixels. This operation not only filters the noise out but also removes small vessel segments which are clinically insignificant. The end point of each disconnected skeletonized vessel segment is detected if a skeleton pixel contains one and only one foreground pixel in its 3x3 neighborhood. It finds all end points for each of the interrupted vessel segments (marked yellow in Fig. 3.3(b)).

#### 3.2.2.2 Reconnection of interrupted vessel segments to the primary vasculature.

The first step in the reconnection procedure is to identify the end point of a vessel segment which is to be reconnected back to the primary structure. The disconnected vessel segment may have two or more end points (considering possible bifurcations). From the empirical observation, it appears that the end point of the segment to be reconnected is the one which is nearest to the center of optic disc (OD). Thus, the Euclidean distances of the end points belonging to a single vessel segment, from the OD center are determined and the end point closest to the OD center is selected for segment reconnection. In case of a vessel segment with two end points (E1, E2) at similar distances from the OD center (e.g., for a segment which is radially parallel to OD), the algorithm maintains a threshold value for the difference between such distances. If the absolute difference between two distances (OD-E1 and OD-E2) is below the threshold, i.e., the segment is radially parallel to OD, the end point which is nearest to the primary vessel structure is selected for the reconnection purpose. The threshold was empirically determined to be 20 pixels.

I use Dijkstra's graph search algorithm (See Appendix) in order to find the connecting path between the disconnected segment and the primary vasculature. The use of shortest path search algorithm to find the connection path is based on a theoretical assumption that the retinal vessels in the segmentation image consist of an intensity ridge at the vessel centerline and the tapering intensity response towards the vessel edges (Gaussian approximation) [30]. Therefore, I propose to find a mini-

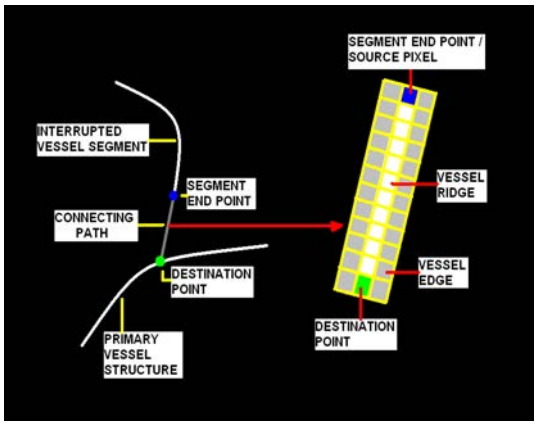


Figure 3.4: Connecting path

mum cost path corresponding to the vessel ridge, starting from the segment end point selected for reconnection, to the destination point on primary vasculature (Fig. 3.4).

The centerline of a vessel consists of a ridge or the high intensity pixels as compared with the pixels at vessel edges. Therefore I choose the highest intensity pixel in 7x7 neighborhood of the selected end point pixel of the disconnected segment. This highest intensity pixel becomes a source pixel for the graph search algorithm (Fig. 3.4). The vessel segmentation image structure is converted into a graph *G(V,E)* in which the source pixel forms a source node $(V_s)$ and other pixels form other nodes $(V_n)$ of the graph. The edge cost of an edge *(E)* between any node of the graph and a node in its 3x3 neighborhood (forming a node pair), is given by the normalized addition of intensity cost and direction cost. The intensity cost is defined as the absolute difference of intensities of two pixels represented by two respective nodes. The direction cost is defined as the absolute difference between the vector directions of two pixels with respect to the direction of the vessel segment tracked until that

point. Therefore, considering $(V_s)$ as one of the nodes in a pair and the other node in its 3x3 neighborhood, the least edge cost would be represented by an edge connecting the source node $(V_s)$ and a node (in the 3x3 neighborhood), which has the smallest addition of intensity and direction costs. In other words, this node among all the neighborhood nodes, represents the most similar intensity and similar vector direction with respect to the source node $(V_s)$.

For the Dijkstra's algorithm, I define the minimum cost path to be consisting of edges which represent the smallest total cost of the path starting from source node to destination node which is a pixel on the primary vessel structure (Fig. 3.4). Thus, the Dijkstra's algorithm starts at the source node and goes on adding the nodes which represent most similar intensity with respect to the source node and the most similar direction with respect to the vessel segment connection tracked until that point. The algorithm terminates when the latest node added, represents the pixel on primary vessel structure.

The vessels are segmented in such a way that the high intensity pixels define a ridge along the vessel, i.e., the approximate vessel centerline. Thus, the minimum cost path (consisting of high intensity pixels) obtained by the graph search algorithm represents the ridge pixels on the vessel connecting the end point of the disconnected vessel segment to the primary vessel structure (Fig. 3.4). Therefore, the algorithm is able to reconnect the interrupted vessel segment as long as the connecting path between the segment and the primary structure exists on the vessel segmentation image (i.e., the pixel intensities on the connecting path lie between 1 to 255, for 8-bit

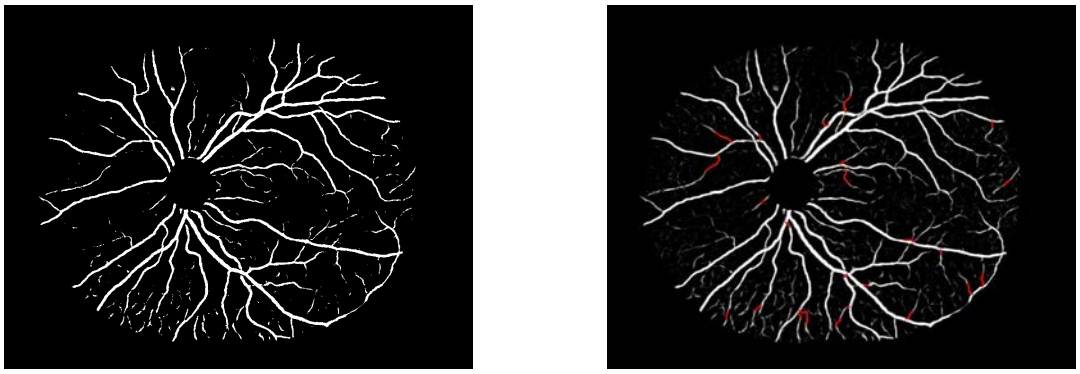

Figure 3.5: Reconnection: a) Input vessel segmentation image, b) Reconnected vessel network

image), irrespective of the low pixel intensities on the path. Such a path always exists (may be with lower intensities) unless there is no real vessel, with rare exceptions. The algorithm connects each of the interrupted vessel segments to the primary vessel structure with the connecting path as shown in (Fig. 3.5(b)), marked in red, and in (Fig. 3.6).

The connecting path is evaluated and confirmed if both of the following constraints are met:

Tortuosity constraint is evaluated as follows. Based on a theoretical assumption that a connecting path obtained over a short distance does not possess a highly tortuous course, I measure and compare the tortuosity [112] of connecting path with an empirically determined tortuosity threshold, such that the reconnection path with tortuosity greater than 1.5 is rejected.

Connection strength constraint is evaluated as follows. The connection strength of the path is measured as the average intensity of pixels from the segmentation image,

present on the connecting path. I determine the connection strength and compare it with an empirically determined intensity threshold, such that the path with connection strength below the average intensity of 15 (for 8-bit images) is rejected.

If the connecting path possesses the tortuosity below the tortuosity threshold and the connection strength above the average intensity threshold, the connection is confirmed. If any of the criteria is not satisfied, the algorithm rejects this connection and the corresponding end point of the vessel segment. The algorithm then performs the reconnection and evaluation procedure with respect to another end point of the same vessel segment, which exhibits the second shortest distance from the OD center. If none of the end points of the given vessel segment and its respective connection is confirmed, the vessel segment is disqualified for the reconnection and remains disconnected.

### 3.2.3 Results

I applied the proposed method to a dataset of 25 vessel segmentation images (Image size: 1000x800) selected randomly from a population of normal and diabetic retinopathy subjects. To obtain the ground truth, the interrupted vessel segments were connected back manually to their point of origin at the primary vessel structure, by a medical expert. The quantitative analysis was performed by comparing the true vessel segment connections obtained by the automated method and those obtained by the ground truth. The number of independent, connected vessel trees along with the interrupted vessel segments was 695 for the set of 25 interrupted vessel segmentation images. For manually connected images and automatically connected

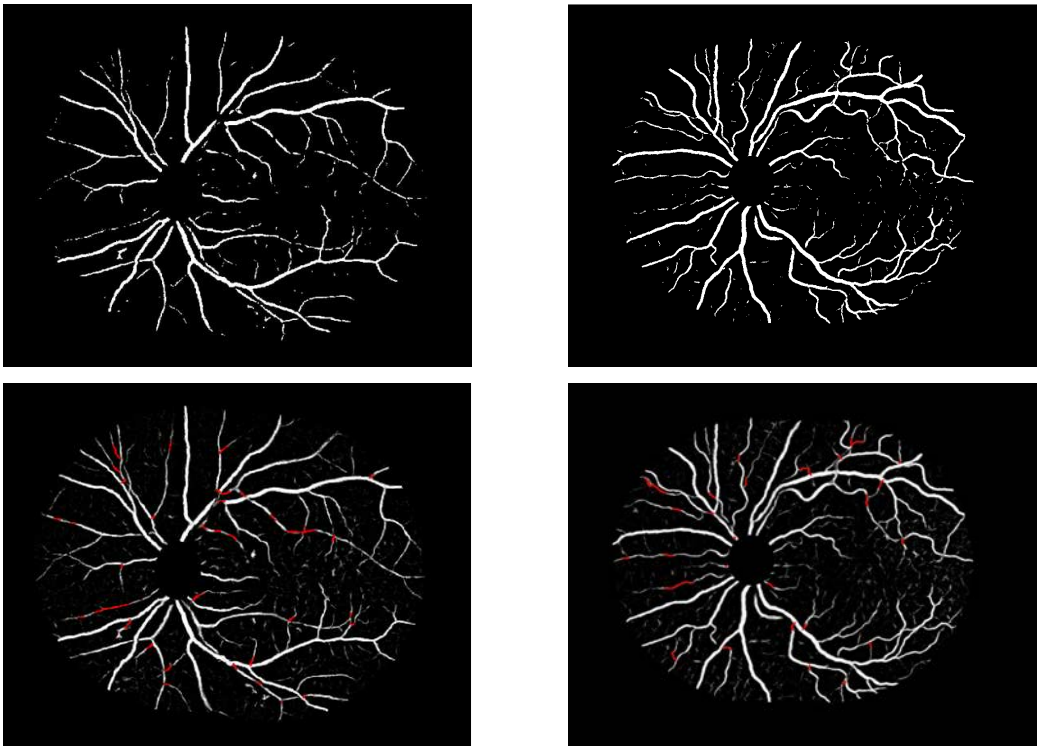

Figure 3.6: Input vessel segmentation image and a reconnected vessel network

images this number reduced down to 205 and 295 respectively, considering only the true vessel reconnections obtained by the automated method when compared with the ground truth. I define a performance index as the ratio of number of true vessel reconnections obtained by the automated method to the number of true vessel reconnections obtained by the ground truth. The performance index of 81.63% shows the reconnection performance achieved by the automated method compared to the ground truth. An average of 2 false positives was obtained per image.

To analyze the effect of automated vessel reconnection procedure on the measurement of morphologic parameters of vessels, mean vessel tortuosity of each of the 25 images was measured using a method developed in the thesis [112], as described in chapter 3. The set of 25 images was graded by two masked ophthalmologists and the images were ranked from 1 to 25 representing the lowest tortuosity image by rank 1 and the highest tortuosity image by rank 25. The standard ranking was determined as the average of corresponding rankings obtained from two ophthalmologists. The mean tortuosity values measured for the set of 25 images obtained from interrupted vessel segmentation, those from automated vessel reconnection procedure, and those from manual reconnection procedure (ground truth), were ranked according to the tortuosity indices (TI). Three Spearman's ranking correlation coefficients were obtained for correlations between ophthalmologist's standard ranking and the ranking obtained from interrupted vessel images ($r_s$=0.58), automatically reconnected vessel images ($r_s$=0.68), and manually reconnected vessel images ($r_s$=0.72), respectively. Results show the improvement in the correlation coefficient for automated reconnection pro-

cedure which approaches the coefficient for the ground truth, over the coefficient for interrupted vessel segmentation.

The average running time per image starting at the readily available vessel segmentation to the completion of vessel reconnection process was 3 minutes, when processed in MatLab environment on a standard personal computer with Intel core 2 Duo processor, running at 3 GHz.

### 3.2.4 Discussion

The results show that the number of interruptions in the automatically connected vessel images is reduced significantly and it approaches the value obtained for manually connected vessel images. It not only enhances the accuracy of segmentation but also provides a connected vessel structure that may represent an improvement in measurement of morphologic properties, such as vessel tortuosity.

The method in this paper utilizes the existing vessel segmentation path for the vessel reconnection, irrespective of the low valued pixel intensities on the connecting path, vessel segment intensities, directions and diameters. The connecting path is not constrained by the distance between the interrupted vessel segment and the primary vessel structure, which makes the algorithm able to connect the vessel segment disconnected even by a longer gap.

The method of Forkert et al. [115] may not be able to find the end point of the segment in advance which is to be reconnected, and may lead to an erroneous path formation between two anatomically separate vessels. The other source of erroneous connection may be the possibility of finding two end points eligible for the connection

based on a cost function, which are anatomically disconnected from each other. As the method identifies the end point to be reconnected in advance, and finds the connecting path based on the existing vessel segmentation, the path formation may logically be more appropriate. Forkert's method does not provide any automated means of verifying the resultant connecting path as provided by our method based on measures of tortuosity and connection strength. Such a procedure is required in order to discard erroneous connections.

Potential drawbacks are the following: the vessel segments are reconnected only if completely disconnected from the primary structure and not those vessels segments which are connected with the primary structure at any one of the segment ends but not the other, as such reconnections may produce erroneous vessel linkages. I hope to investigate such vessel interruptions i.e., one possible solution is to obtain the branching and crossing (B/C) point information from the fundus image and driving the connecting path propagation towards the B/C point as a heuristic.

### 3.2.5 Conclusion

I have developed an automated method for identifying the interruptions in retinal vessel segmentation and means of reconnecting the vessel segments to the primary vessel structure to obtain a connected retinal vessel network. The application of the algorithm to a dataset of 25 vessel segmentation images resulted into a reduction in vessel interruptions suggesting that the method has potential in providing a connected vessel network for presenting a true and a consistent morphologic analysis.

## 3.3 Automated method for identification and artery-venous classification of vessel trees in retinal vessel networks

### 3.3.1 Introduction

The connected vessel segmentation network obtained in the previous step [57] enables the morphologic analysis of retinal vessel network as well as the individual vessel trees. Several automated techniques were reported to quantify the changes in morphology of retinal vessels (width, tortuosity) indicative of retinal or cardiovascular diseases. Some of the techniques measure the vessel morphology as an average value representing the entire vessel network, e.g., average tortuosity [42]. However recently, the vessel morphology measurement specific to arteries or veins was found to be associated with the disease occurrance. A plus disease may result into increase in arterial tortuosity relative to that of veins indicating the onset of retinopathy of prematurity (ROP). [58]. The arterial narrowing, venous dilatation and resulting decrease in artery-to-venous width ratio (AVR) may predict the future occurrence of a stroke event or a myocardial infarct. [114]. Unfortunately, the detection of minute changes in vessel width or tortuosity specific to arteries or veins may be difficult in a visual evalution by an ophthalmologist or by a semi-automated method, which is laborious in clinical practice. Therefore, an automated identification and separation of individual vessel trees and the subsequent classification into arteries and veins may be required for vessel specific morphology analysis [118].

Vickerman et al. presented a method for identification and separation of reti-

nal artery and venous trees from fluorescence angiogram images where arteries are filled first before veins [118]. This AV separation is propagated into the entire vessel network using morphologic and connectivity features of retinal vessels. A method for structural analysis of intra-cranial vessels from three-dimensional computed tomography (CT) and magnetic resonance angiogram (MRA) volumes has been reported by Aylward et al. [119]. It provides a spatial mapping of vessels known as spatial graphs, using blood vessel structure, vessel positions, and vessel paths. Several arterio-venous (AV) classification methods have been proposed based on the analysis of localized vessel structure. Rothaus et al. proposed a semi-automatic constraint optimization approach based on artery-venous crossing properties and anatomic characteristics [120]. The central light reflex of retinal arteries was used as a distinguishing factor by Tramontan et al. [121]. Grisan et al. suggested a method based on the division of the posterior pole into four regions of interest (ROI) and the classification of blood vessels in each region using the color properties of the vessels [122]. Vazquez et al. presented a clustering approach based on the feature sets obtained from retinal vessels[123]. A method by Kondermann et al. extracts a feature set from vessel profiles and local image intensities with respect to the vessel centerlines [124]. This method uses a support vector machine and neural networks for classification. A supervised classification approach was demonstrated by Niemeijer et al. in which the algorithm was trained on annotated vessel segments for feature extraction and the trained classifier was used to separate arteries from veins in a test dataset [114]. However, so far these automated methods only allow AV classification constrained to

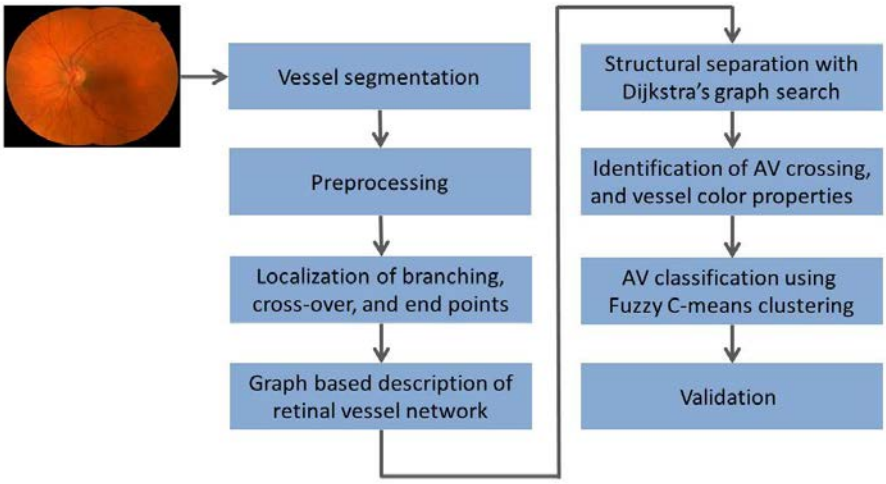


Figure 3.7: Overview of the steps in proposed method

a small region around the optic disc but not the entire retinal image. [114][122].

An automated method is introduced for structural mapping of retinal vessels by modeling the vessel segmentation into a vessel segment map and identifying the vessel trees based on graph search. Artery-venous classification then use color features. I evaluated the method on a dataset of 50 fundus color images from 50 subjects and compare the results to manual annotations.

### 3.3.2 Method

An overview of the approach is described in (Fig. 3.7). Each of the steps is explained in detail as follows.

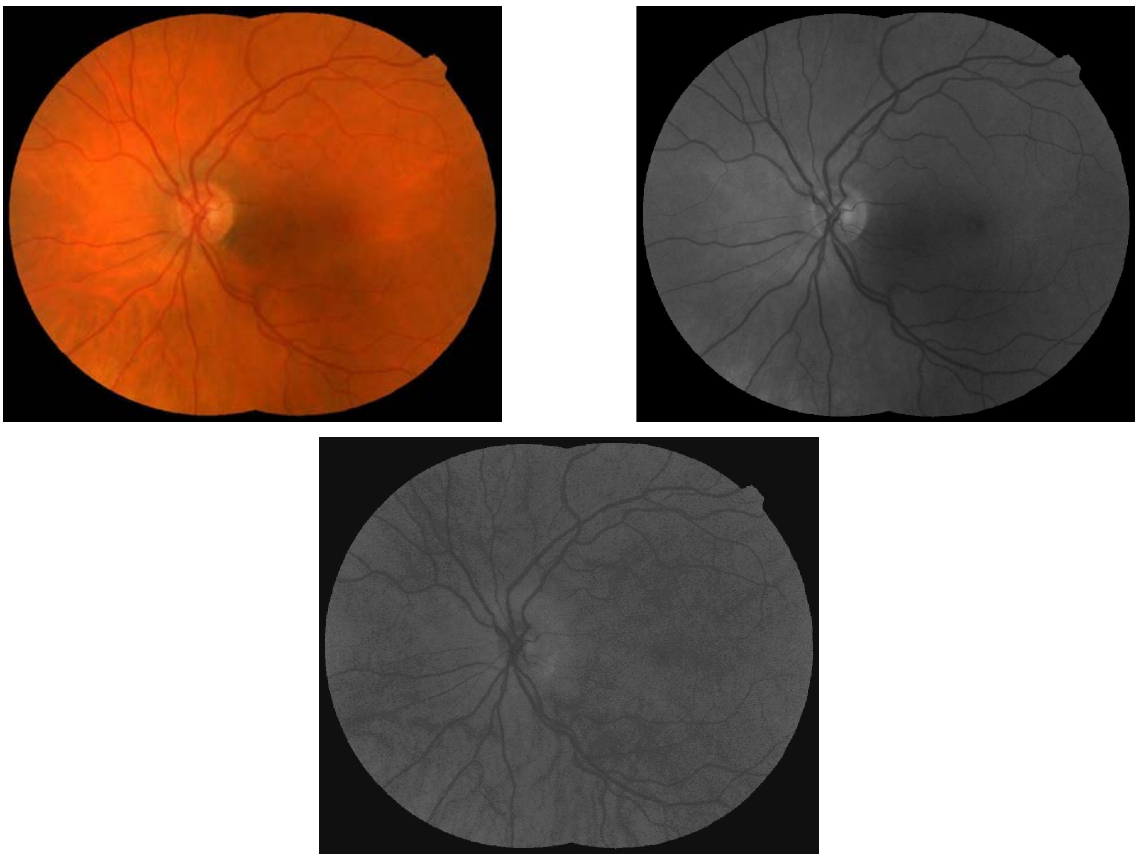

Figure 3.8: Input images: a) Fundus image b) Green channel image c) Hue channel image

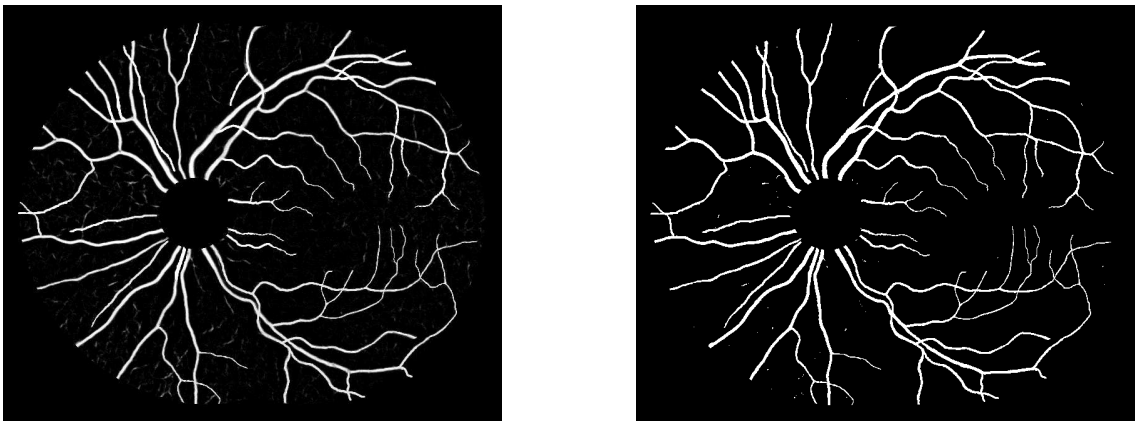

Figure 3.9: Preprocessing a) Vessel probability image b) Binary image

3.3.2.1 Vessel segmentation and image preprocessing

Two-field fundus images of the same eye are registered by mosaicing [125] (Fig. 3.8(a)). The corresponding green channel image (Fig. 3.8(b)) and hue channel image (Fig. 3.8(c)) are shown. The retinal vessels are segmented using the standard approach (supervised pixel classification approach using a Gaussian filter set and classification by a k-nearest neighbor classifier [33]). The resulting vesselness image represents the likelihood of each pixel belonging to a vessel (Fig. 3.9(a)). The optic disc (OD) region is masked manually using standard size mask to reduce ambiguities from the highly tortuous and intertwined vessel patterns at the OD region.In order to trace the vessel path and obtain structural mapping, a connected binary vessel image is required which may be obtained using a previously developed method for vessel reconnection based on graph search [57].

The binary vessel image (Fig. 3.9(b)) is generated from the vessel probability image using Otsu's thresholding method [116]. The Otsu threshold minimizes the

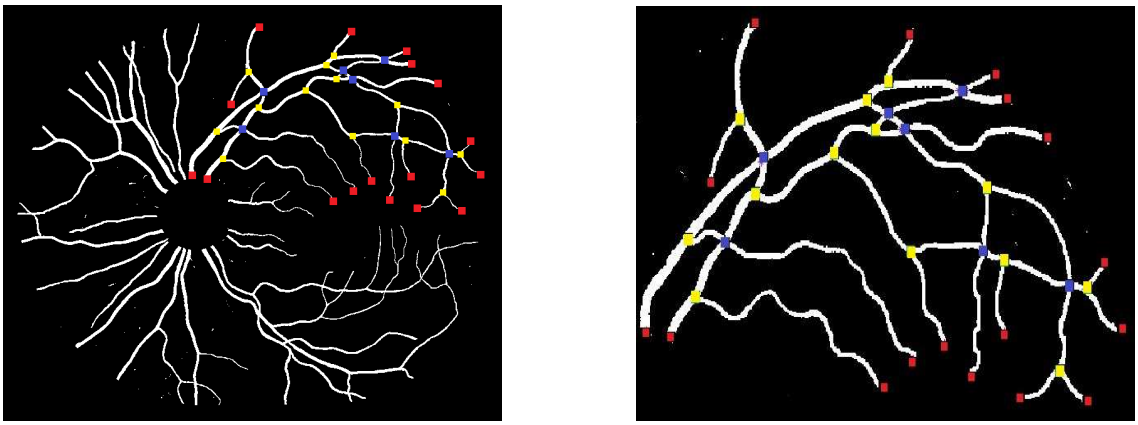

Figure 3.10: Branch, crossing, and end points: a) Vessel network b) Vessel tree [Vessel width is enlarged for visualization]

intra-class variance for the foreground (vessel) and the background (non-vessel region) classes. Next, the vessel skeleton is obtained by applying mathematical morphology reducing the vessel to a centerline of single pixel width. [117].

#### 3.3.2.2 Localization of branch points, crossing points and end points

In order to represent the vessel structure in terms of a graph, the vessel skeletons have to be converted into vessel segments separated by interruptions at the branch- and crossing points. Their start and end positions are determined as follows. Each of the centerline pixels on the vessel skeleton is analyzed for its 3x3 neighborhood, and branch and crossing points are detected as centerline pixels with more than 2 neighbors. The detection of vessel end points is required for the graph search and they are determined as the centerline pixels with only one neighbor.

The Fig. 3.10(a) (vessel network), and Fig. 3.10(b) (vessel tree), show the end

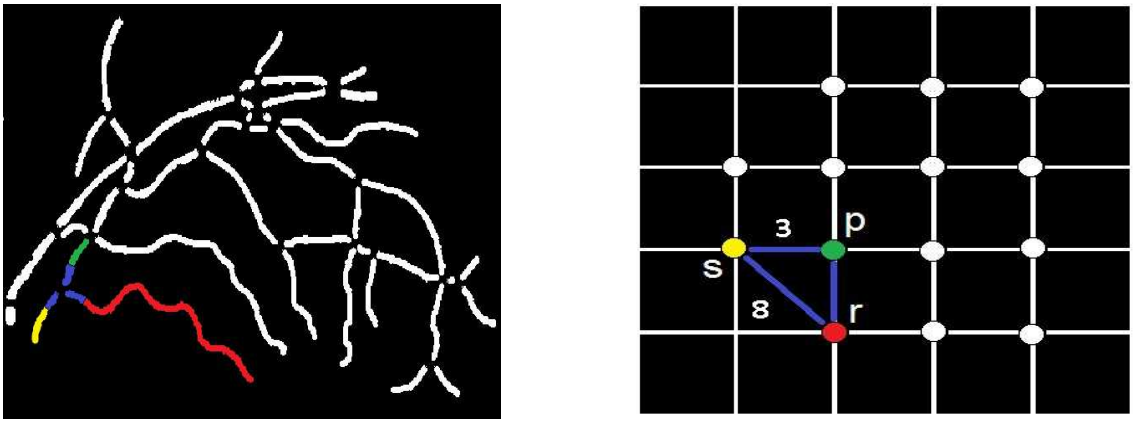


Figure 3.11: Graph formation: a) Vessel segment map [Vessel width is enlarged for visualization] b) Representative graph structure

points (red), branching points (yellow), and crossing points (blue).

3.3.2.3 Graph based description of a retinal vessel network

In order to construct a graph, the vessel segment map (Fig. 3.11(a)) is obtained by removing branch and crossing points on vessels in a binary image (Fig. 3.9(b)), resulting in a group of discrete vessel segments representing a vessel tree.

A vessel consists of number of smaller vessel segments linked together [126]. Three attributes, i.e., orientation, width, and intensity of vessel segments corresponding to a single vessel, have similar characteristics [127] within a vessel tree. The distribution of the orientation between the neighboring segments follows a smooth continuous function. The adjacent vessel segments exhibit fine continuous variation in widths, with some exceptions such as microaneurysms and vessel beading. Similarly, there is a gradual intensity transition between the neighboring segments.

A vessel subtree is identified by selecting a group of segments from the vessel

segment map (Fig. 3.11(a)), based on the similarity between these segments. Three features are used 1) segment orientation, 2) segment width, and c) segment intensity (in the green channel), and these are the costs associated with each segment: segment orientation cost, segment width cost, and segment intensity cost. The features are measured at the end regions of each vessel segment, with skeletal length of 15 pixels from each end. Specifically, orientation is expressed as the angle (in radian) the segment end region makes with the positive direction of X-axis, a measurement between [0,$\pi$]. The width (in pixel) is measured as a median value of 15 measurements of diametric length between the vessel edges, and passing through the skeleton pixels of the end region. The intensity is measured as a median value of green channel pixel intensities at the segment end region. The median value of the width and that of the intensity measured for each vessel segment are normalized by the respective maximum values obtained across the vessel tree.

To convert the vessel segment map (Fig. 3.11(a)) into a connected graph structure, connecting neighboring vessel segments are identified using the branch and crossing-point information. In the derived graph structure $G(V, E)$ (Fig. 3.11(b)), nodes $V$ represent the corresponding vessel segments from the vessel segment map, and each edge $E$ connecting any two nodes, represents the costs with respect to absolute difference in orientation ($E_O$), absolute difference in width ($E_W$), and absolute difference in intensity ($E_I$), at the end regions of two vessel segments represented by two nodes. At any instant during the graph search, only one of the three difference costs is assigned to the edge, as explained in algorithm 1. In fig. 3.11(a) three vessel

segments are colored in yellow, green, and red as an example. The end regions connecting the three segments are marked in blue. The corresponding graph structure (Fig. 3.11(b)) shows a seed node '$s$' in yellow, identified as the node which represents the root vessel segment in a vessel tree (a vessel segment nearest to the optic disc, marked yellow in (Fig. 3.11(a))). Two other nodes '$p$' (green), and '$r$' (red) are marked in respective colors representing the vessel segments. The edge (marked in blue) connecting any two nodes (e.g., '$s$' and '$r$') represents the costs with respect to three parameter differences associated with two respective vessel segments. For an illustration, the orientation of yellow segment is more similar to that of green segment than the red segment (Fig. 3.11(a)). Therefore, the orientation difference cost of the edge between yellow and green node ($E_O(s,p)$=3) is lower compared to the orientation difference cost of the edge between yellow and red node ($E_O(s,r)$=8) (Figure not to scale).

#### 3.3.2.4 Dijkstra's graph search

Dijkstra's algorithm is utilized to identify a vessel subtree. Equation 3.1 explains the operation of Dijkstra's algorithm which searches for a minimum edge cost path 'dist[t]' that connects any node '$t$' with the seed node '$s$' by minimizing the sum of edge costs '$E$' between intermediate nodes '$q$' on the path (e.g., $E(q,t)$).

$$dist[t] = \min_{q \in S} [dist[q] + E(q,t)] \tag{3.1}$$

3.3.2.5 Structural separation of vessel trees

The Dijkstra's algorithm determines the minimum edge cost path (smallest sum of edge costs on the path) 'dist[e]' from seed node '$s$' to each of the end point nodes '$e$' representing vessel end point segments (marked red in (Fig. 3.10(b))), by selecting the intermediate nodes '$q$' which minimize the sum of edge costs on the path (Eqn. 3.2), i.e., the intermediate vessel segments which minimize the parameter differences along the path. The value of 'dist[e]' for each '$e$' is normalized by the number of nodes (vessel segments) on the path, given as '$dist_{norm}$[e]'.

$$dist[e] = \min_{q \in S} [dist[q] + E(q, e)] \tag{3.2}$$

The theoretical assumption is that the true vessel path is governed by the lowest edge cost path '$dist_{norm}$[e']' among all the edge cost paths '$dist_{norm}$[e]' determined for the respective end point nodes '$e$' (Eqn. 3.3). In other words, the path with lowest sum of edge costs '$dist_{norm}$[e']' along the total path length, from seed node '$s$' to one of the end point nodes ($e'$), would be the path with least parameter differences between the vessel segments, i.e., most similar segments on the path (segments marked in red (Fig. 3.12(a))), comprising a true vessel. The pseudocode for the structural mapping using Dijkstra's graph search is given in algorithm 1. The graph edges are initialized with '$E_O$', due to a higher robustness in the 'orientation measurement' irrespective of image resolution and image noise.

$$dist_{norm}[e'] = \min\left(dist_{norm}[e]\right) \tag{3.3}$$

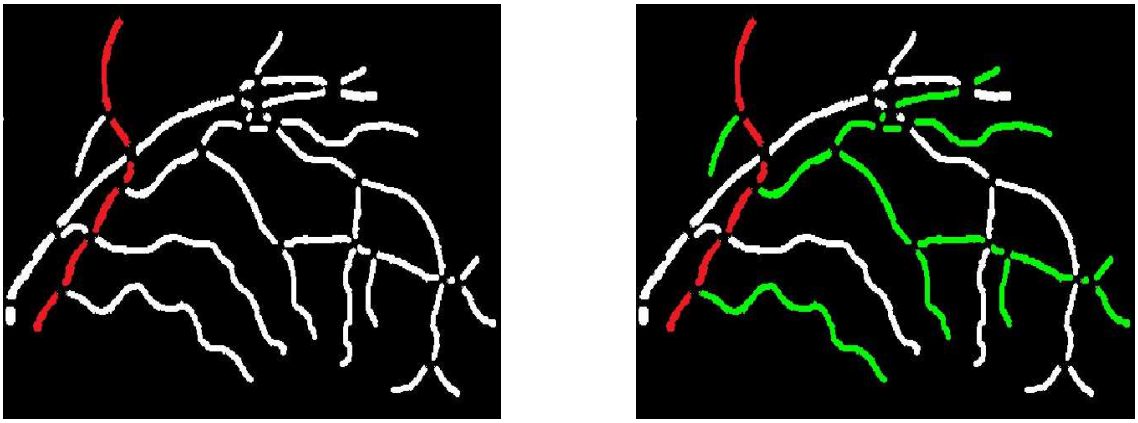

Figure 3.12: Structural mapping: a) Vessel segment map showing the true vessel path b) True vessel path with branches

Utilizing the branch and crossing point information (Fig. 3.10(b)) along with the selected true vessel path, the branches and sub-branches are determined using the same principle, as above. A true or primary vessel path (marked in red), the branches and the sub-branches (marked in green) in a vessel tree are mapped as shown in Figure (Fig. 3.12(b)). The primary vessel, its branches and sub-branches in each vessel tree may be identified by numerical or color labels as shown in (Fig. 3.13(b)).

#### 3.3.2.6 Identification of artery-venous crossing and color properties specific to arteries and veins

I propose an automated AV separation algorithm based on structural mapping, which classifies the vessel trees into arteries and veins, using vessel color features as well as the anatomic property of artery-venous (AV) crossing. This property proposes that the crossing of two retinal blood vessels imaged on a two-dimensional fundus

**Algorithm 1** Structural mapping using Dijkstra's graph search

Given a graph '$G$', with any pair of nodes a and b $\in$ '$V$', and edge '$E$' of the form $E(a,b) = E_O(a,b)$ or $E_W(a,b)$ or $E_I(a,b)$. The seed node = '$s$', and each end point node = '$e$'.

**for** i = each end point node $e$ **do**
    S = set of explored nodes in $G$, Q = set of unexplored nodes in $G$
    For each node u$\in$S, dist[u] = minimum distance from $s$, and previous[u] = parent node, are stored.
    **for** each node $V$ in $G$ **do**
        dist[$V$] = infinity, previous[$V$] = undefined
    Initially, S=$s$, and dist[$s$] = 0
    **while** u $\neq$ i: **do**
        u := node in Q with at least one edge from S, and with smallest dist[]; remove u from Q, and add u to S
        **for** each neighbor v of u: **do**
            **Comment:** Initialization of edge costs with '$E_O$'
            Initialize $E(u,v)$=$E_O(u,v)$
            **if** dist[v] > dist[u] + $E(u,v)$ **then**
                dist[v] := dist[u] + $E(u,v)$
                previous[v] := u
            **Comment:** Compare width differences, if 2 child nodes (at bifurcation) possess equal orientation differences with parent node
            **for** each neighbor v' ($\neq$ v) of u: **do**
                **if** abs[$E(u,v)$-$E(u,v')$] $<$ 0.35 radian **then**
                    **if** $E(u,v) \leq E(u,v')$ **then**
                        m=$E(u,v)/E_W(u,v)$
                    **else**
                        m=$E(u,v')/E_W(u,v')$
                    **Comment:** Scale matching of width difference cost to orientation difference cost
                    Initialize $E(u,v)$=$E_W(u,v)$ * m and $E(u,v')$=$E_W(u,v')$ * m
                    dist[v] := dist[u] + $E(u,v)$
                    dist[v'] := dist[u] + $E(u,v')$
                    **Comment:** Compare intensity differences, if 2 child nodes (at bifurcation) possess equal width differences with parent node
                    **if** abs[$E(u,v)$-$E(u,v')$] $<$ 0.35 radian **then**
                        **if** $E(u,v) \leq E(u,v')$ **then**
                            n=$E(u,v)/E_I(u,v)$
                        **else**
                            n=$E(u,v')/E_I(u,v')$
                        **Comment:** Scale matching of intensity difference cost to orientation difference cost
                        Initialize $E(u,v)$=$E_I(u,v)$ * n and $E(u,v')$=$E_I(u,v')$ * n
                        dist[v] := dist[u] + $E(u,v)$
                        dist[v'] := dist[u] + $E(u,v')$

    **Comment:** Nodes on the path from end point node $i$ to $s$ = previous[], path cost = dist[i]; for i
    **Comment:** Path cost normalized by number of nodes on path, $dist_{norm}$[i] = dist[i]/length(previous[]); for i
    return $dist_{norm}$[i], previous[]; for i

**Comment:** True vessel path = path from $e'$ to $s$ which has minimum of all $dist_{norm}$[e]
$dist_{norm}$[e'] = min($dist_{norm}$[e])
True vessel path = previous[]; for $e'$

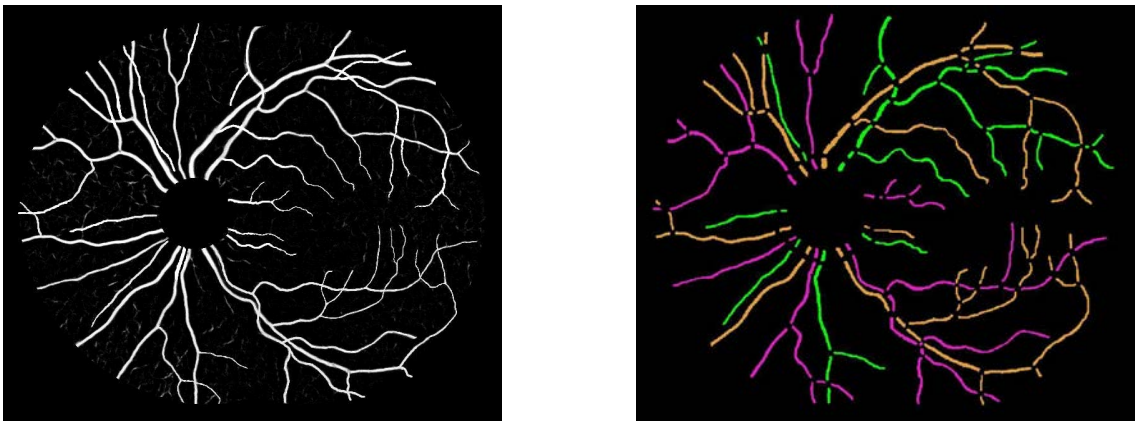

Figure 3.13: Structural mapping: a) Vessel probability map b) Structural mapping of vessel network

image, signifies high probability of one vessel being an artery and the other one being a vein. In other words, at a vessel crossing, there is very low probability of both vessels being of the same kind; i.e., both being arteries or both being veins. Therefore, as an initial task, the vessel trees are separated into those with (Fig. 3.14(b)), and those without (Fig. 3.14(c)) artery-venous crossing.

The vessel segments (Fig. 3.14(a)) are skeletonized to obtain the vessel centerlines. For the centerline extraction, significantly large vessel width segments in a vessel tree are selected to avoid the inclusion of smaller, peripheral or single pixel width segments. It may prevent the effect of noisy centerlines on color feature extraction. A significantly large vessel width is defined for a particular vessel tree locally, and is determined as the width more than 60% of the maximum vessel width obtained in that vessel tree.

A feature vector consisting of four features, viz., mean ($MG$) and standard

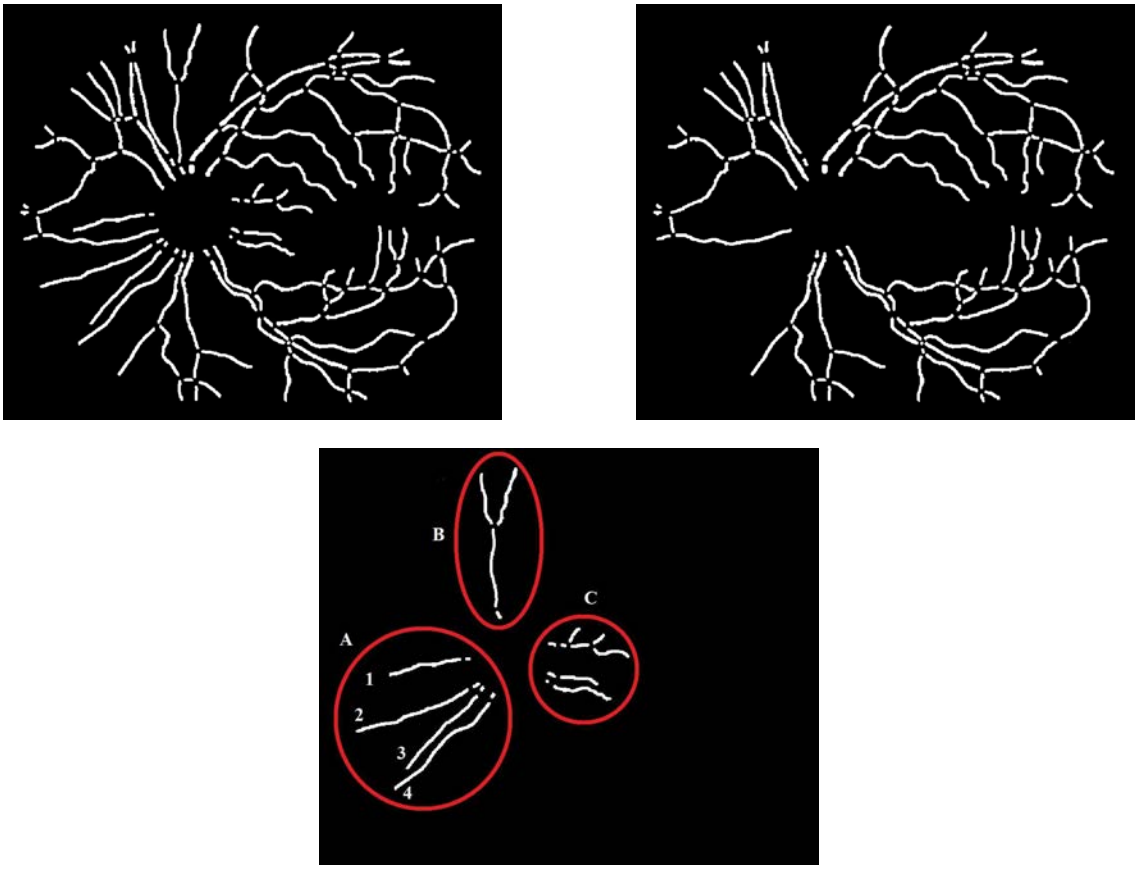


Figure 3.14: Vessel network: a) Vessel segment map b) Vessel trees with artery-venous crossing c) Vessel trees without artery-venous crossing

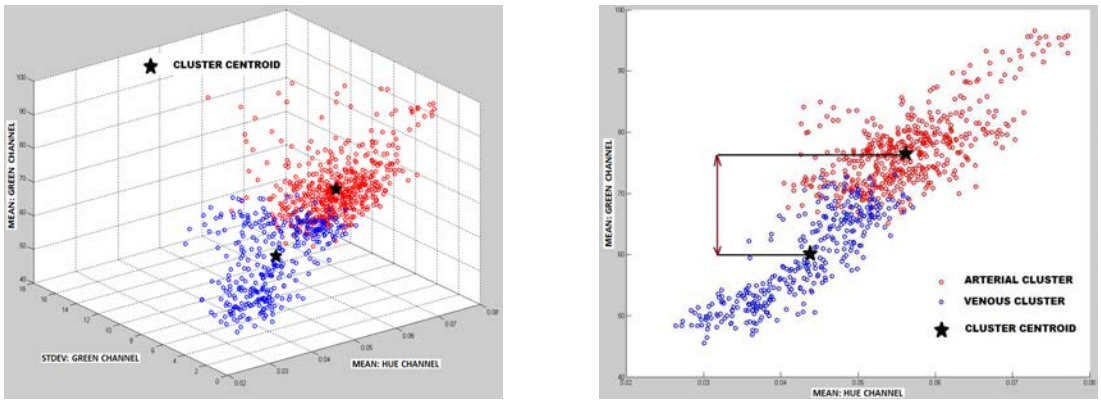


Figure 3.15: Clustering: a) Cluster formation b) Comparison of mean green channel intensity

deviation ($SG$) of green channel (from RGB color space) (Fig. 3.8(b)), and mean ($MH$) and standard deviation ($SH$) of hue channel (from HSV color space) (Fig. 3.8(c)), from the 3x3 neighborhood (region of interest) of each vessel centerline pixel is acquired. The choice of particular color features has been shown to be capable of distinguishing between arteries and veins [114][122]. Arteries appear brighter (higher green channel intensity: $MG$) than veins because oxygenated hemoglobin is less absorbent than the de-oxygenated blood between 600-800 nm [128].

#### 3.3.2.7 Artery-Venous classification of retinal vessels based on fuzzy C-means clustering

The centerline pixels obtained from any two vessel trees are collected and classified to detect the AV status of respective vessel trees. Based on the associated feature vector, the algorithm classifies the centerline pixels obtained from a pair of vessel trees, into two clusters/classes (with respective centroids) using the fuzzy

C-means clustering algorithm (See Appendix). Each centerline pixel is assigned a degree of belonging to each of the two clusters (a number between 0-1), based on Euclidean distance measurement between the cluster centroid and the pixel in feature space. The two degrees assigned to a centerline pixel always sum to 1. A centerline pixel with difference between two degrees, higher than 0.2 (e.g., 0.39 vs. 0.61), is assigned to the higher degree cluster. The use of fuzzy C-means clustering helps eliminating the centerline pixels with difference between two degrees of less than 0.2, i.e., having more or less equal affinity (e.g., 0.45 vs. 0.55) towards both clusters. These indeterminate pixels are treated as noise pixels and are removed from further analysis. Fig. 3.15(a) shows the formation of two clusters in a three-dimensional view with axes represented by $MG$, $SG$, and $MH$, and centroids marked with a black star ($\star$) symbol. The centroid of each of the two clusters is a co-ordinated vector of average values of 4 feature properties associated with centerline pixels in that cluster [$MG_{mean}$,$SG_{mean}$,$MH_{mean}$,$SH_{mean}$]. The clusters are labeled as arterial or venous, based on the numerical comparison of averages of mean green channel intensity ($MG_{mean}$) of two centroids. Fig. 3.15(b) shows the projection of clusters in (Fig. 3.15(a)) on a two-dimensional plane formed by $MG$ and $MH$, with $MG$ represented on Y-axis. The cluster with higher average value of mean green channel intensity ($MG_{mean}$) is labeled as arterial cluster and the other cluster as the venous cluster, since arteries appear brighter relative to veins.

For a pair of vessel trees with AV crossing (with prior knowledge of them being of different types), the vessel tree with higher proportion of arterial class centerline

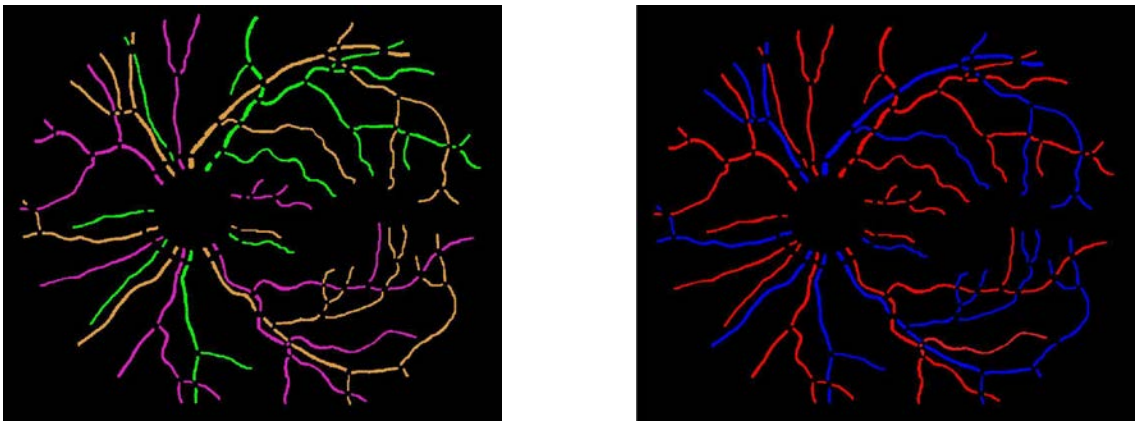

Figure 3.16: AV classification: a) Structural mapping b) Artery-Venous Classification

pixels compared to the other vessel tree is labeled as an arterial tree, and the other one is labeled as a venous tree. For the vessel trees with no AV crossing, I use the following method for classification. A group of single vessel trees in a localized region are analyzed together which may prevent the non-uniform illumination effects, as shown in (Fig. 3.14(c)) for groups A, B, and C. The vessel trees in any one group at a time, are organized in pairs such that the mutual comparison is possible, e.g., Vessels 1,2,3 and 4 in group A are compared in pairs such as 1-2,1-3,1-4,2-3,2-4 and 3-4. If a group consists of only one single vessel (e.g., group B), this vessel is merged into spatially nearest group of vessels (e.g., group C) for analysis. For each pair of vessels, the most probable class of centerline pixels is identified for each vessel; i.e., the class pixels (arterial or venous) occupying in higher proportion of centerline pixels on that vessel. As the statuses of both the clusters/classes are already determined, each vessel in a pair is soft-labeled with the corresponding high probability class label. This procedure is followed for all the vessel pairs in a group and each vessel

in a group is soft-labeled number of times depending upon the number of vessels in that group. A hard label is assigned to each vessel as the median value of all the soft labels received for that vessel. The vessels without AV crossing are classified based on the most probable class of centerline pixels but with mutual comparison between vessel pairs and a voting procedure (i.e., median of soft labels). The AV classification results are shown in (Fig. 3.16(b)), with arteries marked in red and veins marked in blue.

### 3.3.3 Materials

I evaluated the dataset of 50 digital color fundus images of 50 subjects selected randomly from EYECHECK database. More information about the dataset can be found elsewhere [8]. The dataset consists of standard two-field registered fundus images (768x512, 45° FOV) with normal subjects and subjects with some form of diabetic retinopathy. The images were deidentified and patient's personal information was encapsulated from the research team. The proposed method was applied to the dataset and the images used to design and implement the algorithm were excluded from the evaluation data. The fundus images were processed to obtain the vessel segmentation and the vessel segment map as shown in (Fig. 3.14(a)). In order to validate the structural mapping and the AV classification produced by the automated method, the vessel segment map (Fig. 3.14(a)) was annotated manually by a trained human grader using color labels for structural mapping, whereas red (artery) and blue (veins) labels for AV classification. I used previously validated Java based Truthseeker desktop application for expert annotation of vessel trees [129].

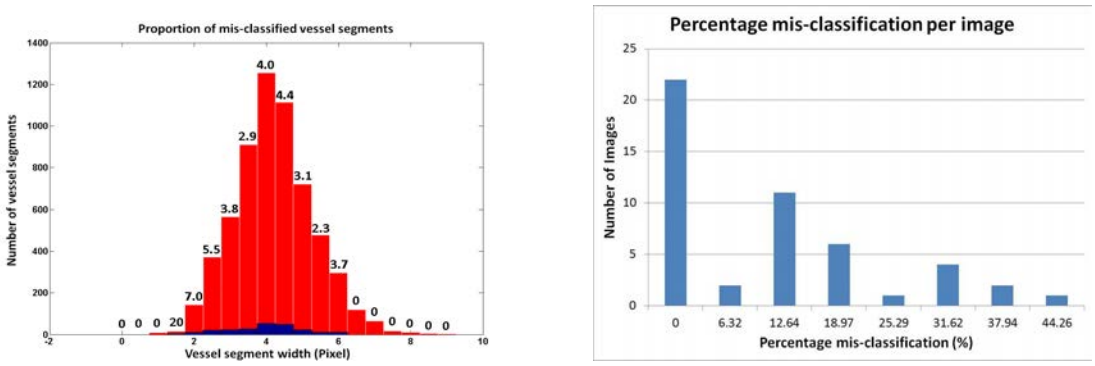


Figure 3.17: Quantitative results: a) Proportion of mis-classified vessel segments, b) Percentage mis-classification per image

### 3.3.4 Results

A copy of the vessel segment map (as above) was also labeled using the automated method by preserving the respective color code followed by the grader. To evaluate the accuracy of the proposed method, the automated labeling was compared with the expert annotation in terms of a segment color value. A segment marked with equal color value by both automated method and expert annotation was treated as accurately classified segment, and vice versa.

Two metrics were utilized to quantify the accuracy of the method. The first metric calculates the mis-classification rate (%) for vessel segments as a function of vessel segment width, over the dataset (Fig. 3.17(a)). The red bar in the histogram shows the total number of vessel segments (Y-axis) within a particular width interval (X-axis), whereas the respective blue bar shows the number of mis-classified vessel segments in the same interval. The number shown on top of each red bar represents the mis-classification rate (%) for vessel segments within that width interval. The mis-

| Vessel size | Vessel width (Pixel) | Vessel segment mis-classification (%) |
|---|---|---|
| Small/Peripheral | 1≤width<4 | 4.07 |
| Medium | 4≤width≤6 | 3.78 |
| Major | 6<width≤9 | 0.00 |

Table 3.1: Proportion of mis-classified vessel segments

classification rates (%) for various vessel segment sizes were categorized in Tab.3.1. The average mis-classification rate (%) for vessels with width above 4 pixels was 3.58%. Thus, given a randomly selected medium sized or major retinal vessel, it would be classified correctly in 96.42% of cases.

The second metric (Fig. 3.17(b)) shows the histogram of pixel mis-classification (%) per image, in the dataset. The Y-axis shows the number of images for which the pixel mis-classification (%) was within the interval represented on (X-axis). For each image, the pixel mis-classification (%) was calculated as the fraction of total number of vessel pixels which was mis-classified, representing its impact on the vessel network. The average mis-classification of 8.56% or the accuracy of 91.44% correctly classified vessel pixels was obtained over the dataset.

The average mis-classification rate (%) for single vessel trees (without AV crossing) was obtained as 17.07%, whereas the average mis-classification rate (%) for paired vessel trees (with AV crossing) was determined as 4.96%. The difference between the mis-classification rates for single and paired vessel trees was statistically significant (p-value<0.05).

The average running time per image starting at the readily available vessel

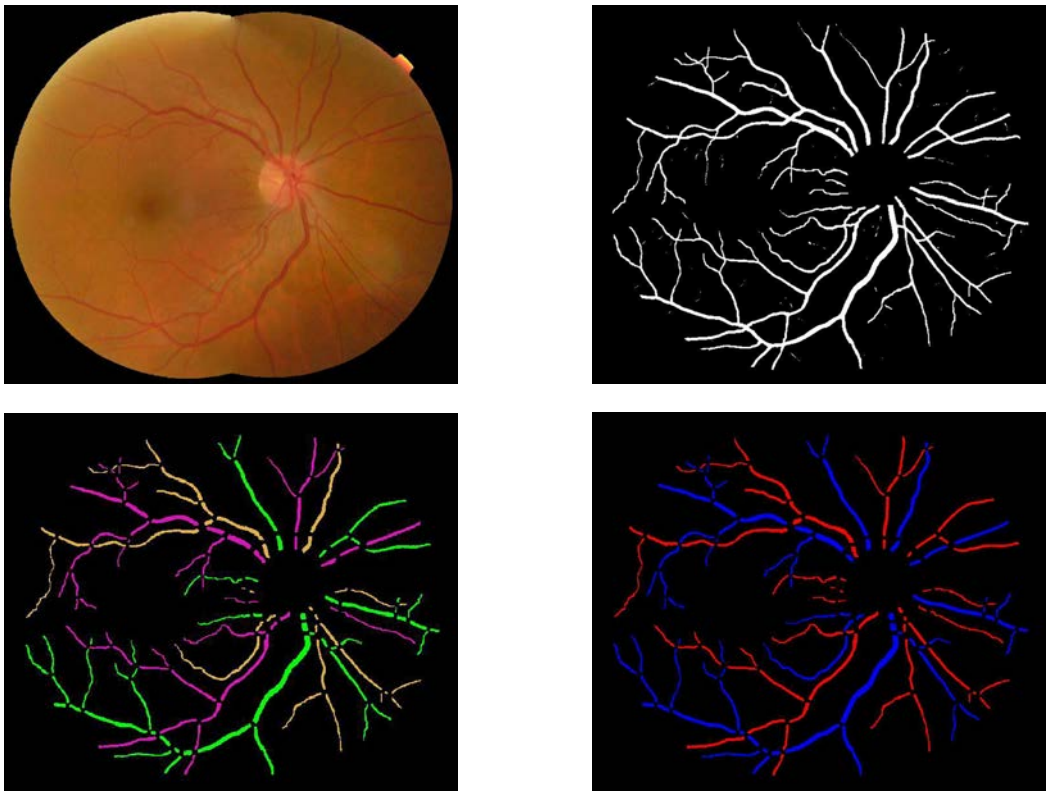

Figure 3.18: Results: a) Fundus image b) Vessel probability map c) Structural mapping d) AV Classification

segmentation to AV classification was 8 minutes including 7 minutes for structural mapping and 1 minute for subsequent AV classification, when processed in MatLab environment on a standard personal computer with Intel core 2 Duo processor, running at 3 GHz. The algorithm was not optimized for speed. The automated structural mapping and AV classification of retinal vessel trees has been demonstrated in Fig. 3.18.

### 3.3.5 Discussion

I developed an automated method for identifying and separating the retinal vessel trees in color fundus images, which provides the mapping of primary vessels, and their branches. The strategy of modeling the vessel segmentation into vessel segments, characterizing their properties, i.e., orientation, width and intensity, and minimizing the difference between these properties to identify a true vessel, may work well for structural mapping. Furthermore, I described the mapped vessel trees in terms of arteries and veins.

The results demonstrate that the automated method is capable of separating and classifying the retinal vessel trees with the accuracy comparable to that of expert annotation performance. The first metric reports the average mis-classification rate below 5% for vessel segments. This mis-classification rate decreases further to 3.58% if only medium sized and major vessels are considered, as a clinician may find their diagnostic importance higher compared to smaller or peripheral vessels. Therefore, the diagnostically relavent vessels may be classified correctly 96.42% of the times. The second metric provides the average accuracy of 91.44% correctly classified vessel

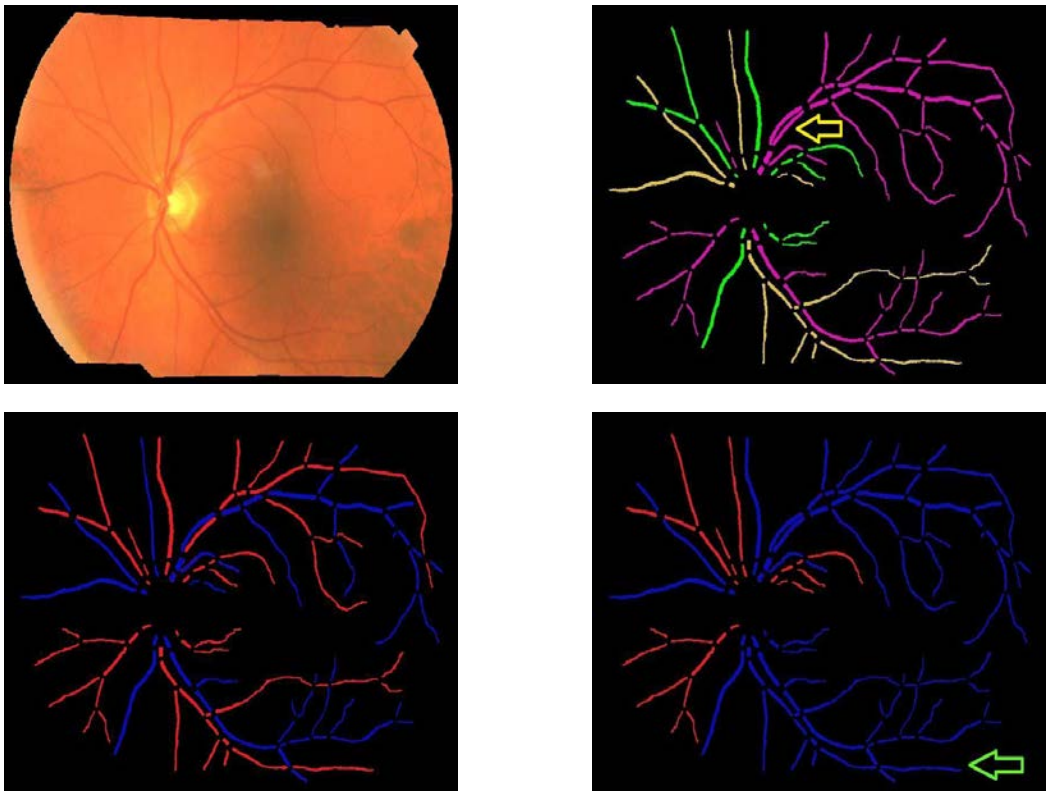

Figure 3.19: Results: a) Fundus image b) Structural mapping c) Manual AV labeling d) Automated AV Classification

pixels (vessel network area), and enables the determination of the overall impact of mis-classification on the vessel network. The results (Fig. 3.17(b)) show six outliers representing images with more than one-third of the vessel region classified falsely. The image with highest mis-classification of 44.26% is shown in (Fig. 3.19), which was partially contributed by both false structural mapping and false AV classification, as will be discussed later. On an average, the proposed method may be capable of classifying at least 90% of the vessel network accurately.

The structurally separated vessel trees were classified using color properties that distinguish between an artery and a vein. The classification based on localized color features along with mutual comparisons and a voting procedure may have reduced the effect of intensity variations across the image, and across different subjects. The artery-venous crossing property determined the vessel pairs with a high probability of vessels being of different types, and enhanced the classification performance. It is evident from the smaller contribution of paired vessel trees (4.96%) in mis-classification relative to that of single vessels (17.07%), and statistically significant difference between the mis-classification rates for both vessel types.

The AV classification methods [114][122] reported previously, depend upon the color features obtained from vessels to discern between an artery and a vein. For the feature extraction, the vessel segments are selected from a definite region of interest (ROI), which may exclude the posterior pole as well as the peripheral region of retina. This region selection constraint may limit the strength of a feature set as the features are extracted only from the selected ROI. Furthermore, since these methods classify the vessels only inside the ROI, it may become complicated to propagate the classification results outside the ROI. This may constrain the measurement of AV parameters such as AVR to a limited region. However, the proposed method provides structural mapping of the entire vessel network which may enable the AV feature extraction without the region constraint and AV classification over the complete vessel network.

The proposed method provides the separation of vessel trees into arteries and

veins as well as into primary vessels, and their branches, which may reduce the inter-twining complexity of the retinal vessel structure that normally prevents the accurate measurement of individual vessel properties. This analysis may enable the automated measurement of morphologic parameters viz., branching angle and branching coefficient which get altered during retinopathies such as diabetic retinopathy [10][9]. The added advantage may be the inclusion of smaller and peripheral vessels into the measurement system without following the constraint over the vessel size as in [88], or the specified ROI of the fundus as in [104].

The method reported by Aylward et al. estimates the mapping of intra-cranial vessels imaged in three dimensions, in terms of spatial graphs [119]. However, the proposed method utilizes the structural properties of retinal vessels imaged in two dimensions, which may recover for the loss of third dimensional data, for simplifying the mapping procedure. Few other methods developed for retinal vessel tracking in two dimensions [56][55], may track the vessel without a control over its individual structural propagation. Therefore, they may not provide the identification and the separation of individual vessel trees. To the best of knowledge, the proposed method may be a novel research describing the structural mapping and AV classification of retinal vessel trees imaged in two-dimensional color fundus images.

Though a novel approach towards the retinal vessel analysis, some limitations of this method are worth mentioning. The method requires clean and connected vessel segmentation image for the structural mapping. Therefore, poor and interrupted vessel segmentation may result into inconsistent and false mapping. I previously

developed a method for identifying and reconnecting the interrupted vessels using graph search which may be able to provide a connected vessel structure [57]. The other limitation is its inability to identify and separate two vessels overlapping or touching each other in a parallel course (Fig. 3.19(b):Yellow arrow), which may be improved using methods presented elsewhere [130]. The AV classification method is based on color features of vessels and therefore limited by the non-uniform illumination effects and low contrast in the fundus image. It may result into a false classification of arteries and veins due to the localized illumination effect. Fig. 3.19(c) shows the AV classification by a trained grader, and Fig. 3.19(d) shows the automated AV classification where artery in a local darker region is classified as a vein (Green arrow).

In summary, I developed the automated method for identification and AV classification of retinal vessel trees in fundus color images. The properties of a vessel structure, i.e., orientation, width and intensity, were utilized to identify the vessel tree, and its color as well as crossing properties classified it as an arterial or a venous vessel tree. The proposed method was validated on a fundus color image dataset showing results that match well with the expert annotations. The preliminary version of this method was published in [131][132].

### 3.3.6 Conclusion

The research presents a novel method for identification and AV classification of retinal vessel trees in color fundus images. A fundus image and the corresponding vessel segmentation image are processed to obtain the separation of intertwined vessel trees, and their description in terms of arteries and veins. The structural mapping and

the AV classification results match well with the expert annotations. This approach has the potential to have major impact on the diagnostically important morphologic analysis of individual retinal vessels.

## 3.4 Automated measurement of retinal blood vessel tortuosity

### 3.4.1 Introduction

Morphologic analysis of retinal vessels was proven to be of primary importance in gaining an understanding about future complications, either in the eye or in other parts of the body. The methods proposed in the previous step [59] enable the measurement of morphologic parameters with respect to arteries and veins, as well as the different branching generations.

The vessel tortuosity is of high clinical significance and may be measured using the method proposed below. Fluctuations in physiological parameters such as blood volume, blood flow, or blood pressure, due to the above mentioned disorders, change the structural properties of the retinal blood vessel network, such as geometry and the shape of blood vessels (blood vessel morphology), contributing to vessel tortuosity (Fig. 3.20). In eye and systemic diseases the arteries, veins, or both change their shape in terms of curvature and twists, the changes which are collectively described by clinicians as tortuosity [133][30][72][83].

Ophthalmologists analyze vessel tortuosity visually, using qualitative assessments of curvature and changes in the vessel course or direction, such as winding and twisting. Visual assessment and qualitative grading of vessel tortuosity suffers

Figure 3.20: Fundus image: a) normal and, b) with tortuous blood vessels

from inter-observer and intra-observer variations [133]. Thus a quantitative index of vessel tortuosity may provide a more sensitive and reproducible measure of vessel characteristics. Some methods describing the vessel tortuosity are based solely on the measurement of vessel arc to chord ratio or the vessel curvature analysis which may not conform to the clinically acceptable tortuosity characteristics [84] [134]. A review of such methods has also been presented in the literature [87].

Grisan et al. proposed a method to measure retinal blood vessel tortuosity in mathematical terms [87], and I will compare their approach to the new method.

I propose an automated method to assess vessel tortuosity using geometric properties of the vessel structure as extracted from digital fundus images of the retina. The vascular structure can be extracted using the previously developed methods [135][136][49][51]. I calculate a tortuosity index (TI) which presents a numerical assessment of vessel tortuosity, and test the method using the available dataset [137].

### 3.4.2 Method

#### 3.4.2.1 Description of Tortuosity

In order to propose a method to estimate the numerical index describing vessel tortuosity, one needs to understand the notion of tortuosity and the parameters which affect its measurement. Ophthalmologists visually judge blood vessel tortuosity based on an assessment of total curvature and/or local curvature and changes in the vessel course or direction. A metric that provides a numerical index for tortuosity measurement, needs to determine the parameters affecting the tortuosity, according to the opthalmologic conventions and should conform to the clinical definition of vessel tortuosity.

In the proposed metric, tortuosity is assessed by measuring the curvature of a vessel, length of a curved vessel over chord length, and the number of curvature sign changes along the vessel course, which conform to the clinically accepted properties for describing the vessel tortuosity. I define a tortuosity index (TI) combining the above mentioned properties to differentiate between normal or abnormal blood vessels.

#### 3.4.2.2 Algorithm overview

The proposed method can be summarized as consisting of three tasks.

1) Vessel segmentation.

2) Assessment of the geometric features of a vessel, affecting the TI.

3) Calculation of final TI.

The retinal blood vessel segmentation is obtained from the color fundus image

(Fig. 3.21(a)) using a previously published method developed by our group [33]. It is a supervised method based on pixel classification that uses a Gaussian filter set for feature extraction. Each pixel in the fundus image is classified with a k-Nearest Neighbor classifier to produce vessel segmentation in terms of a gray level vessel probability map (Fig. 3.21(b)). The blood vessels which have been used in the implementation of the proposed method were extracted manually from the vessel probability map (Fig. 3.21(c)). For each subject, the blood vessels were preprocessed to determine the centerlines by skeletonization [117]. The vessel centerline was used for further analysis.

In order to quantify the tortuosity of the entire blood vessel, algorithm sums up the local tortuosity measures of its individual segments. For this purpose, the centerline data corresponding to the entire vessel course is decomposed into consecutive individual segments, marking the centerline at regular intervals. For each vessel segment, the method determines the following parameters (discussed in detail in the next section) in order to estimate the local tortuosity.

1) Arc to Chord Ratio

2) Number of changes in Curvature sign/Frequency

3) Angle of Curvature

The algorithm sums up the local tortuosity measures from all segments to determine the tortuosity index, as compared to the methods which estimate the vessel tortuosity on global measures. A brief review of such methods is presented in the literature [87].

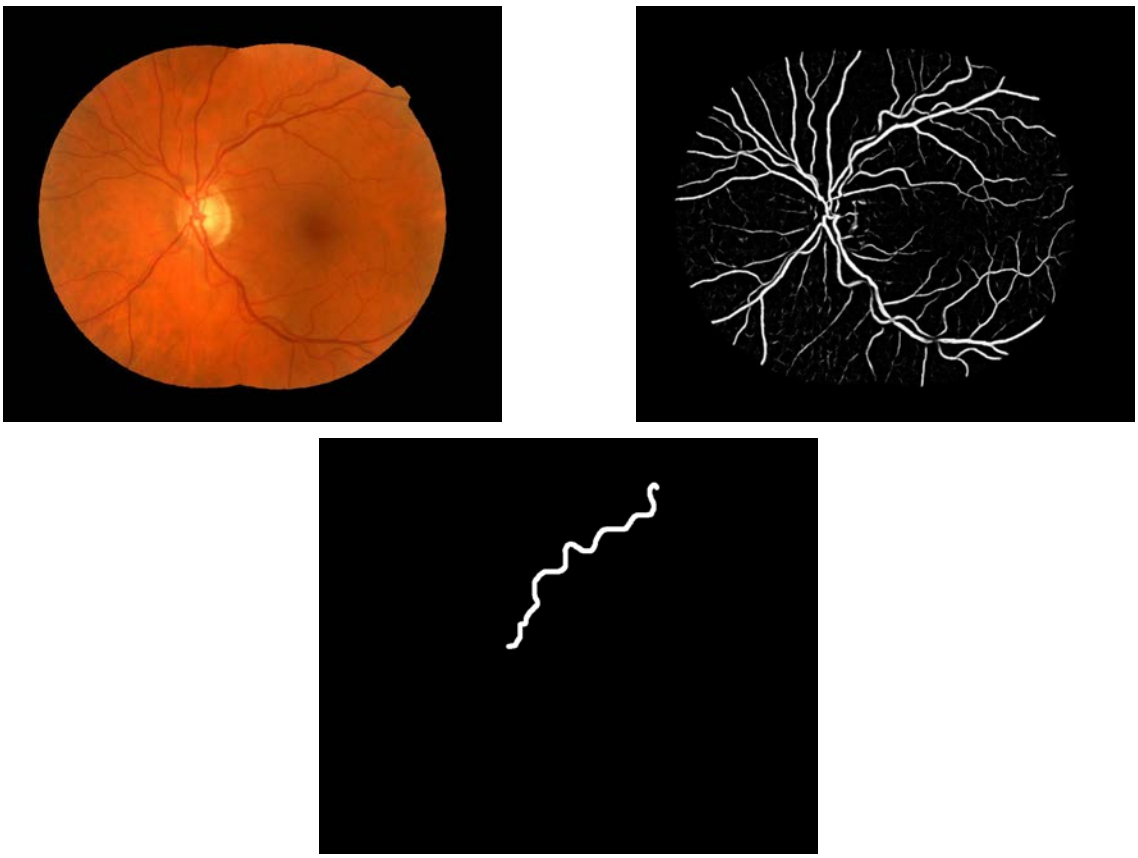

Figure 3.21: Preprocessing: a) Fundus Image b) Vessel probability map c) Segmented vessel

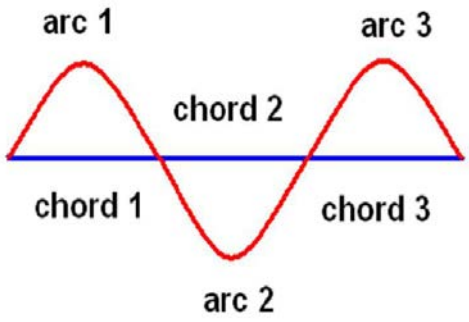


Figure 3.22: Ratio of vessel arc to vessel chord for 3 individual segments in the vessel

3.4.2.3 Assessment of the geometric features

1) The arc to chord ratio is determined as follows. Considering the ophthalmologist's description of tortuosity, the first parameter I include in the metric is based on the distance measures. It is defined as the ratio of length of a vessel arc to length of the corresponding vessel chord (Fig. 3.22) [138][139][134][140]. In other words, the given parameter measures the normalization factor for the curved length of the vessel segment per unit shortest (straight-line) distance between the two ends of the vessel segment.

2) The number of changes in the curvature sign is determined as follows. Using only the distance based metric explained above, may not be sufficient in providing the ophthalmologist's perception of tortuosity, as this metric alone is unable to differentiate between the tortuosities of blood vessels with equal arc to chord ratios but different number of vessel twists or turns, i.e., frequency [87] .

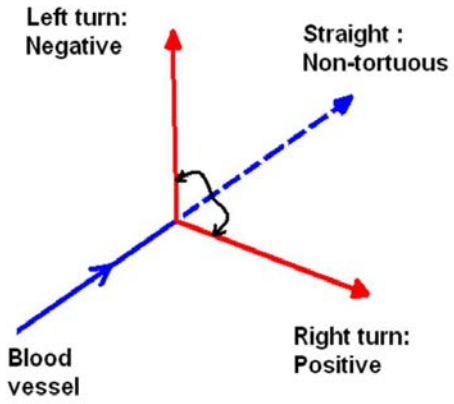


Figure 3.23: Frequency or number of curvature sign changes

Retinal disorders affect the vessel course by producing twists and windings. Retinopathy of prematurity is one of the disorders which affects the vessel course with twists, near to the posterior pole of retina [141] [83][142]. A method which is based on calculating the number of inflection points (change in curvature sign) in the vessel course, estimates the tortuosity inclusive of frequency parameter [143]. The limitation of this method is the lack of normalization procedure which may differentiates between vessels of different lengths.

The proposed method includes a parameter which determines the number of changes in the sign of a curvature of a vessel, or the number of sign changes when a vessel turns to change its course, through its length. Figure (Fig. 3.23) shows the sign convention for the left turn as negative and the one for the right turn as positive. This parameter determines the total number of events when the vessel changes its direction of course from negative to positive and vice versa. Sometimes the poor vessel segmentation or the image processing noise, affects the data containing the

centerline of the vessel, which may result into detecting an undesired curvature sign change even with very small angles of curvature (clinically insignificant), in a local tortuosity calculation. This introduces more than the true number of sign changes in the determination of tortuosity, which does not conform to the ophthalmologist's notion of frequency in tortuous vessels. To avoid this, the algorithm works with a hysteresis criterion in which all the angle of curvature measures ($\theta$) below the pre-defined threshold value of $\theta = 20^\circ$ (empirically determined), are treated as due to a noise and discarded, and the angle of curvature measures above the threshold are accounted for the calculation of curvature sign changes.

3) The angle of curvature is determined as follows. To maintain the count of how many times the vessel changes its course is required but may not always be sufficient. The measure of angle through which the vessel segment changes the course is also an important aspect. The third factor I estimate is based on the measure of curvature of the vessel segment. This factor stands to be valuable and I am going to show in discussion section, how it helps overcoming the limitations presented in the literature method [87].

It determines the magnitude or the measure of angle of curvature through which the vessel segment changes its course. More the angle through which the vessel turns, more is the tortuosity of the vessel. Figure (Fig. 3.24) shows the increasing tortuosity measures of the vessel turning through larger angles.

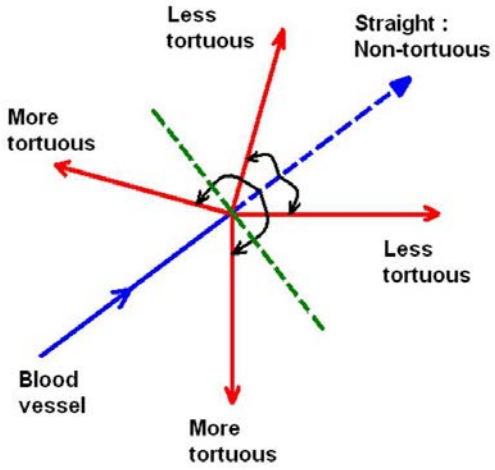


Figure 3.24: Angle of curvature

4) The final task accomplished by the algorithm is the determination of the tortuosity index. The aforementioned factors affecting the tortuosity of a vessel are normalized and are formulated to derive the tortuosity index (TI), given as,

$$TI = \frac{(n+1) * (\sum_{i=1}^{m} \Theta_i) * (\sum_{i=1}^{m} (L_{ci}/L_{xi}))}{L_c * m * m} \tag{3.4}$$

where, TI is a tortuosity Index, n is the number of changes in curvature sign, m is the number of segments in the vessel, $\Theta_i$ is the magnitude of angle of curvature, Lci is the length of the respective arc, Lxi is the length of the respective chord, and Lc is the total length of the vessel. The parameters with subscript i describe the values for ith segment. Factor 'n' (Frequency) has been normalized over the total length of the vessel (Lc), so that it gives equal tortuosity perceptions for two vessels with equal frequencies per unit length but different lengths over the course. Factor

'Θ' (Angle of curvature) calculated for each segment is summed up over all segments and is normalized with the number of individual segments in the vessel (m), so that it gives equal tortuosity perceptions for two vessels with approximately equal curvatures but different lengths over the course. Factor $L_{ci}/L_{xi}$ (Arc to chord ratio) calculated for each segment is summed up over all segments and is normalized with the number of individual segments in the vessel (m), so that it gives equal tortuosity perceptions for two vessels with approximately equal 'arc to chord ratio' but different lengths over the course. The given metric (Eqn.3.4) shows the formulation in which the numerator enlists the three parameters and denominator enlists the normalization factors for the corresponding parameters.

### 3.4.3 Results

The proposed algorithm was applied to a case study consisting of 15 fundus images (Image size: 3150x2696) of 8 patients with facioscapulohumeral muscular dystrophy (FSHD), a congenital disease that was recently described by us to display retinal arterial tortuosity related to severity [137]. Fundus photographs were obtained with the Zeiss fundus camera with the pupil in a dilated position. Three masked ophthalmologists graded the vessel tortuosities based on a Likert severity scale from 1 to 4 with 1 indicating lowest and 4 indicating highest tortuosity (ground truth). To compare the TI with the ground truth, the following tables summarize the correlation between the TI values obtained by the method and the grading obtained by the experts for arteries (Tab.3.2) and veins (Tab.3.3). Second column represents the numerical average of severity grading given by 3 ophthalmologists, combined for both

| Patient ID | Average grading by 3 experts | TI by method | TI ranking |
|---|---|---|---|
| C | 1.00 | 4.82 | 1 |
| H | 1.33 | 32.41 | 2 |
| B | 2.00 | 33.52 | 3 |
| G | 2.00 | 35.78 | 4 |
| F | 2.66 | 46.64 | 5 |
| E | 3.33 | 63.86 | 6 |
| D | 4.00 | 65.00 | 7 |
| A | 4.00 | 141.82 | 8 |

Table 3.2: Correlation between the TI and the manual grading, for arteries

| Patient ID | Average grading by 3 experts | TI by method | TI ranking |
|---|---|---|---|
| B | 1.00 | 3.47 | 1 |
| F | 1.00 | 3.51 | 2 |
| E | 1.00 | 4.07 | 3 |
| C | 1.33 | 5.10 | 4 |
| G | 1.00 | 8.55 | 5 |
| D | 1.33 | 10.72 | 6 |
| A | 1.33 | 11.78 | 7 |
| H | 1.33 | 20.58 | 8 |

Table 3.3: Correlation between the TI and the manual grading, for veins

eyes and the fourth column represents the tortuosity (TI) rankings from 1 to 8 with 1 indicating lowest tortuosity and 8 indicating highest tortuosity. This correlation has been emphasized graphically for arteries (Fig. 3.25) and for veins (Fig. 3.26).

The Spearman's ranking correlation coefficient between the tortuosity index (TI) by method and manual tortuosity grading was calculated for arteries as $r_s$=0.98, and for veins as $r_s$=0.77. The average running time per vessel, starting with manually extracted vessel segment from the readily available vessel segmentation to the tortuosity index determination was 10 seconds, when processed in MatLab environment

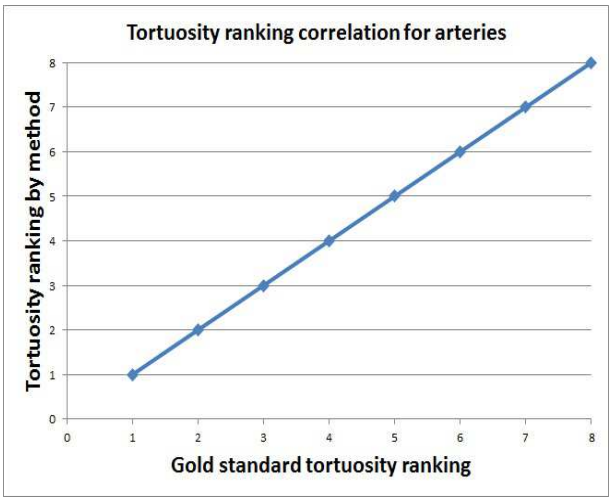


Figure 3.25: Correlation between the results obtained by the method and that by manual grading, for arteries, FSHD dataset. Circles represent the tortuosity ranking by the method for the corresponding ranking by the experts and the 45 line represents the ideal correlation between the two rankings

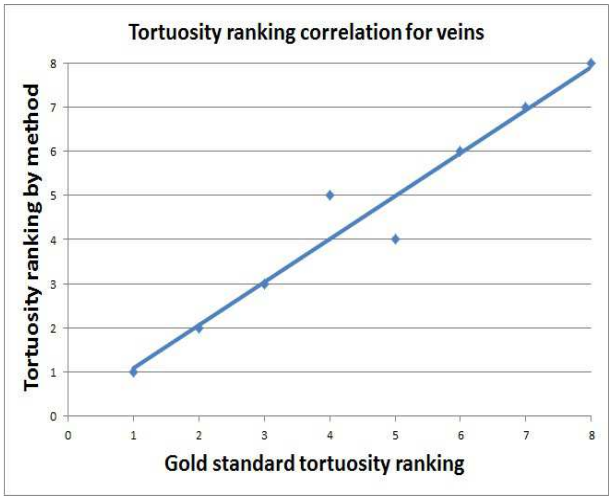


Figure 3.26: Correlation between the results obtained by the method and that by manual grading, for veins, FSHD dataset. Circles represent the tortuosity ranking by the method for the corresponding ranking by the experts and the 45 line represents the ideal correlation between the two rankings. The maximum disagreement of 1 rank at the outlier (4,5)

on a standard personal computer with Intel core 2 Duo processor, running at 3 GHz.

With reference to tables (Tab.3.2) and (Tab.3.3), it is observed that the patients can be conveniently graded for tortuosity based on the numerical indices (third column) rather than merely distinguishable manual grading patterns (second column). The tortuosity index (TI) obtained by the proposed method and the qualitative grading of tortuosity by the ophthalmologist's evaluation are highly correlated.

### 3.4.4 Discussion

A method presented in the literature [87], proposes an algorithm to determine a tortuosity index for retinal blood vessels. It gives the tortuosity index as:

$$TI = \frac{(n^{'} - 1) * (\sum_{i=1}^{n^{'}} (L_{ci}/L_{xi}) - 1)}{n^{'} * L_c} \tag{3.5}$$

The metric proposed here has the same legend for variables as used in (Eqn.3.4), except for $n^{'}$ which is the number of turn curves. Analyzing this metric, I may address some of its limitations, and propose the solutions.

For a vessel with constant curvature sign, or with no twists or turns throughout its course, the algorithm (Eqn.3.5) produces the number of turn curves as $n^{'}$=1, which yields the TI=0, meaning the method provides equal TI (TI=0) values for all the vessels with constant curvature sign or no turns. Hence, it provides equal tortuosity estimates for all the vessel structures presented in (Fig. 3.27(a)) from a straight line to a high curvature vessel. The index TI=0 may fit well for the vessels having a course close to the straight line (small curvature), but may not be appropriate for the

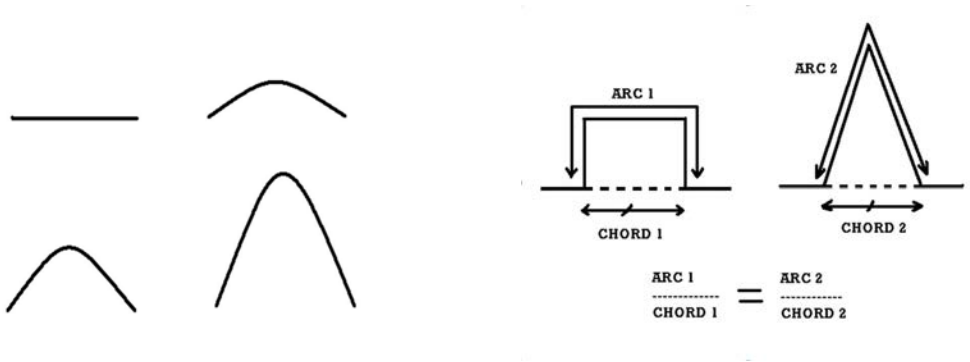


Figure 3.27: Retinal vessels: a) Vessels with constant curvature sign (no turns) from straight line to high curvature vascular pattern, b) Theoretical vessels with equal $n^{'}$ and equal arc to chord ratios, e.g. (arc1=arc2, chord1=chord2)

vessels with higher curvature. TI value of 'zero' does not suit the clinical perception of tortuosity of high curvature vessels. This high curvature value may be of a significant clinical importance as a retinopathy sign, especially when calculating the tortuosity of the entire vessel network.

By the proposed algorithm (Eqn.3.4), the number of curvature sign changes n=0, which formulates TI=1*Angle of curvature*Arc to chord ratio, and produces appropriate tortuosity estimates for all the constant curvature sign vessels, with higher TI value corresponding to higher curvature vessels and vice versa. For vessels with n=0, the tortuosity is determined by the product of angle of curvature and arc to chord ratio.

For the vessels with equal frequency and arc to chord ratio, the TI is determined by two metrices differently. The metric presented in (Eqn.3.5), is based on two parameters, i.e., Frequency and Arc to chord ratio. Hence, it provides equal

tortuosity index values for vessels with equal frequencies ($n^{'}$) and equal Arc to chord ratios. (Fig. 3.27(b)) shows two theoretical vessels which may have equal frequencies and equal arc to chord ratios, and hence equal TI according to the metric (Eqn.3.5), but different clinical tortuosity perceptions in the ophthalmologist's evaluation.

The proposed metric (Eqn.3.4) has one more parameter based on the angle of curvature of a vessel. For the vessels shown in (Fig. 3.27(b)), the metric produces appropriate tortuosity values corresponding to their $\Theta$ or the angle of curvature such that, TI=k*Angle of curvature, where k = constant determined by equal frequency and equal arc to chord ratios.

The proposed method estimates the parameters such as angle of curvature and number of curvature sign changes, which overcomes the shortcomings introduced in the vessel tortuosity determination when considering solely the arc to chord ratio, or the curvature [84][134].

### 3.4.5 Conclusion

The method presents a quantitative index of tortuosity by analyzing the factors affecting the local tortuosity values of a retinal blood vessel, and formulates them to provide a tortuosity index (TI). The TI may offer an automated tool giving the user an objective and reproducible measure of vessel tortuosity which may overcome the challenges experienced in the qualitative assessment of vessel tortuosities. The high correlation with expert's subjective estimates shows that the proposed algorithm has potential in the automated tortuosity evaluation.

## 3.5 Automated detection of malarial retinopathy associated retinal hemorrhages

### 3.5.1 Introduction

Malarial retinopathy (MR) is characterized by retinal hemorrhages of varying size and shape, often showing as Roth-spots, retinal whitening, papilloedema and vessel discolouration [19][22][23][24][6][25][27][144] and has been shown to be highly sensitive and specific in differentiating cerebral malaria (CM) from other causes of coma in pediatric [21] and adult patients [145]. The hallmark of CM is sequestration of parasites in the vessels of the central nervous system (CNS), but post-mortem studies have shown that many patients are misdiagnosed [146]. Reasons for this include incidental parasitaemia in high transmission settings and a lack of imaging, laboratory, and electroencephalography facilities in malaria endemic areas. Ophthalmological expertise that is crucial in diagnosing malarial retinopathy is often also lacking. Malarial retinopathy has great potential as a surrogate marker for adjunctive therapies but current methods of quantification and scoring severity of retinopathy are subjective and not evidence-based [19][20][5][28].

The number of retinal hemorrhages in CM correlates with the number of cerebral hemorrhages, so the detection of hemorrhages in MR is a logical first step [25]. Therefore, this article primarily focuses on the development of a method for automated detection of MR hemorrhages.

We have recently developed, studied, and validated retinal image analysis algorithms that are capable of detecting retinal hemorrhages, exudates, microaneurysms,

drusen, and cottonwool spots, as well as measure retinal arterial and venous parameters in retinal color fundus images, with performance comparable or superior to that of ophthalmologists [147][148][38][149][112][131]. We proposed a supervised pixel classification and red lesion detection method based on the analysis of features that include color, shape, and the response of a Gaussian filter-bank [38]. Sinthanayothin et al. [68] used a recursive region growing segmentation method accompanied by a binary thresholding which detects hemorrhages, microaneurysms and vasculature from the green channel image and removes vasculature from the final segmentation result. Remaining structures in the image were considered to be hemorrhages and microaneurysms. Gardner et al. presented a supervised algorithm in which a neural network was utilized for the classification of image regions containing hemorrhages and exudates [48]. However, these algorithms were targeted towards detection of diabetic retinopathy and age-related macular degeneration retinal phenotypes.

The purpose of the present pilot study is to evaluate an automated method for detecting MR associated retinal hemorrhages of varying size in retinal fundus color images on a dataset of 14 patients (200 images) previously diagnosed with MR.

### 3.5.2 Method

#### 3.5.2.1 Subjects

Patients were enrolled at Chittagong Medical College Hospital, Chittagong, Bangladesh. Adult patients diagnosed with severe P. falciparum malaria [145] based on the presence of asexual stage parasites in microscopy of their peripheral blood, and MR including retinal hemorrhages were included consecutively. All patients or their

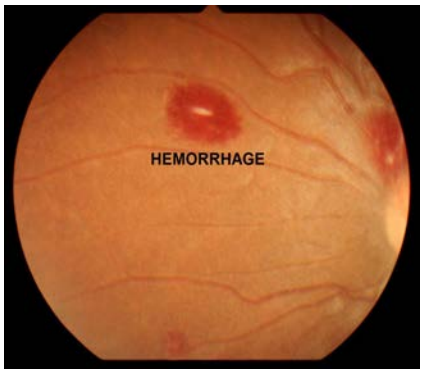


Figure 3.28: Image of a patient with MR with hemorrhages, notice the Roth spot

attending relatives provided written informed consent for participation in a larger study of malarial retinopathy from which the images used in the present study were taken. Retinal images were obtained from (both) eyes of all patients using a Kowa Genesis D handheld retinal camera through dilated pupils. Image resolution was 1200x1600. After imaging, images were deidentified and shared with the University of Iowa. The research team at University of Iowa did not have access to any patient identifiable information. The study was therefore declared exempt by the IRB of the University of Iowa. Ethical approval for the larger study on malarial retinopathy was obtained from the Bangladesh Medical Research Council ethics committee and the Oxford Tropical Research Ethics Committee (OXTREC).

#### 3.5.2.2 Overview of the method

The following block diagram (Fig. 3.29) shows the key steps in the method for detecting MR associated retinal hemorrhages.

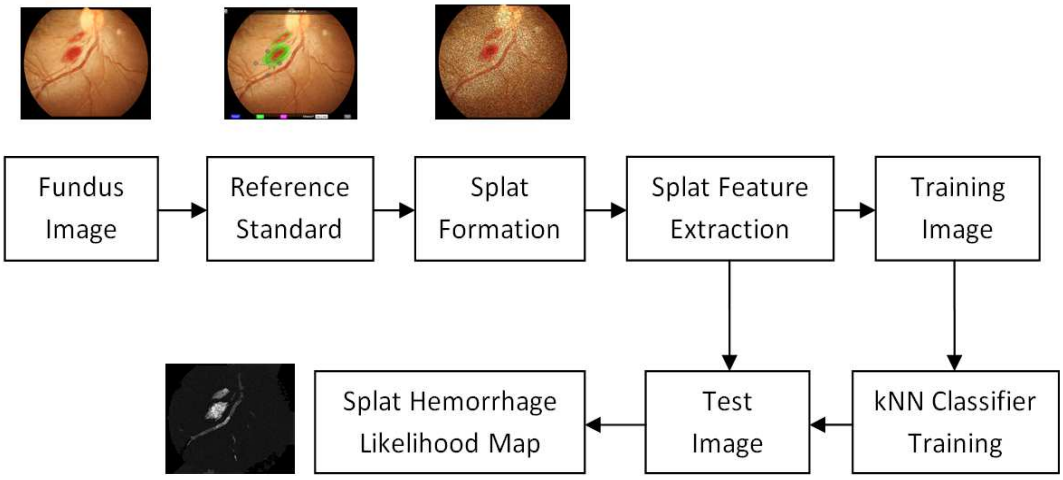


Figure 3.29: Block diagram showing the overview of the method

#### 3.5.2.3 Reference standard

A fellowship trained retinal specialist (MDA), masked to the algorithm results, manually segmented all hemorrhages in all images, using the iPad app Truthmarker that has been previously validated [12]. Fig. 3.30(a) shows the retinal fundus image and (Fig. 3.30(b)) shows the manual segmentation in action.

#### 3.5.2.4 Hemorrhage detection algorithm

The approach is a splat classification method, which we used previously for retinal image analysis [147][114], described as follows.

1) Division of a retinal image into splats: The method performs a watershed segmentation procedure (called 'tobogganing') to generate splats, which initially determines the gradient magnitudes of a grayscale version of a color image, at multiple scales and then utilizes their maximum for segmentation [150][151]. The maximum

Figure 3.30: Reference standard: a) Fundus image, b) Expert annotation using Truthmarker [12]

of the gradient magnitudes over scales represents a boundary between the contrast structures. The gradient magnitude at lower scale gives more response at the boundaries of smaller structures, and at higher scale gives more response at the boundaries of larger structures. Based on the boundaries formed, the image pixels are classified into catchment basin regions by grouping together the pixels with paths of steepest descent terminating at the same local minimum. Thus, the fundus image (Fig. 3.31(a)) is divided into a number of regions called 'splats' based on region homogeneity. I used a 'marker-controlled watershed segmentation method' in which the homogeneous regions in the image are initially marked by foreground markers (single pixel or a group of pixels) using morphological image reconstruction [152]. The regional maxima of the reconstructed image are used to obtain the foreground markers. The background markers are determined from the distance-transform of the binary version of the morphologically reconstructed image. The previously computed gradient magnitude image is modified so that it has regional minima only at the positions

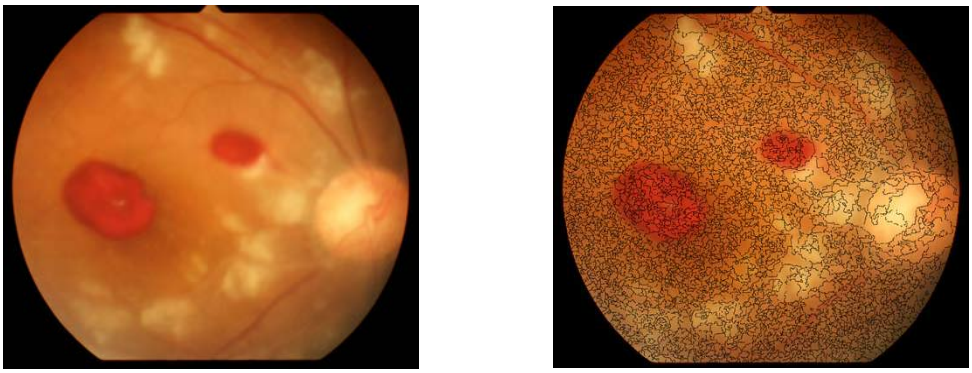

Figure 3.31: Splat formation: a) Fundus image, b) Image divided into splats

of foreground and background markers. Finally, the watershed segmentation of the modified gradient magnitude image is performed. The size of the structuring element selected for the morphological reconstruction controls the size of the marker and hence the splat size. To over-segment, I selected a 'disk' shaped structuring element of radius 1 pixel. The splats generated by the watershed segmentation of the fundus image (Fig. 3.31(a)) are shown in terms of splat boundaries overlaid on the image, in (Fig. 3.31(b)). The parameter settings result in approximately 4000 splats per image on average.

2) Splat feature extraction and classification: For each splat, a set of 43 features was calculated from the pixels within the splat (Tab.3.4). I chose features which represent the color as well as its variation across the fundus image. Some of the features in this set were used previously [147]. A subset (features: 1-6) of the feature set accounts for the mean color within a splat in RGB and HSV channels. The other subset (features: 7-42) characterizes the intensity variations across the fundus image

| Feature number | Feature description |
|---|---|
| 1-6 (6 features) | Mean of pixel values in a splat, for red, green, blue (RGB), and hue, saturation, value (HSV) channels |
| 7-42 (36 features) | Mean of pixel values at the splat boundary for difference of Gaussian image: (Ig - Io), Ig= Gaussian smoothing with $\sigma$=1, 2, 4, 6, 8, 10, Io= Original image, for each of RGB and HSV channels. |
| 43 (1 feature) | Mean of pixel values in a splat for Adaptive histogram equalization image |

Table 3.4: Features used for MR hemorrhage detection

in terms of difference of Gaussians at various scales ($\sigma$). I introduced a feature (43) of the mean intensity within a splat in adaptive histogram equalization image, which brings out the structural details due to the local contrast, at various scales.

A classifier was then trained on the feature set of each splat from a training set of images. I used a linear k-nearest neighbor (kNN) classifier [153][154] (See Appendix) based on Euclidean distance measurement for the supervised splat classification. The feature set of 43 features extracted from each of the splats in a training image, as above, represents the position of that splat in a forty three-dimensional feature space (training data point). The classifier is trained by associating the feature set with the label associated with the splat (hemorrhage or non-hemorrhage), derived from the reference standard created by the expert, as above. In the reference standard, a splat was labeled as a hemorrhage splat if more than 50% of the splat area was segmented manually.

In the testing phase, a feature set is extracted as above, from each splat in

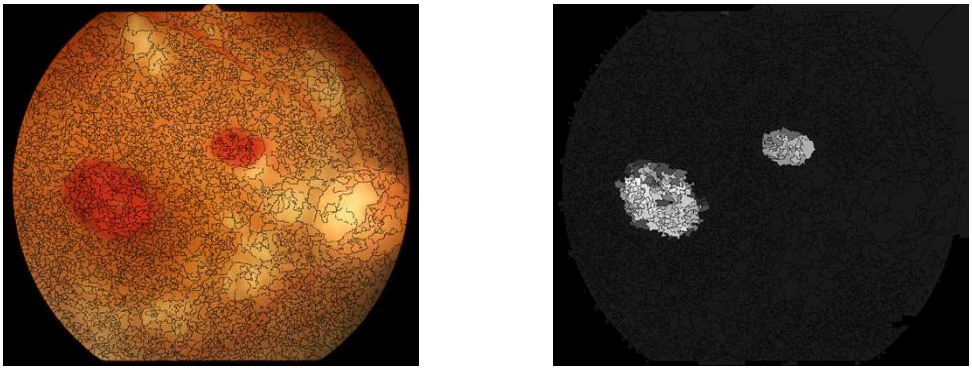

Figure 3.32: Hemorrhage detection: a) Fundus image with the overlaid splat boundary, b) Hemorrhage likelihood map: bright pixels indicate higher likelihood of the splat being a hemorrhage

the test image. The previously trained kNN classifier is then queried with the feature set, and provides the labels of 'k' nearest neighbors in the 43 dimensional feature space in return. The fraction of the 'k' nearest neighbors labeled as hemorrhage splat provides the likelihood, which is assigned to the test splat. This likelihood, a number between 0-1 is then assigned to all pixels belonging to the test splat, and a hemorrhageness map can thus be created, indicating how likely each splat is to be a part of hemorrhage, (Fig. 3.32(b)). The likelihood map can be thresholded at various values between 0 and 1, producing different system sensitivities and specificities, and thus producing a receiver operating characteristic (ROC) curve. The optimal value of 'k' for kNN classifier was determined based on area under the ROC curve (AUC). For this experiment, the maximum AUC was found corresponding at k=181.

3.5.2.5 Analysis

Performance of the algorithm was measured in a cross-over design experiment. The dataset of all patients was partitioned into two complementary subsets, 2 patients for testing and the remainder for training the classifier, and this process was then repeated 13 times for different permutations of the training set.

The performance was determined for splat-based as well as hemorrhage lesion-based analysis. The splat-based analysis measures how well the system can classify a splat as a part of hemorrhage or non-hemorrhage region, whereas the lesion-based analysis measures system performance in terms of classifying a retinal lesion as a hemorrhage or non-hemorrhage.

The following metrics were used:

1. True positive splats (or lesions) (TP): The number of splats (or lesions) marked by both the algorithm and the expert as hemorrhage.

2. False negative splats (or lesions) (FN): The number of splats (or lesions) marked as hemorrhage by the expert but not by the algorithm.

3. True negative splats (or lesions) (TN): The number of splats (or lesions) marked as non-hemorrhage by both the algorithm and the expert.

4. False positive splats (or lesions) (FP): The number of splats (or lesions) marked by the algorithm as hemorrhage but not by the expert.

$$Sensitivity = \frac{TP}{TP + FN} \qquad (3.6) \qquad Specificity = \frac{TN}{TN + FP} \qquad (3.7)$$

| | |
|---|---|
| Total hemorrhage splats | 454581 |
| False negative splats | 87143 |
| Total non-hemorrhage splats | 1862830 |
| False positive splats | 62032 |

Table 3.5: Performance in terms of splats,
at likelihood threshold of 0.12

| | |
|---|---|
| Sensitivity (%) | 80.83 |
| Specificity (%) | 96.67 |
| Area under the curve (AUC) | 0.9148 |
| 95% Confidence interval for AUC | 0.8254 to 0.9842 |

Table 3.6: Performance in terms of splats,
at likelihood threshold of 0.12

Sensitivity was defined as the fraction of hemorrhage splats (or lesions) marked by the expert (TP+FN), that were detected as hemorrhage splats (or lesions) by the algorithm (TP) (Eqn.3.6), while specificity was defined as the fraction of non-hemorrhage splats (or lesions) marked by the expert (TN+FP), that were detected as non-hemorrhage splats (or lesions) by the algorithm (TN) (Eqn.3.7). The hemorrhage lesion was considered 'detected' if at least one of the hemorrhage splats marked by the expert, was detected by the algorithm.

The total number of TP, FN, TN, and FP values for 14 test sets, and the respective sensitivity and specificity measures were evaluated by varying the threshold on the hemorrhage likelihood map. The sensitivity and specificity values obtained at the likelihood threshold of 0.12 are reported in Tab.3.6 for splat-based analysis,

| | |
|---|---|
| Total hemorrhage lesions | 917 |
| False negative lesions | 139 |
| False positive lesions | 1079 |

Table 3.7: Performance in terms of lesions, at likelihood threshold of 0.38

| | |
|---|---|
| Sensitivity (%) | 84.84 |
| False positive lesions/ Image | 3 |
| Area under the curve (AUC) | 0.9030 |
| 95% Confidence interval for AUC | 0.8724 to 0.9325 |

Table 3.8: Performance in terms of lesions, at likelihood threshold of 0.38

whereas the sensitivity and false positive values obtained at the likelihood threshold of 0.38 are reported in Tab.3.8 for lesion-based analysis. For the splat-based analysis, a receiver operating characteristic (ROC) curve was determined (Fig. 3.33(a)), whereas for the lesion-based analysis, a free-response operating characteristic (FROC) curve was obtained (Fig. 3.33(b)), using an online ROC analysis tool [155]. The FROC curve describing the actual performance of hemorrhage lesion detection, plots the sensitivity of the proposed method with respect to all hemorrhage lesions in the test set against the average number of false positives detected per image.

The ROC and area under the ROC curve (AUC) were reported for the sample of 14 patients included in the study. The AUC value is not a true value but the sample value with statistical error, and may vary for different samples [156]. Therefore, a

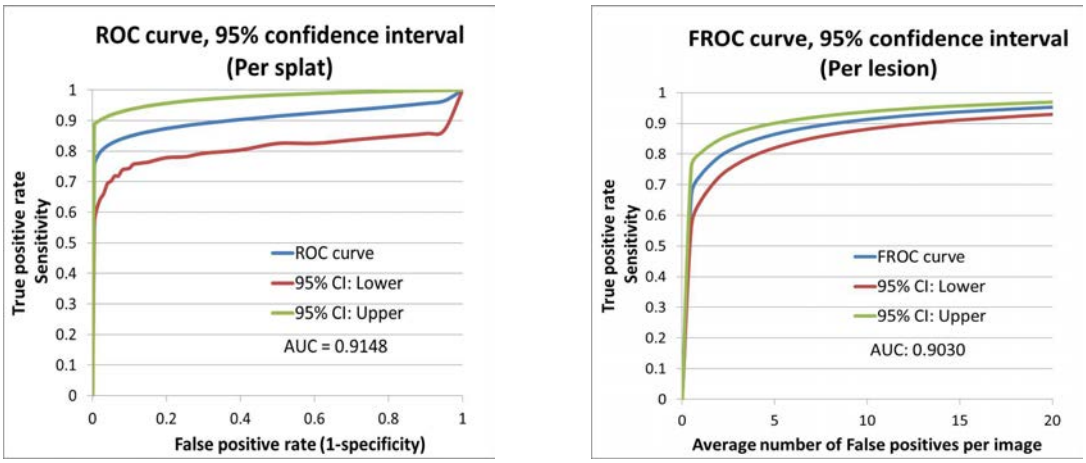


Figure 3.33: Performance: a) ROC curve: splat-based analysis, b) FROC curve: lesion-based analysis

range of AUC values (confidence interval: CI) is reported within which a true value lies with a certain degree of confidence. I included 95% confidence interval with the ROC curve representing the range of values in which the true value lies.

### 3.5.3 Results

For the splat-based analysis, the sensitivity and specificity values obtained from the ROC curve at the likelihood threshold of 0.12 are 80.83% and 96.67% respectively (see Tab.3.6). For the lesion-based analysis, the FROC curve shows the sensitivity of 84.84% against the average of 3 false positives detected per image, at the likelihood threshold of 0.38 (see Tab.3.8). The respective ROC and FROC curves are shown in Fig. 3.33. The AUC and the associated 95% CI on splat-basis are 0.9148 and [0.8254 to 0.9842] respectively, and that on lesion-basis are 0.9030 and [0.8724 to 0.9325] respectively. The average number of hemorrhages per patient detected by

the system was estimated to be 4 or more out of every 5 hemorrhages annotated in the reference standard. The running time required per image, was 10 minutes when processed on a standard personal computer with Intel core 2 Duo processor, running at 3 GHz.

### 3.5.4 Discussion

The results demonstrate that the automated method is capable of detecting retinal hemorrhages on retinal fundus color images, and match well with the reference standard as shown by area under the FROC curve (AUC=0.9030). The FROC curve and the corresponding AUC indicate the ability of the system to distinguish between hemorrhage and non-hemorrhage regions. This means that, given a randomly selected retinal region in the image, the automated system will correctly detect in 90.3% of cases the presence or absence of a hemorrhage in that region. Note that the reported lesion detection sensitivity of 84.84% is obtained at the cost of an average of 3 false positives (FP) per image, which may be a high FP rate for the application where the automated system is used to assist image analysis by a human.

Potentially, the use of automated techniques such as this, providing quantitative estimates of the signs of MR with good reproducibility may improve the objectivity of scoring and classification of malarial retinopathy. This technique has potential for assisting with assessment of malarial retinopathy in both research and clinical settings [157].

The varying shapes and sizes of hemorrhages were modeled in terms of splats, which enabled the splat specific feature extraction and classification. This decreases

the computation time required by pixel based classification and may prevent the inclusion of pixel level noise into the feature set.

This study has a few limitations worth mentioning. The technique is currently limited only to retinal hemorrhages, and when used alone these have poor specificity for severe malaria [145]. This is likely to be because they are not a result of the core pathological process of microvascular obstruction in severe malaria [157]. Future expansion of automated image assessment to the other features of retinal whitening, vessel discoloration and papilloedema, is ongoing.

The running time of the system may be considered high due to the small splat size. I chose the splat size depending upon the smallest hemorrhage size in the dataset. The smaller the size of a splat compared to that of the smallest hemorrhage, the more accurate may be the detection performance of the system. This is due to the ability of smaller splats to demark the hemorrhage boundaries more accurately compared to the larger ones. If the average splat size is greater than the hemorrhage size, it may include the surrounding background features into a feature space and may be classified erroneously. As the splat size decreases, the average running time increases due to increase in the number of splat feature extractions and classifications. Most of the running time was spent in the splat classification process. Future refinements to reduce this running time are needed so it can deal with large numbers of images rapidly.

Finally, training and test datasets consisted of images exclusively containing retinal hemorrhages. Though the system specificity for non-hemorrhage regions is

high, it may be advisable to include more test images with no hemorrhages, in order to avoid bias in the dataset. The future efforts will focus on analyzing larger datasets to provide a more robust assessment.

In summary, I developed an automated MR hemorrhage detection method based on splat classification and validated it on a dataset of patients previously diagnosed with MR. The results were validated with the reference standard showing the potential of the method in providing diagnostic assistance in detection of MR.

## 3.6 Analysis of a longitudinal study dataset

### 3.6.1 Introduction

The structural mapping of a retinal vessel network and its classification into arteries and veins was obtained [59], as explained in chapter 3. The morphology of a vessel network was quantified in terms of tortuosity, width, branching angle, branching coefficient, with respect to arteries and veins, and fractal dimensions. The morphologic parameters were measured with respect to each bifurcation across a vessel tree at seven vessel generations, for each vessel tree in a network. The vessel network analysis and morphology measurement were applied to a dataset of 70 subjects imaged over four time intervals (a longitudinal study). The statistical analysis results were presented to assess the possible correlation between the changes in vessel morphology and disease progression, or demographic parameters such as age.

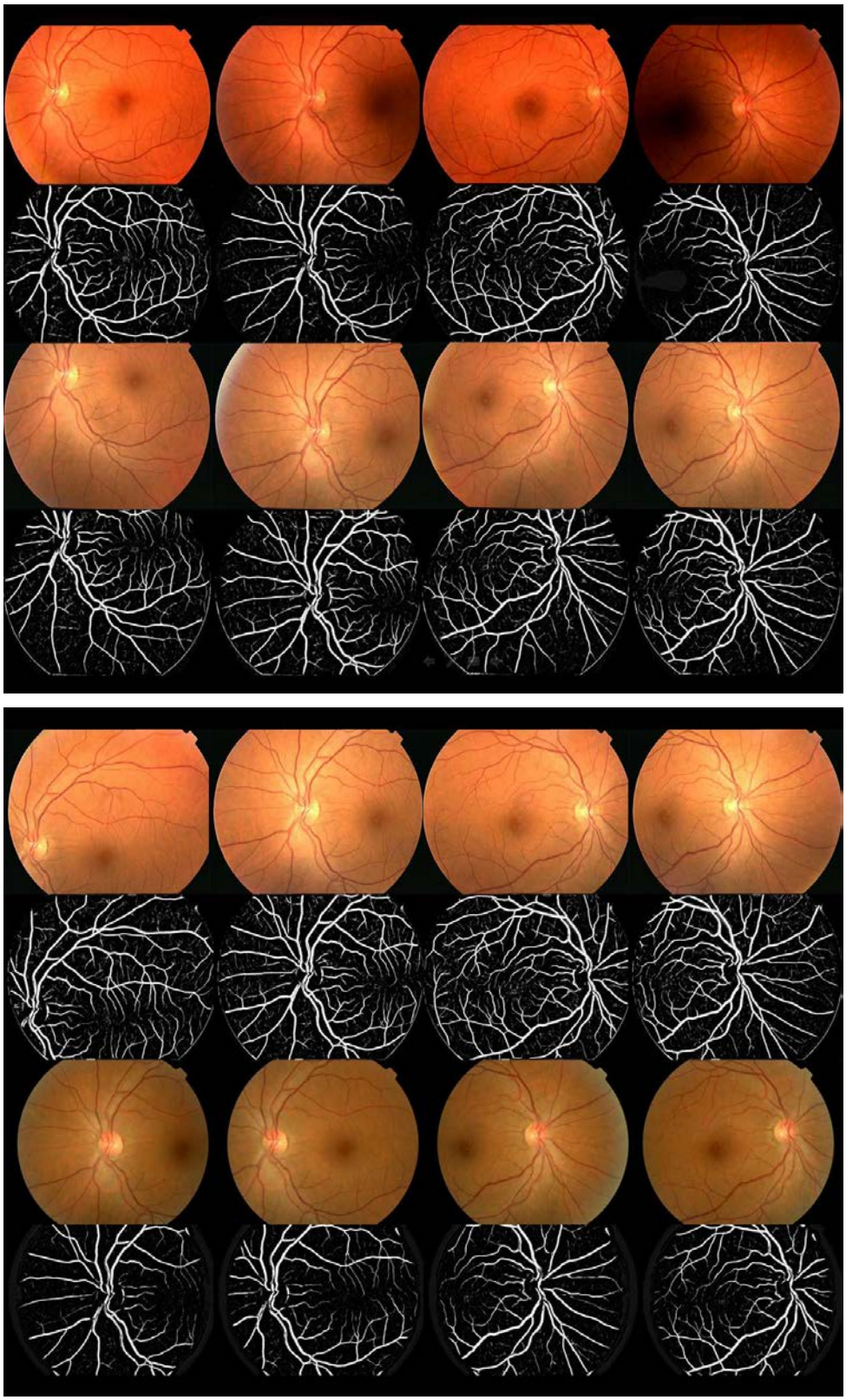

Figure 3.34: Four images captured at each of the four intervals and respective vessel segmentation:

### 3.6.2 Methods and Materials

A digital fundus color image dataset consists of 1120 images of 70 subjects selected randomly from a longitudinal study dataset. The four fundus images captured at each of the four intervals and the respective vessel segmentation, for one subject is shown in (Fig. 3.34). Referring to the figure, the data for one subject consists of four standard one-field fundus images (Image size: 768x576), one with optic-disc centered and one with fovea centered for each eye (first two columns: left eye, last two columns: right eye), captured at any one interval. The subject was imaged at 4 different intervals of time (fundus images in rows 1,3,5,7 in figure) but removed from the dataset as soon as any signs of diabetic retinopathy were observed. The average length of time interval between any two imaging instances was 1.14 years with the standard deviation of 0.28 years. The images were deidentified and patient's personal information was encapsulated from the research team. The retinal blood vessels were segmented (vessel segmentation in rows 2,4,6,8) using a previously validated segmentation method [33].

The structural mapping as well as artery-venous classification methods [59] were applied to the vessel segmentation obtained in the previous step, and five morphologic properties of a vessel network, viz., tortuosity, width, branching angle, branching coefficient, and fractal dimensions were measured. The measurement started at the root vessel segment (part of the vessel nearest to the optic disc) as first generation, and each of the vessel segments generated further at each bifurcation were labeled as successive generations, as shown in (Fig. 3.35). The first seven generations

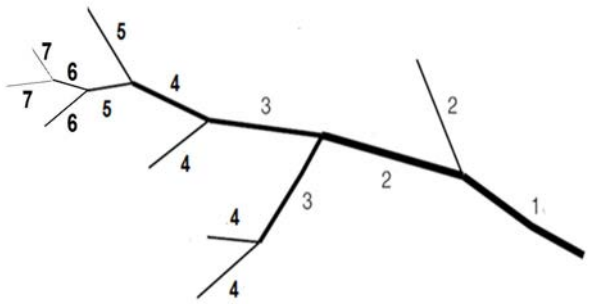


Figure 3.35: First seven vessel generations of a retinal vessel tree

of the vessel tree were considered for the analysis. The morphologic measurements for the vessel trees were averaged over the vessel network and over the images captured at any one interval. In the first pass of averaging procedure, the measured parameters were averaged for each generation over all the vessel trees across the vessel network. The second pass consisted of averaging the means of measured parameters in the first pass, over four images (four vessel networks) captured at any one interval. The measurement and averaging procedure was followed for arterial and venous vessel trees separately.

The tortuosity measurement was based on [112], whereas the measurements of width and branching angle were obtained as measured during the structural mapping process [59], explained in chapter 3. The branching coefficient was determined by the optimality ratio $\gamma = [(d_1^3 + d_2^3)/2 * d_0^3]^{0.33})$ defined in [89]. The fractal dimensions were measured using a box-counting method. Therefore, each morphologic property except

fractal dimension, was measured at first seven generations of the vessel network, separately for arteries and veins, yielding total of 14 measurements at each interval. The process was repeated for all the 4 intervals giving a set of 56 measurements of each property for a subject. The fractal dimension measurements for four images at an interval were averaged, and four average measurements were obtained at four respective intervals.

### 3.6.3 Results

I applied the proposed method to a dataset of 70 subjects each with images obtained at four time intervals. The measurement of morphologic parameters such as tortuosity, width, branching angle, and branching coefficient yielded 4 averaged measurements at respective time intervals, at each generation separately for arteries and veins. The 'analysis of variance (ANOVA)' test was carried out to analyze the possible statistically significant changes in a morphologic parameter across four time intervals. The ANOVA tests for tortuosity, width, branching angle, and branching coefficient were not statistically significant for arteries or veins. The graphical results are shown in the appendix section.

The fractal dimension measurement presented 4 measurements for vessel networks at respective time intervals (Fig. 3.36). The ANOVA test for fractal dimension analysis was statistically significant with (F=15.75 $\geq$ $F_{crit}$), where $F_{crit}$=2.64 and p-value $\leq$ 0.05 ($\alpha$=0.05). Furthermore, Tukey post-hoc [HSD(q)] test results for 70 subjects, were presented in (Tab.3.9) at $\alpha$=0.05 and critical value of q=3.63. The second row of the table represents the mean fractal dimension at respective interval,

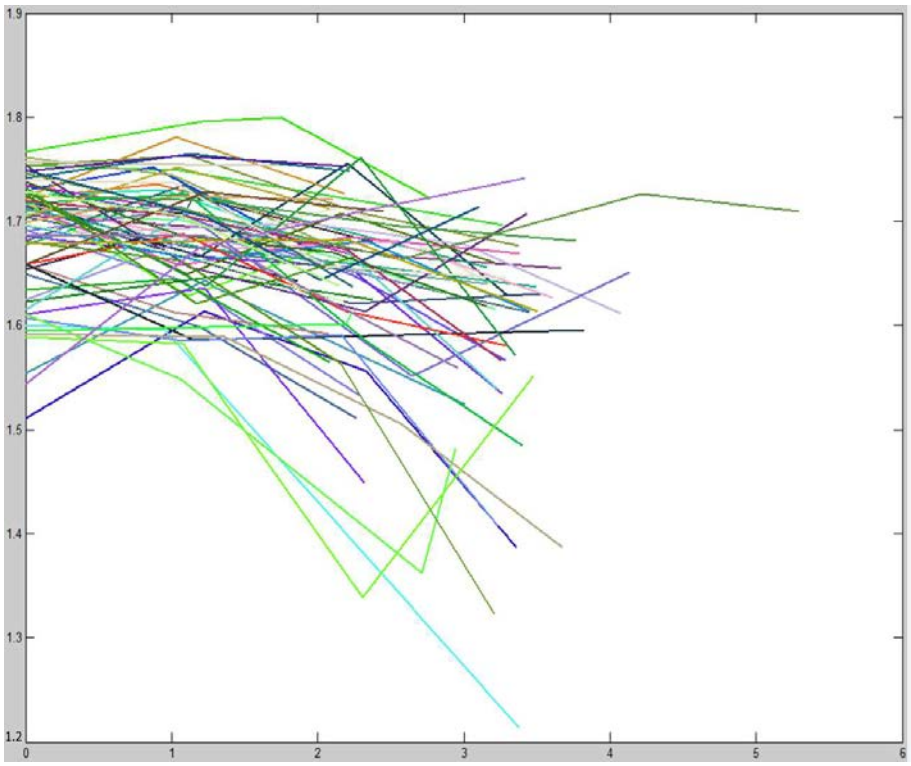


Figure 3.36: Fractal dimension, X-axis: 0 to 6 years, Y-axis: 1.2 to 1.9

over 70 subjects. Referring to the same table, intervals 1,2, and 3 (rows 4,5,6) present the HSD(q) values in relation with the respective intervals 1,2,3,4 (columns 2,3,4,5). The higher HSD(q) values compared to the critical value of q may conclude that the differences between all of the intervals were statistically significant except those between interval 1 and interval 2.

### 3.6.4 Discussion

The set of automated image analysis and morphology measurement algorithms was applied to the dataset. The retinal vessels were separated and classified into arteries and veins, and were measured for the changes in morphologic properties across

| Tukey post-hoc | Interval 1 | Interval 2 | Interval 3 | Interval 4 |
|---|---|---|---|---|
| Mean | 1.6889 | 1.6824 | 1.6401 | 1.5973 |
| Tukey HSD(q) | | | | |
| Interval 1 | 0 | 0.7140 | 5.3611 | 10.0630 |
| Interval 2 | | 0 | 4.6470 | 9.3489 |
| Interval 3 | | | 0 | 4.7019 |

Table 3.9: Tukey post-hoc test results,
at the critical value of q=3.63

four time intervals. The results show that the morphologic parameters, viz., tortuosity, width, branching angle, and branching coefficient measured across 4 intervals of time did not change significantly. The possible reasons could be the following:

1. The image quality and image resolution may not be high enough to capture relatively minute changes in anatomy of vessels, which may be reflected in higher resolution images.

2. The field of view of the images across the same interval as well across different intervals for the same subject may be different. The field of view for different images may cover different retinal regions and hence the consistency of morphology measurement on the same set of vessels across intervals may be compromised.

3. The subjects were removed on the onset of diabetic retinopathy, i.e., as soon as any sign of diabetic retinopathy was observed. Thus, the vessel morphology might not have changed significantly which could be observed under the effect of moderate or severe retinopathy.

4. The accuracy of vessel segmentation is crucial as the success of vessel analysis and

measurement algorithms is based on vessel segmentation. Therefore, it may need a more accurate vessel segmentation to capture minute changes in the vessel morphology such as small changes in width and branching angle.

5. It may need more accurate morphology measurement algorithms which can capture even a minute change in vessel anatomy from fundus images.

As evident from the statistical analysis, the differences in fractal dimensions across four intervals were statistically significant, except that between interval 1 and interval 2. Although the observed differences were quantitatively different, it appeared from the visual inspection of images that the source of these differences may not be the anatomic change in vessel fractal properties. The set of images obtained at some intervals may be affected by the imaging defect which was either the effect of imaging device limitations in terms of focus and illumination, or due to the anatomic changes in subjects eye such as cataract which may have prevented the illumination of retina [158]. This may also be the effect of collecting images at different intervals from different imaging sites, captured with different cameras, imaging specifications, and variably skilled imaging specialists. The aforementioned effects are shown in (Fig. 3.37). The defects in the fundus image were carried forward in the segmentation of vessels, and vessels were segmented either with interruptions or with the loss of smaller vessel segments ($\leq$4 pixels width). The fractal dimensions not only measure the ability of vessel network to fill the embedding space but also the degree or the kind of vascular branching with which the embedding space is filled up [107]. Therefore, the presence or absence of smaller vessel segments may affect the measurement of

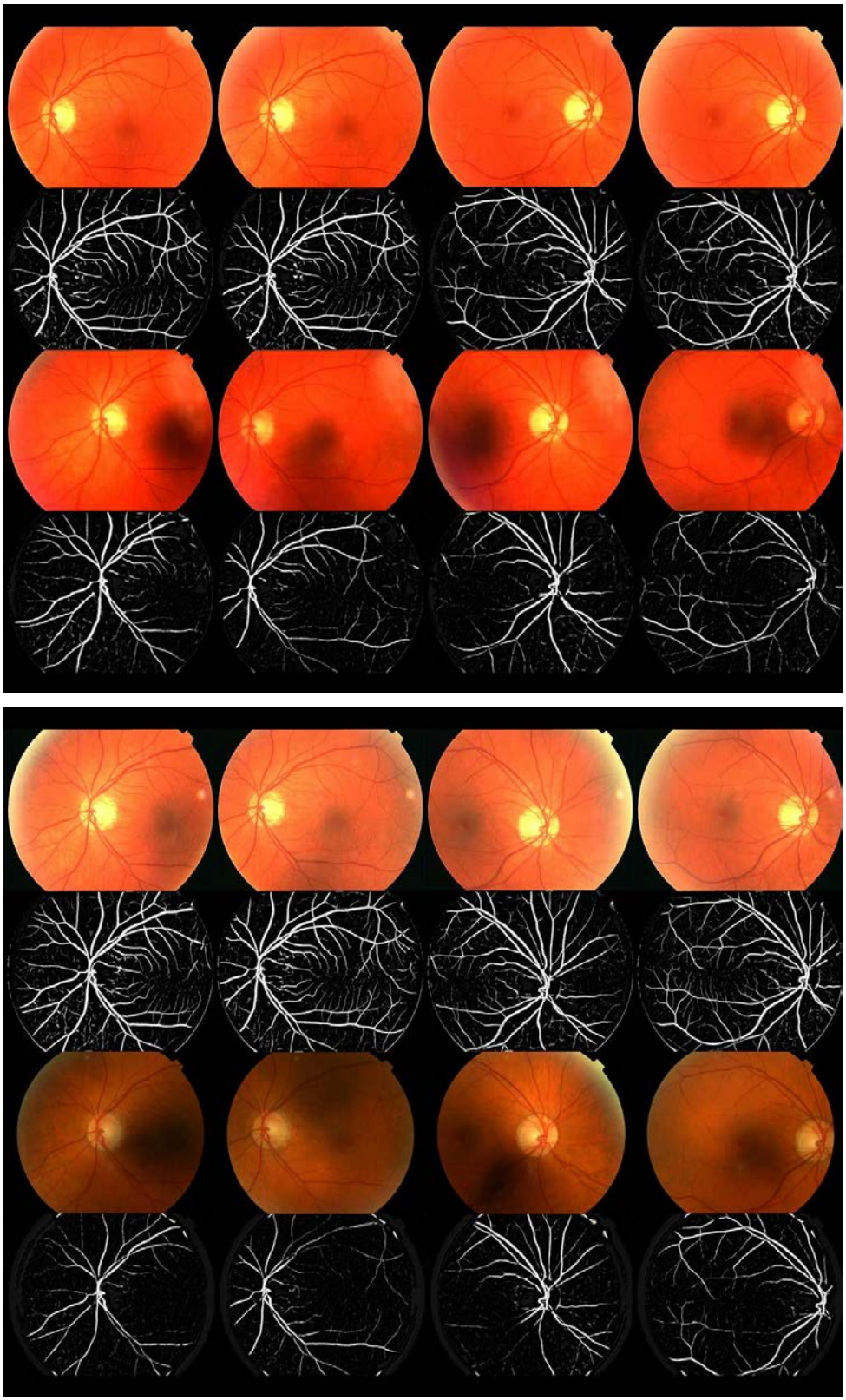

Figure 3.37: Effects of imaging process or anatomic changes in the eye (e.g., cataract) on images captured at each of the four intervals and respective vessel segmentation

fractal dimension. Due to the imaging defects or the anatomic changes leading to imaging limitations, the true changes in the anatomy of vessels may not be measured, but may lead to statistically significant results which do not correspond to the true morphologic changes.

### 3.6.5 Conclusion

I developed a set of automated retinal image analysis methods and applied it to a longitudinal study dataset to quantify the possible changes in vessel morphology under the effect of a disease or a demographic factor such as age. The morphologic characteristics such as tortuosity, width, branching angle, and branching coefficient did not change significantly across four time intervals. The fractal dimensions changed significantly across four time intervals, but the true reason behind this change may not be the anatomic changes in vessel fractals but the possible imaging defects. The morphologic analysis of individual vessel trees in terms of arteries and veins, and that of a vessel network may be implemented with the set of methods proposed in this thesis. The automated retinal image analysis has potential in providing vessel specific as well as network specific morphologic measurements for the automated diagnosis of retinopathies.

# CHAPTER 4
# DISCUSSION AND CONCLUSION

In this chapter, I discuss results and conclude the thesis.

## 4.1 Summary of Results

In this thesis, I proposed and validated the set of mathods for automated morphology analysis of retinal blood vessel network. The thesis consisted of methods analyzing the retinal structure such as structural mapping, reconnection of interrupted vessels, artery-venous classification, and the methods measuring or detecting the morphologic changes in the retinal structure such as vessel tortuosity measurement and malarial retinopathy hemorrhage detection. In this section I summarize the results followed by the discussion.

### 4.1.1 Identification and reconnection of interrupted vessels in retinal vessel segmentation

An automated method for identifying the interruptions in retinal vessel segmentation, and means of reconnecting the vessel segments to the primary vessel structure was reported. Dijkstra's graph search algorithm determines the minimum cost path that connects the disconnected vessel segment to its primary vessel, based on intensity and direction matching. The path is verified by applying the tortuosity and connection strength constraints. The application of algorithm to a dataset of 25 vessel segmentation images resulted into 81.63% of reduction in vessel interruptions

obtained by the manual reconnection process. The results show that the number of interruptions in the automatically reconnected vessel images reduced significantly and approached the value obtained for manually reconnected vessel images. The tortuosity measurement based analysis compared with the experts tortuosity assessment, resulted into the automated reconnection method showing improvement in the correlation coefficient ($r_s$=0.68) compared with that showed by the interrupted network tortuosity ($r_s$=0.58). It suggests that the method may provide a connected vessel network for presenting true and consistent morphologic analysis.

### 4.1.2 Automated method for identification and artery-venous classification of vessel trees in retinal vessel networks

A novel approach for identification and separation of retinal vessel trees in a retinal color image, and their classification into arteries and veins was reported. The automated method models a vessel segmentation image as a vessel segment map and identifies the individual vessel trees by a Dijkstra's graph search algorithm. The structurally separated vessel trees are utilized for color feature extraction and AV crossing detection, and vessel trees are classified into arteries and veins by a fuzzy C-means clustering algorithm. I applied the method to a dataset of 50 fundus images from 50 subjects. Structural mapping based AV classification method resulted in an accuracy of 91.44% correctly classified vessel pixels in a vessel network. The accuracy of correct classification of diagostically important major vessel segments was 96.42%. The results demonstrate that the automated method is capable of separating and classifying the retinal vessel trees with the accuracy comparable to that of experts

annotation performance, and may provide a reliable source of structural information for retinal vessel characterization and the respective morphologic assessment.

### 4.1.3 Automated measurement of retinal blood vessel tortuosity

A new quantitative metric for vascular tortuosity measurement was reported. It measures vessel's angle of curvature, length of the curved vessel over its chord length (arc to chord ratio), number of curvature sign changes, and combines them into a quantitative metric called tortuosity index (TI). I applied this method to a dataset of 15 digital fundus images of 8 patients with facioscapulohumeral muscular dystrophy (FSHD), of which the arterial and venous tortuosities have also been graded by blinded experts (ophthalmologists). Spearmans correlation between the tortuosity index by the method and that by manual tortuosity grading for arteries was $r_s$=0.98, and that for veins was $r_s$=0.77. The results show high correlation with expert's subjective estimates suggesting that TI has potential to detect and evaluate abnormal retinal vascular structure in terms of tortuosity measures.

### 4.1.4 Automated detection of malarial retinopathy associated retinal hemorrhages

Automated MR hemorrhage detection method based on splat classification was reported and validated on a dataset of 14 patients previously diagnosed with MR. A pattern recognition based algorithm was developed which extracts a feature set from the image watershed regions called splats (tobogganing) and trains a linear k-nearest

neighbor classifier to distinguish hemorrhages from non-hemorrhage regions in a test dataset. The results were validated with the reference standard and hemorrhage detection sensitivities in terms of splats and in terms of lesions were reported as 80.83% and 84.84% respectively. The splat-based specificity was 96.67%, whereas for the lesion-based analysis an average of 3 false positives was obtained per image. The area under the receiver operating characteristic curves was reported as 0.9148 for splat-based, and 0.9030 for lesion-based analysis. The results demonstrated that the automated method may be capable of detecting retinal hemorrhages on retinal fundus color images, and matched well with the reference standard. With further development, this technique has its potential in providing automated assistance to screening for and quantification of malarial retinopathy.

## 4.2 Conclusion

This thesis presents automated image analysis approach which consists of set of methods to analyze and to measure the morphology of retinal blood vessel structure. These methods were validated on respective datasets resulting into a performance comparable to retinal experts.

The basis for the automated analysis of vessel structure is a vessel segmentation image which gives a likelihood of each pixel in the image being inside the vessel. The accuracy and consistency of vessel segmentation is a backbone of the automated methods presented in the thesis and any errors in the segmentation may be carried forward through the analysis pipeline, though the method for reconnecting interrupted vessels partially corrects for the segmentation errors.

The advantages of the proposed methods include complete automation of the vessel network analysis, automation of the morphologic characterization and measurement, quantification of results compared to the subjective assessment by an ophthalmologist, and quick analysis relative to the time-consuming work by a retinal expert.

In this thesis, I propose to evaluate the association between morphologic changes in retinal vasculature and the occurrance or progression of retinopathies and systemic diseases. I describe the automated image analysis methods in order to quantify the morphologic properties of retinal vessel network that may provide an objective evaluation of retinopathies such as diabetic retinopathy and malarial retinopathy.

## 4.3 Future Work

Here, I discuss some directions for the future research to analyze retinal vessel structure and measure its morphologic characteristics.

### 4.3.1 Automated retinal image analysis software package

Currently, a set of methods has been proposed which analyzes and measures the retinal vessel morphology. These methods are based on the vessel segmentation and form a pipeline leading to a set of quantitative indices describing the retinal vessel morphology which include tortuosity, branching angle, branching coefficient, vessel width, and fractal dimensions. In the future work, the methods may be combined to

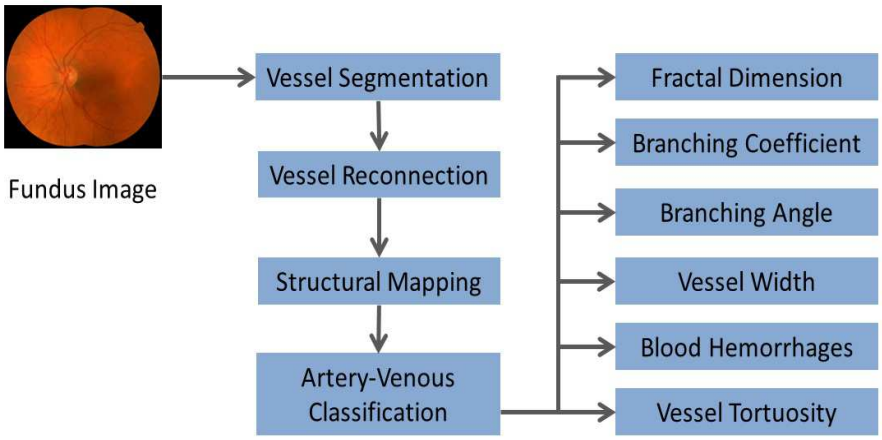


Figure 4.1: Automated retinal image analysis software

form a software package or an executable package which accepts an input as retinal color fundus image and outputs a set of numerical indices describing the current status of the vessel morphology, as shown in (Fig. 4.1).

### 4.3.2 Automated diagnostic system based on clinical input

The aforementioned software package may further be developed into a system to accept an accessory input from clinical analysis of a vessel morphology. An extensive clinical evaluation of a certain retinopathy may be used to train the automated system to set thresholds on each numerical index measuring the morphologic property. Once trained, the system may be able to compare the current numerical measurement status of each morphologic property with the respective threshold to provide the diagnosis in terms of detection or progression of the retinopathy.

# APPENDIX A
# APPENDIX

In this chapter, I describe the graph algorithm methods as well as the classification methods utilized in the thesis.

## A.1 Dijkstra's graph search

Dijkstra's graph search algorithm [159] determines the minimum cost path to each node in the graph from the source node $S$. It maintains the list of 'explored' nodes ($q$) (previously visited nodes) for which the minimum cost path is determined ($d_{(q)}$). Furthermore, it adds 'unexplored' nodes ($p$) to the list of 'explored' nodes by determining the minimum cost path ($d_{(p)}$) from the source node $S$. The Dijkstra's algorithmic function may be explained by eqn. A.1. It searches for a minimum edge cost path that connects the node $p$ with the source node $S$, by minimizing the sum of edge costs $E$ between intermediate nodes ($q$) on the path.

$$d_{(p)} = \min_{q \in S} [d_{(q)} + E(q, p)] \tag{A.1}$$

## A.2 k Nearest Neighbor classifier (kNN)

kNN classifier is a supervised classifier which calculates the probability for a test data of its belongingness to a particular class, based on the class of training data samples in its neighborhood [153][154]. The classifier is trained with the feature vectors obtained from the training data samples and the labels associated with the

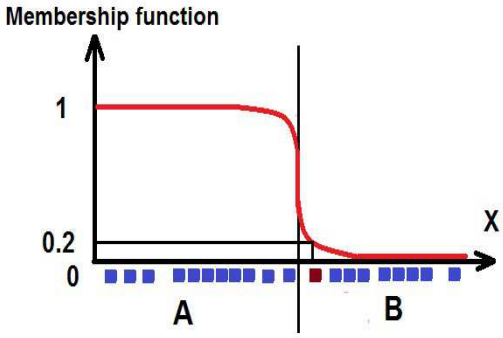


Figure A.1: Fuzzy C-means clustering

respective training samples obtained from the reference standard (ground truth). Once trained, the classifier may be able to distinguish between the samples of different classes. For an unseen data (test data) sample, the classifier extracts the feature vector and determines the position of the test data sample in the feature space. Based on the experiments performed on the training data (e.g., maximum area under the receiver operating characteristic curve), the optimal number of nearest neighbors (k) is determined. The classifier searches the 'k' nearest neighbors of the test data sample in the feature space formed by the training samples, and assigns a probability to the test sample which is the fraction of 'k' nearest neighbors (training samples) belonging to a particular class. The 'k' nearest neighbors are searched based on their Euclidean distance from the test sample.

## A.3 Fuzzy C-means clustering

Clustering is an unsupervised method of dividing the data samples into definite number of non-empty groups, such that the data in a group possess relative closeness

in terms of a defined distance function. Fuzzy C-means clustering allows a data sample to be associated with number of clusters (groups) with a defined degree of association based on its distance from the cluster centroid [160][161] (Fig. A.1).

Any data sample has a set of coefficients giving the degree of belongingness to each cluster. Each cluster centroid is determined by the average of all data samples in a cluster, weighted by their degree of belongingness. The degree of belongingness $Degree_k(x)$ is determined by eqn. A.2, where $C_k$ is a cluster centroid, $C_j$ are other cluster centroids, $x$ is a data sample, m is a level of fuzziness, and distance between any centroid and $x$ is determined by Euclidean or other distance metrices.

$$Degree_k(x) = \frac{1}{\Sigma_j[(Distance(C_k, x)/Distance(C_j, x))^{(2/(m-1))}]} \tag{A.2}$$

## A.4 Results: Longitudinal study dataset

I applied the proposed methods to the longitudinal study dataset of 70 subjects each with images obtained at four time intervals. The measurement of morphologic parameters such as tortuosity, width, branching angle, and branching coefficient yielded 4 averaged measurements at respective time intervals, at each generation separately for arteries and veins as shown in Fig. A.2, Fig. A.3, Fig. A.4, Fig. A.5, Fig. A.6, Fig. A.7, Fig. A.8, Fig. A.9, Fig. A.10, Fig. A.11, Fig. A.12, Fig. A.13.

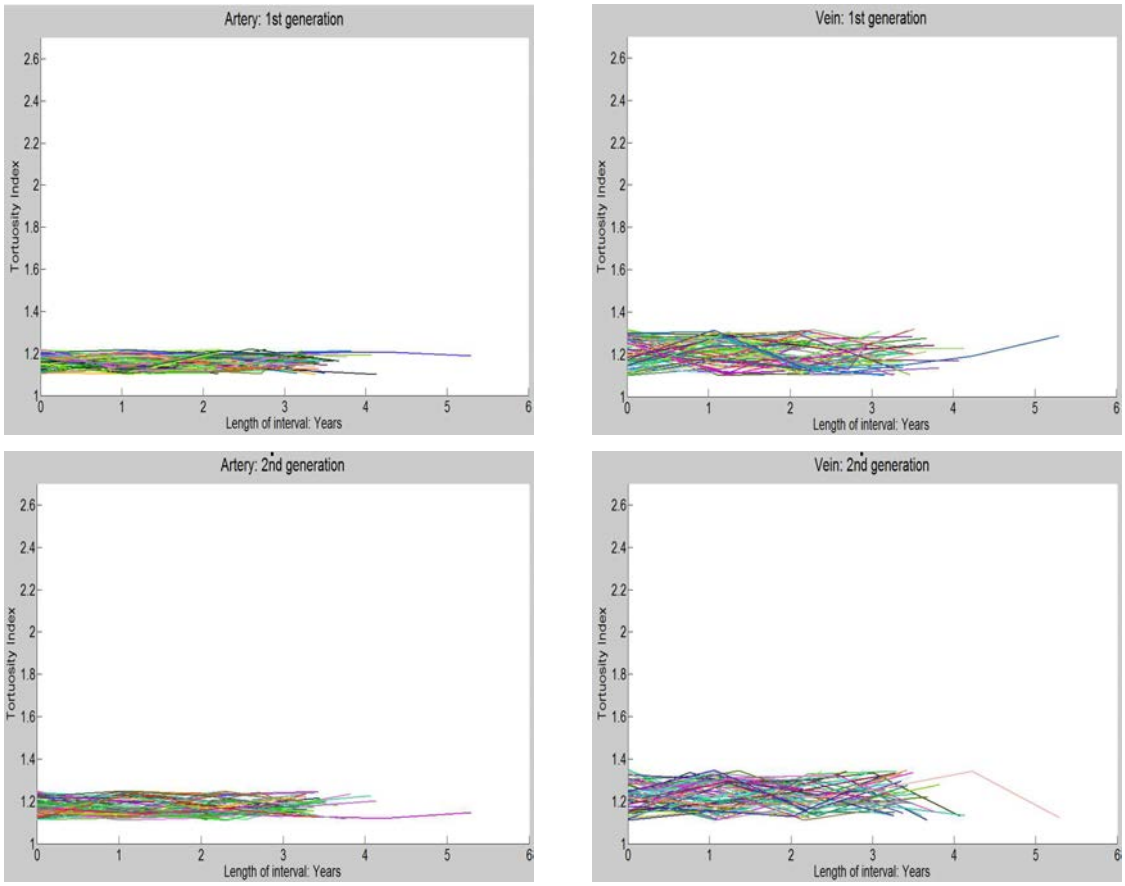


Figure A.2: Tortuosity index, X-axis: 0 to 6 years, Y-axis: 1 to 2.7

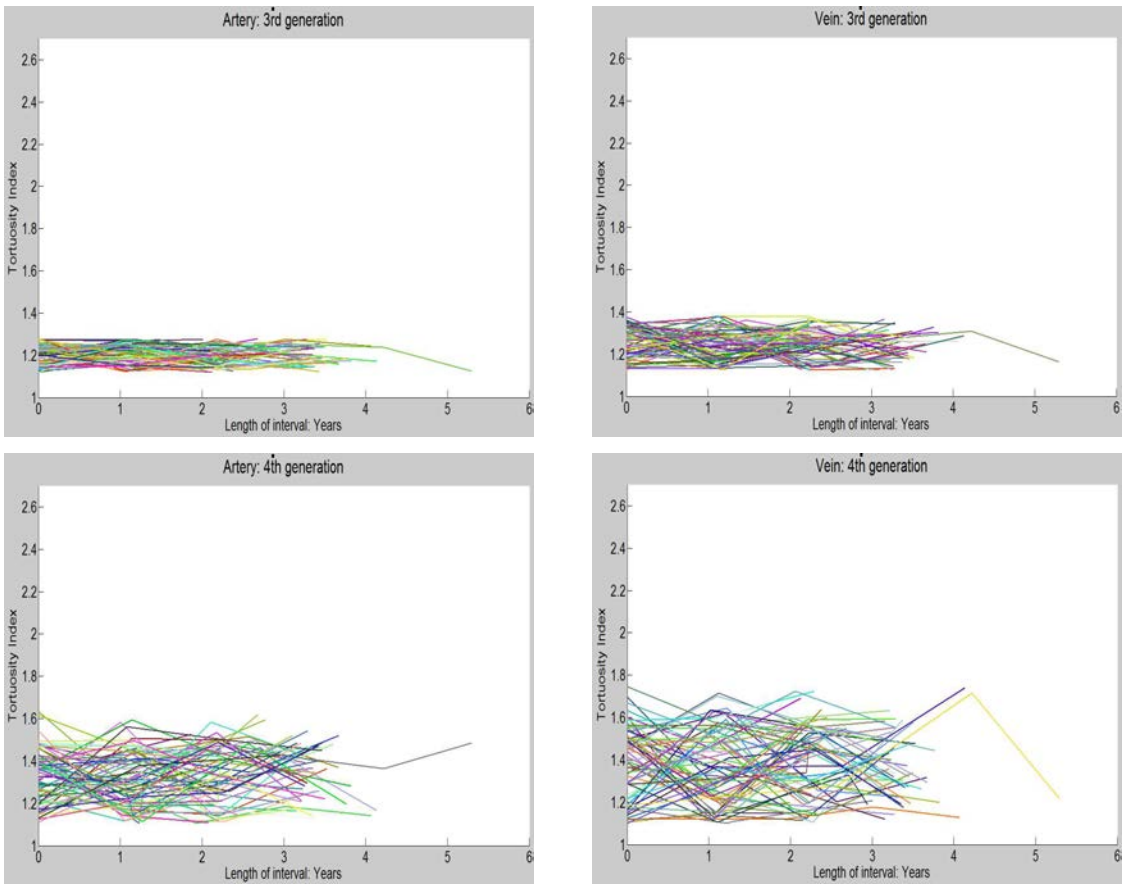


Figure A.3: Tortuosity index, X-axis: 0 to 6 years, Y-axis: 1 to 2.7

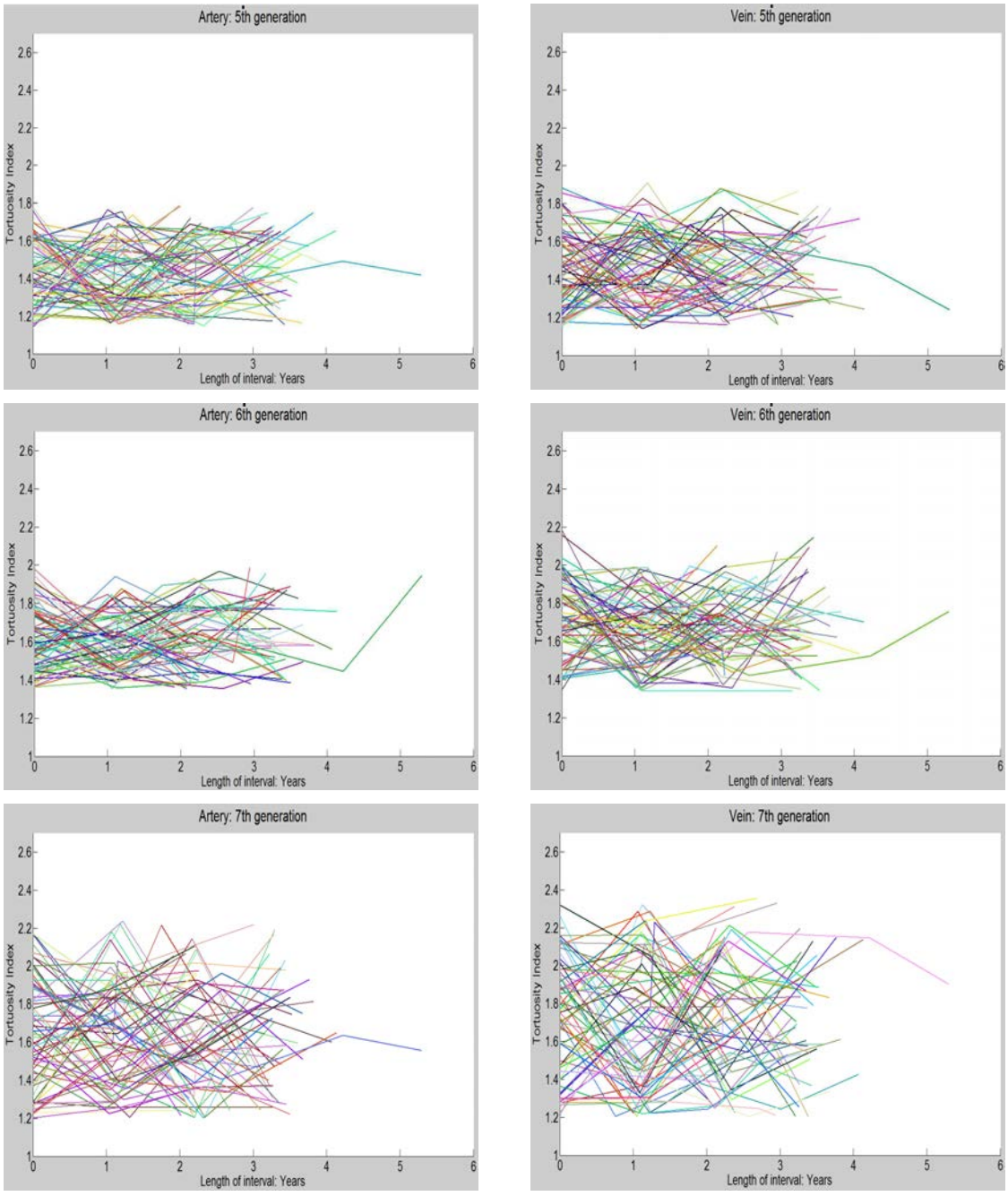


Figure A.4: Tortuosity index, X-axis: 0 to 6 years, Y-axis: 1 to 2.7

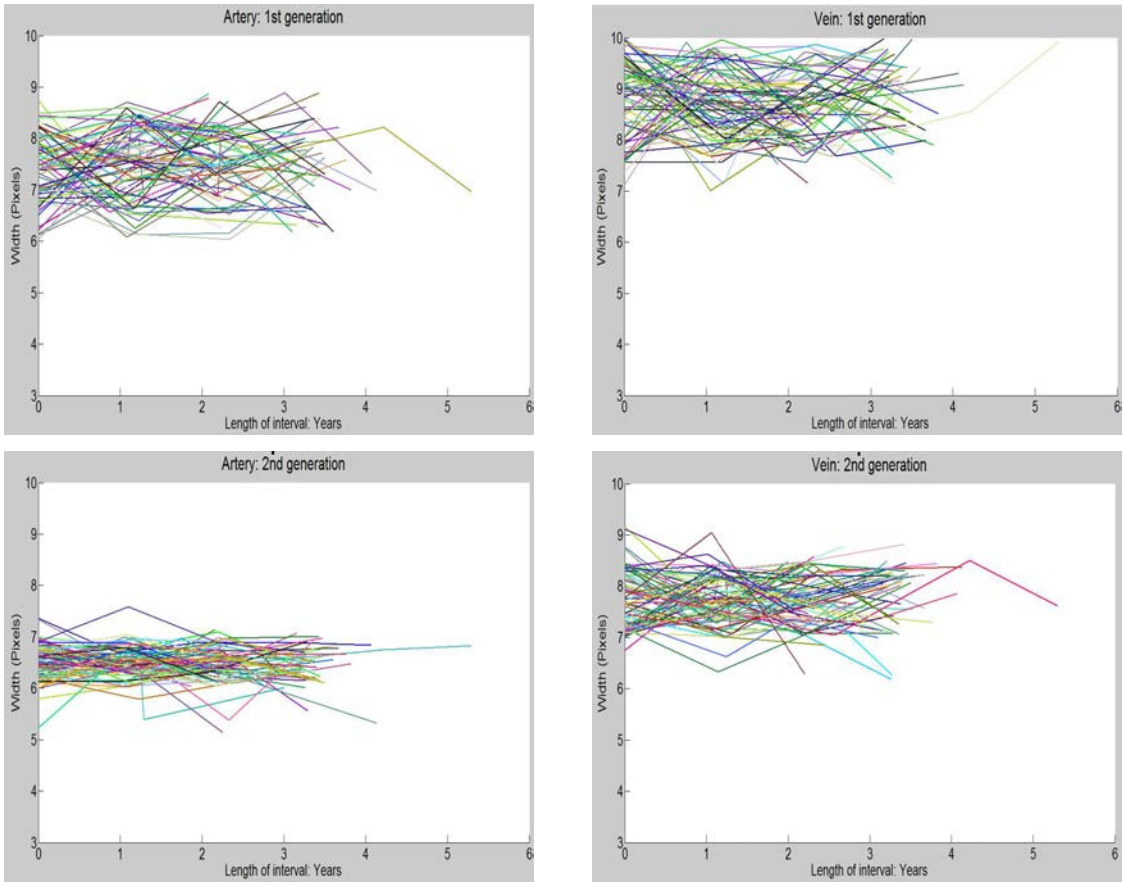


Figure A.5: Width, X-axis: 0 to 6 years, Y-axis: 3 to 10 pixels

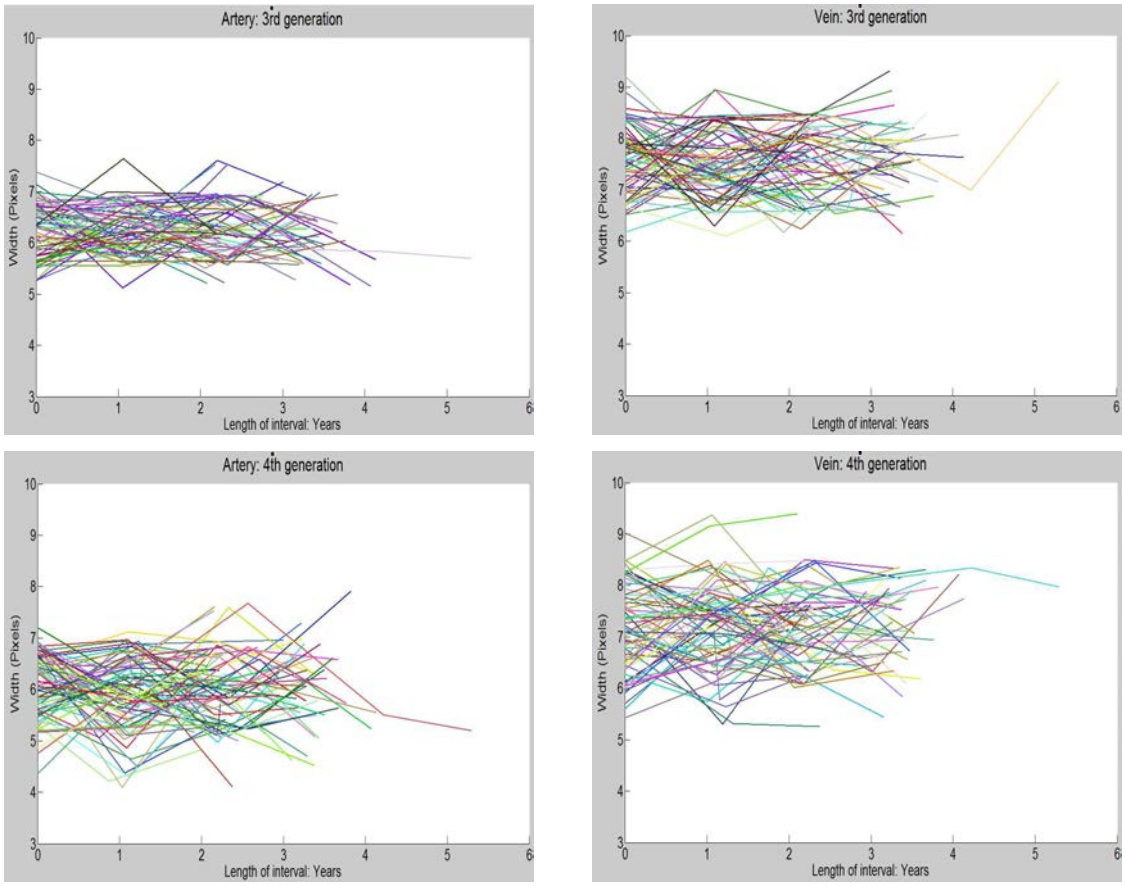


Figure A.6: Width, X-axis: 0 to 6 years, Y-axis: 3 to 10 pixels

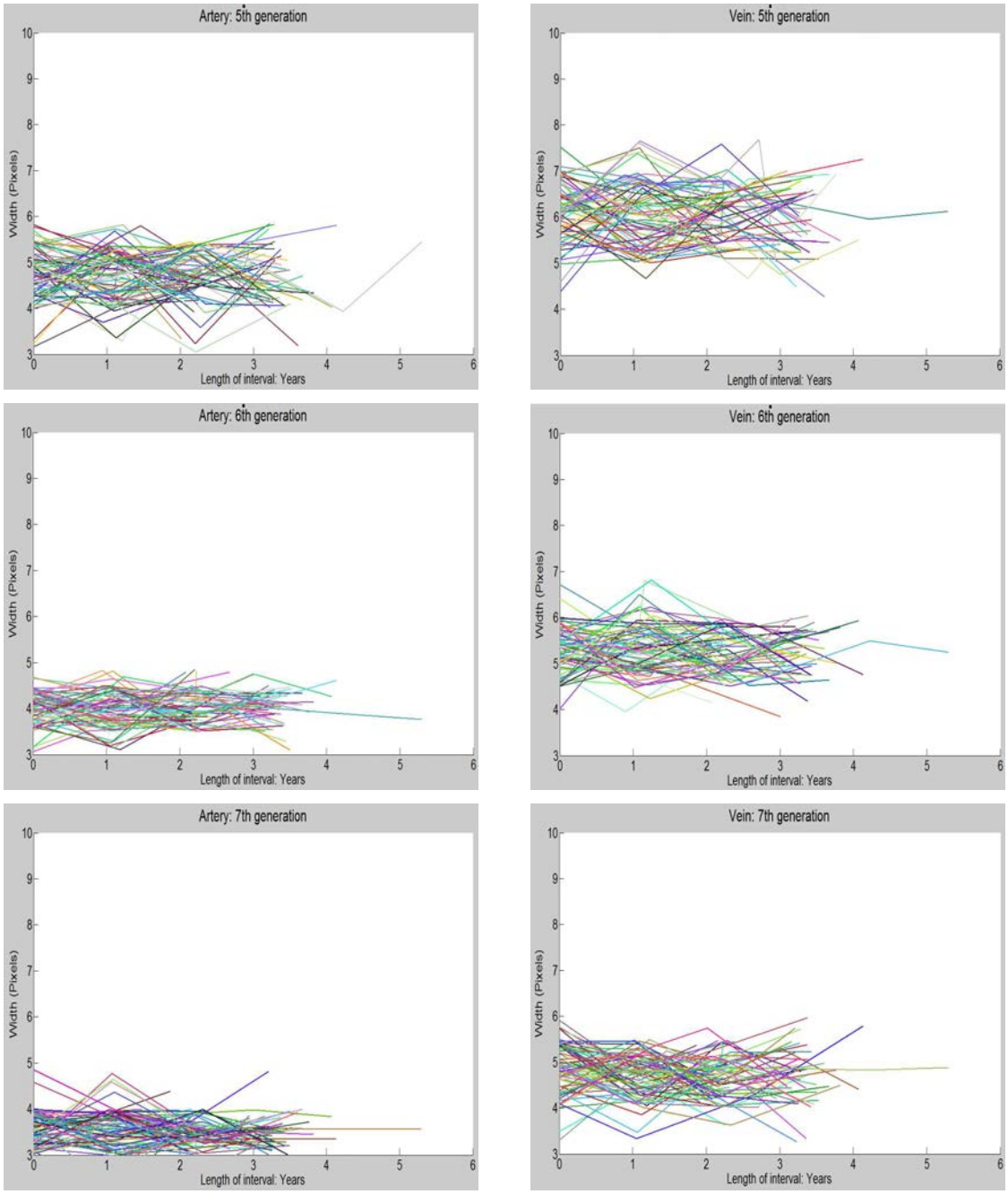


Figure A.7: Width, X-axis: 0 to 6 years, Y-axis: 3 to 10 pixels

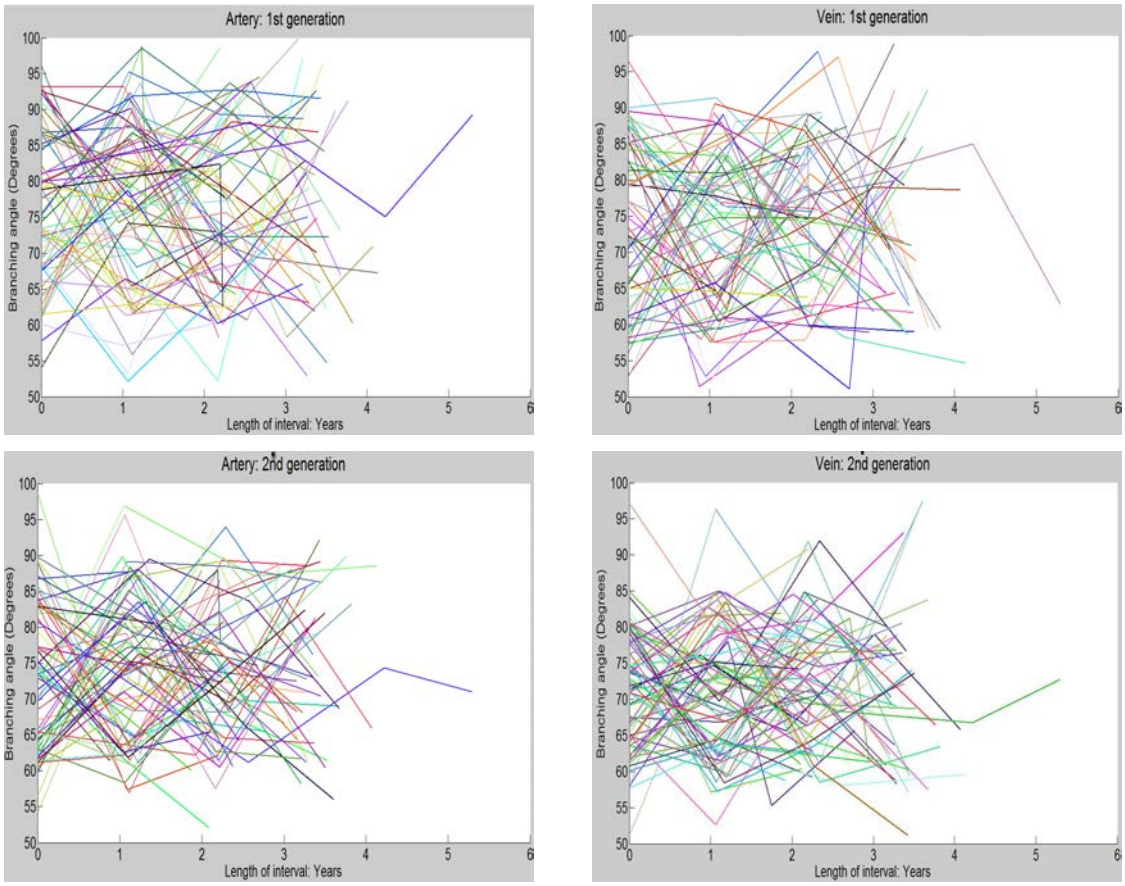


Figure A.8: Branching angle, X-axis: 0 to 6 years, Y-axis: 50 to 100 degrees

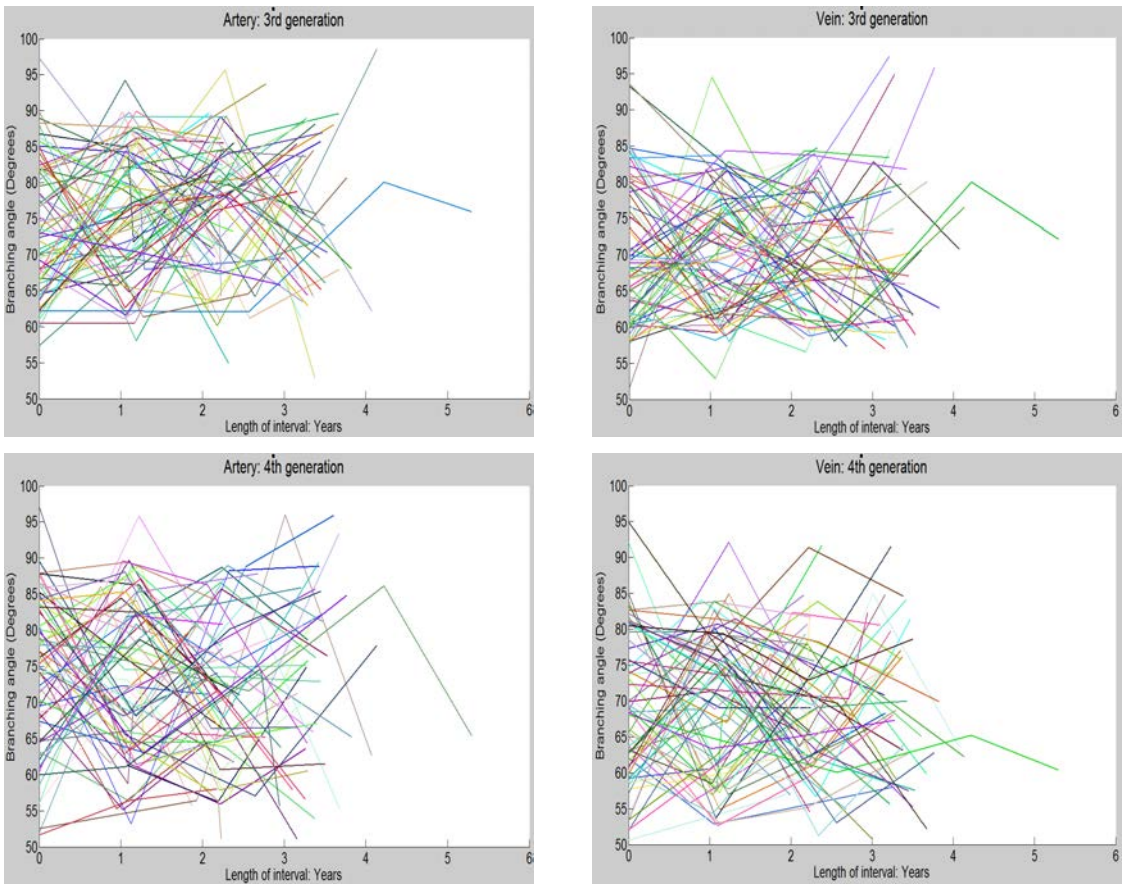


Figure A.9: Branching angle, X-axis: 0 to 6 years, Y-axis: 50 to 100 degrees

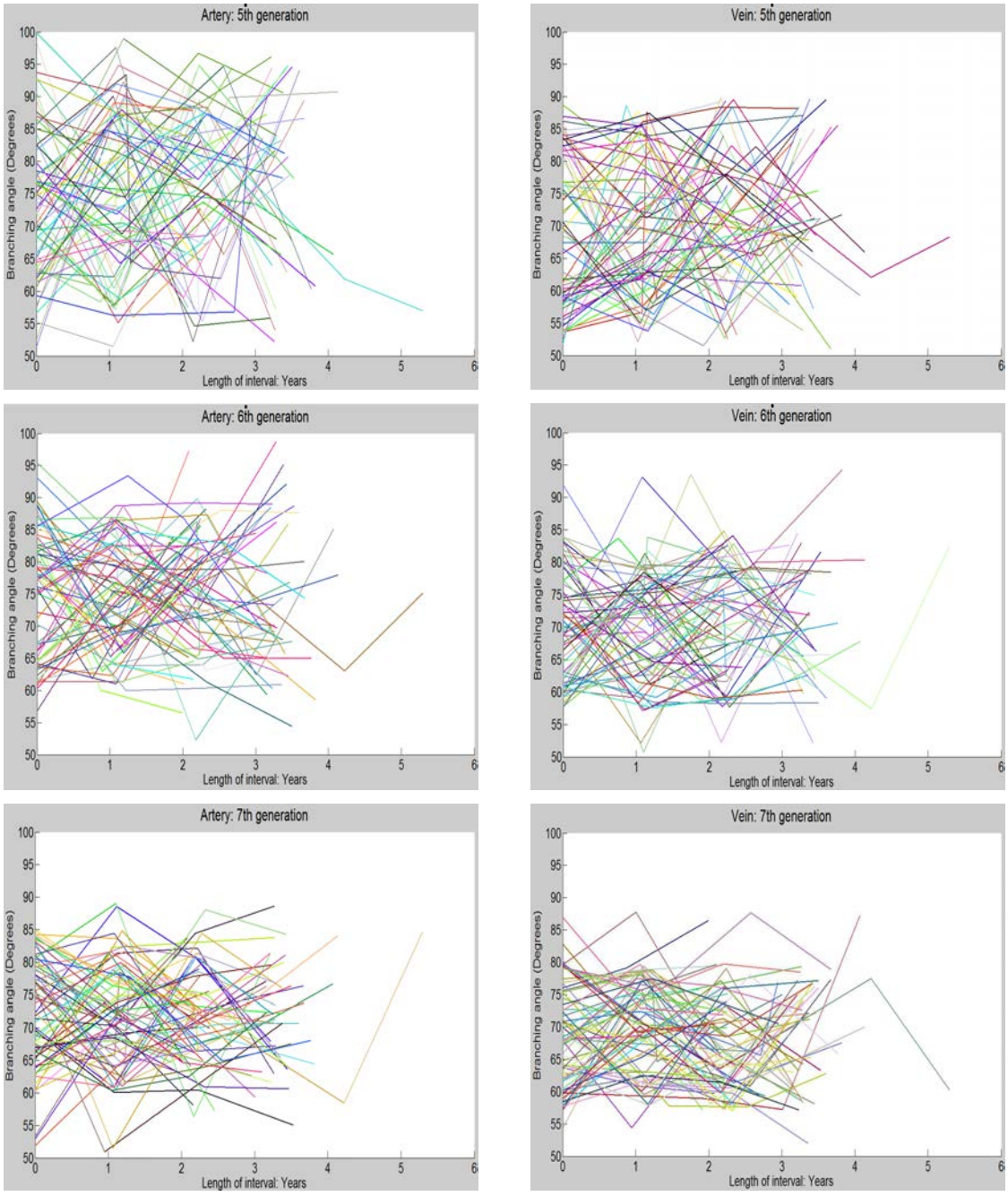


Figure A.10: Branching angle, X-axis: 0 to 6 years, Y-axis: 50 to 100 degrees

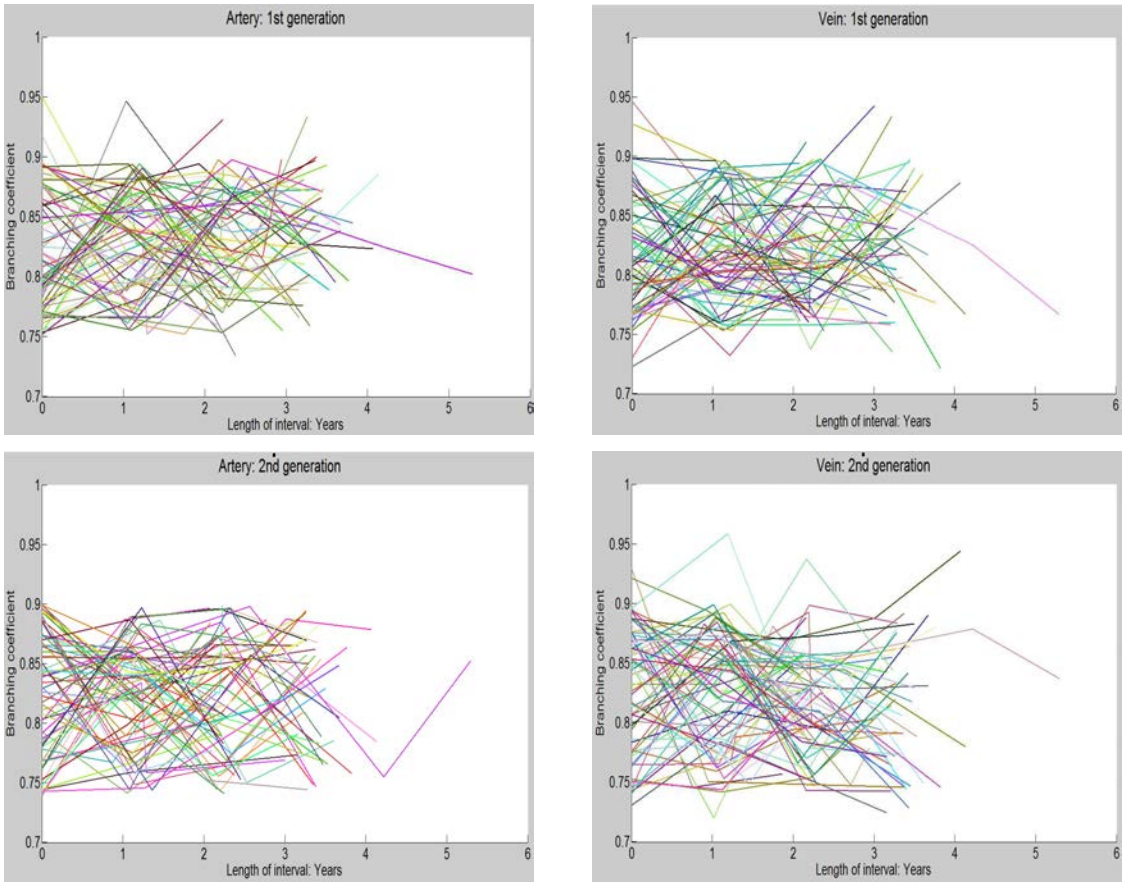


Figure A.11: Branching coefficient, X-axis: 0 to 6 years, Y-axis: 0.7 to 1

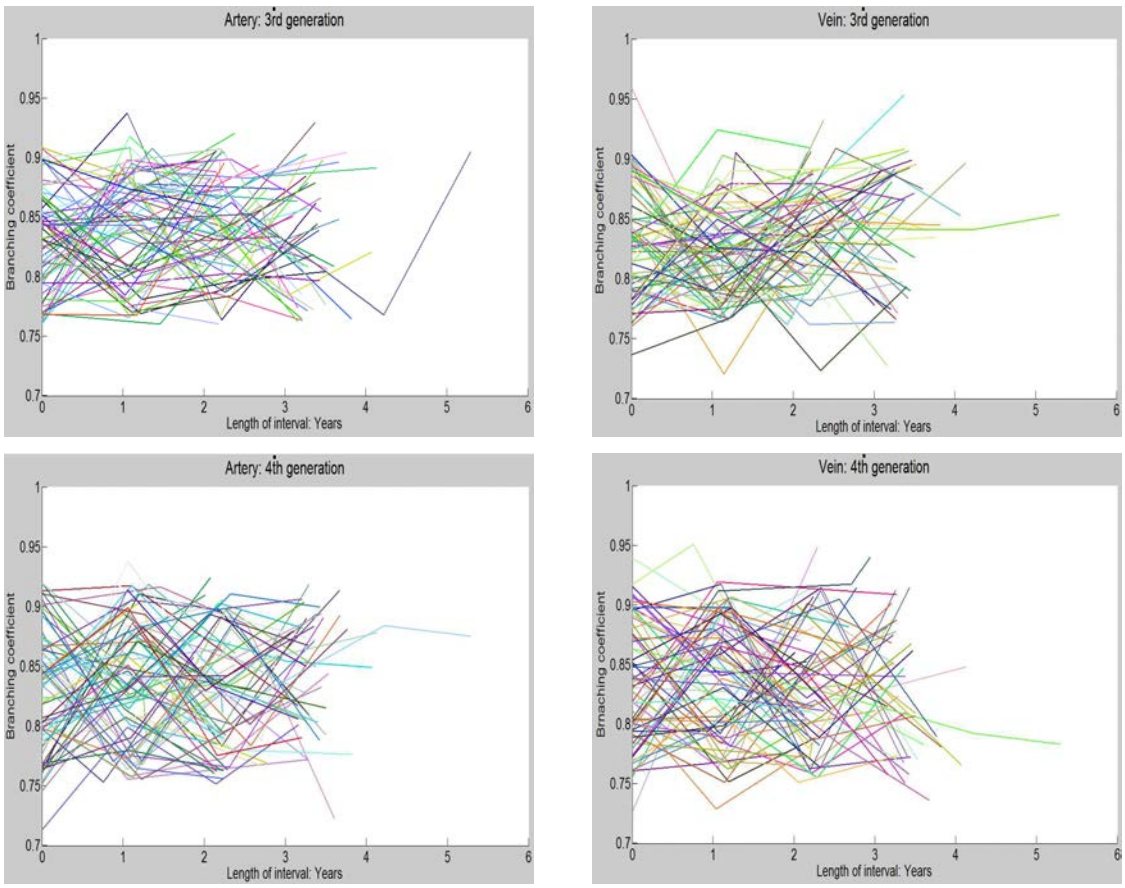


Figure A.12: Branching coefficient, X-axis: 0 to 6 years, Y-axis: 0.7 to 1

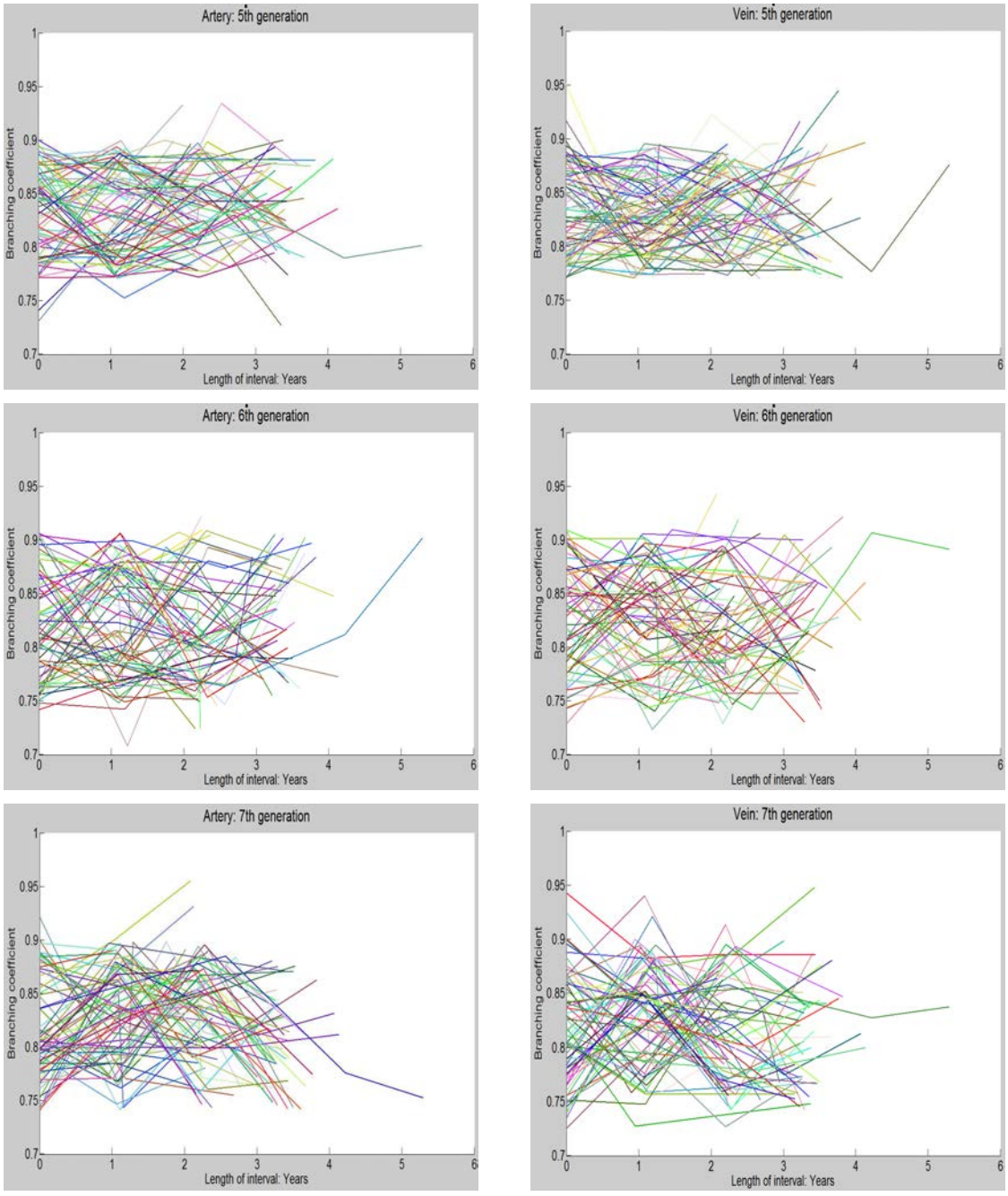


Figure A.13: Branching coefficient, X-axis: 0 to 6 years, Y-axis: 0.7 to 1

## REFERENCES

[1] Wikipedia - A free Encyclopedia. http://en.wikipedia.org/wiki/ (accessed December 25, 2011)

[2] The Bethesda Retina - http://www.bethesdaretina.com/library.htm (accessed December 25, 2011)

[3] EMedicine Health - http://www.emedicinehealth.com/ (accessed December 25, 2011)

[4] Gariano, R., Gardner, T.: Retinal angiogenesis in development and disease. Nature **438**

[5] Beare, N., Harding, S., Taylor, T.: Perfusion abnormalities in children with cerebral malaria and malarial retinopathy. J Infect Dis. **199**(2) (January 2009) 263–71

[6] Beare, N., Taylor, T., Harding, S.: Malarial retinopathy: a newly established diagnostic sign in severe malaria. AM. J. Trop. Med. Hyg. **75**(5) (2006) 790–797

[7] Massachussets eye/ear infirmary - http://www.masseyeandear.org/ (accessed December 25, 2011)

[8] Abramoff, M., Suttorp-Schulten, M.: Web-based screening for diabetic retinopathy in a primary care population: The eyecheck project. Telemedicine and e-Health **11(6)** (2005) 668–674

[9] Zamir, M., Medeiros, J., Cunningham, T.: Arterial bifurcations in the human retina. J. Gen. Physiol. **74** (1979) 537–548

[10] Sasongko, M., Wang, J., Donaghue, K., Cheung, N.: Alterations in retinal microvascular geometry in young type 1 diabetes. Diabetes Care. **33(6)** (2010) 1331–6

[11] Cheng, S., Huang, Y.: A novel approach to diagnose diabetes based on the fractal characteristics of retinal images. IEEE Trans Inf Technol Biomed. **7**(3) (September 2003) 163–70

[12] Christopher, M., Moga, D., Russell, S., Folk, J., Scheetz, T., Abrmoff, M.: Validation of tablet-based evaluation of color fundus images. Retina

[13] VisionRX - http://www.visionrx.com/Library/ (accessed December 25, 2011)

[14] The organization of the retina and the visual system - Simple Anatomy of the Retina. http://webvision.med.utah.edu/sretina.html (accessed December 25, 2011)

[15] Liew, G., Wang, J., Mitchell, P., Wong, T.: Retinal vascular imaging, a new tool in microvascular disease research. Circulation: Cardiovascular imaging **1**

[16] Joussen, A., Gardner, T., Kirchhof, B., Ryan, S.: Retinal vascular diseases. Springer (2007)

[17] The my eye world - http://www.myeyeworld.com/files/ (accessed December 25, 2011)

[18] Medline Plus Information - http://www.nlm.nih.gov/medlineplus/ency/ (accessed December 25, 2011)

[19] Lewallen, S., Bakker, H., Taylor, T.: Retinal findings predictive of outcome in cerebral malaria. Trans. R. Soc. Trop. Med. Hyg. **90**(2) (March 1996) 144–146

[20] Beare, N.: Prognostic significance and course of retinopathy in children with severe malaria. FRCOphth **122**(8) (August 2004)

[21] Birbeck, G., Beare, N., Lewallen, S.: Identification of malaria retinopathy improves the specificity of the clinical diagnosis of cerebral malaria: Findings from a prospective cohort study. Am. J. Trop. Med. Hyg. **82**(2) (2010) 231–234

[22] White, V., Lewallen, S., Beare, N.: Retinal pathology of pediatric cerebral malaria in malawi. PLoS One. **4**(1) (2009) e4317

[23] Lewallen, S., Bronzan, R., Beare, N.: Using malarial retinopathy to improve the classification of children with cerebral malaria. Trans. R. Soc. Trop. Med. Hyg. **102**(11) (November 2008) 1089–1094

[24] Essuman, V., Ntim-Amponsah, C., Astrup, B.: Retinopathy in severe malaria in ghanaian children–overlap between fundus changes in cerebral and non-cerebral malaria. Malar J. **12;9:232** (2010)

[25] White, V., Lewallen, S., Beare, N.: Correlation of retinal haemorrhages with brain haemorrhages in children dying of cerebral malaria in malawi. Trans. R. Soc. Trop. Med. Hyg. **95**(6) (Nov-Dec 2001) 618–21

[26] Lewallen, S., Harding, S., Ajewole, J.: A review of the spectrum of clinical ocular fundus findings in p. falciparum malaria in african children with a proposed classification and grading system. Trans. R. Soc. Trop. Med. Hyg. **93**(6) (November 1999) 619–622

[27] Project, B.M., Trust, M.L.W.: The eyes have it: findings in the optic fundus correspond to cerebral pathology in fatal malaria. Malawi Med J. **14**(1) (2002) 19–21

[28] Schmann, J., Doumbo, O., Malvy, D.: Ocular lesions associated with malaria in children in mali. Am J Trop Med Hyg. **67**(1) (July 2002) 61–3

[29] Beare, N., Glover, S.: Images in clinical tropical medicine: Malarial retinopathy in cerebral malaria. Am. J. Trop. Med. Hyg. **80**(2) (2009) 171

[30] Heneghan, C., Flynn, J., O'Keefe, M., Cahill, M.: Characterization of changes in blood vessel width and tortuosity in retinopathy of prematurity using image analysis. Medical Image Analysis **6** (2002) 407–429

[31] Niemeijer, M., Abrmoff, M., Ginneken, B.: Image structure clustering for image quality verification of color retina images in diabetic retinopathy screening. Medical Image Analysis **10**(6) (December 2006) 888–898

[32] Niemeijer, M., Abrmoff, M., Ginneken, B.: Segmentation of the optic disc, macula and vascular arch in fundus photographs. IEEE TMI **26**(1) (2007) 116–27

[33] Niemeijer, M., Staal, J., Ginneken, B., Loog, M., Abramoff, M.: Comparative study of retinal vessel segmentation methods on a new publicly available database. In: Proc. SPIE. Volume 5370. (2004) 648–656

[34] Abramoff, M., Niemeijer, M., Suttorp-Schulten, M.: Evaluation of a system for automatic detection of diabetic retinopathy from color fundus photographs in a large population of patients with diabetes. Diabetes Care **31**(2) (2008) 193–198

[35] Wilson, C., Cocker, K., Moseley, M.: Computerized analysis of retinal vessel width and tortuosity in premature infants. Invest Ophthalmol Vis Sci. **49**(8) (August 2008) 3577–85

[36] Sopharak, A., Uyyanonvara, B.: Automatic detection of diabetic retinopathy exudates from non-dilated retinal images using mathematical morphology methods. Computerized Medical Imaging and Graphics **32**

[37] Sinthanayothin, C., Boyce, J., Cook, H., Williamson, T.: Automated localization of the optic disc, fovea, and retinal blood vessels from digital colour fundus images. Br J Ophthalmol **83**

[38] Niemeijer, M., Ginneken, B., Staal, J., Suttorp-Schulten, M., Abrmoff, M.: Automatic detection of red lesions in digital color fundus photographs. IEEE transactions on medical imaging **24**(5) (May 2005)

[39] Spencer, T., Olson, J., McHardy, K., Sharp, P., Forrester, J.: An image processing strategy for the segmentation and quantification of microaneurysms in fluorescein angiograms of the ocular fundus. Comput. Biomed. Res. **29**

[40] Cree, M., Olson, J., McHardy, K., Sharp, P., Forrester, J.: The preprocessing of retinal images for the detection of fluorescein leakage. Phys. Med. Biol. **44**(1) (1999) 293–308

[41] Hoover, A., Goldbaum, M.: Locating the optic nerve in a retinal image using the fuzzy convergence of the blood vessels. IEEE Trans. Med. Imag. **22(8)** (2003) 951958

[42] Sukkaew, L., Makhanov, B., Barman, S., Panguthipong, S.: Automatic tortuosity-based retinopathy of prematurity screening system. IEICE transactions on information and systems **12**

[43] Wen, Y., Smith, A., Morris, A.: Automated assessment of diabetic retinal image quality based on blood vessel detection. In: Proceedings of Image and Vision Computing. (2007) 132–136

[44] Lalonde, M., Gagnon, L., Boucher, M.: Automatic visual quality assessment in optical fundus images. In: Proceedings of Vision Interface. (2001) 259–264

[45] Fleming, A., Philip, S., Goatman, K., Olson, J., Sharp, P.: Automated assessment of diabetic retinal image quality based on clarity and field definition. Investigative Ophthalmology and Visual Science **47**(3) (March 2006)

[46] Chaudhuri, A., Chatterjee, S., Katz, N., Nelson, M., Goldbaum, M.: Detection of blood vessels in retinal images using two-dimensional matched filters. IEEE Transactions on Medical Imaging **3**

[47] Martinez-Perez, M., Hughes, A., Stanton, A., Thom, S.: Retinal blood vessel segmentation by means of scale-space analysis and region growing. Medical Image Computing and Computer-Assisted Intervention (MICCAI'99) **1679** (1999) 90–97

[48] Gardner, G., Keating, D., Williamson, T., Elliott, A.: Automatic detection of diabetic retinopathy using an artificial neural network: a screening tool. British Journal of Ophthalmology **80**

[49] Staal, J., Abrmoff, M., Niemeijer, M., Viergever, M., Ginneken, B.: Ridge-based vessel segmentation in color images of the retina. IEEE transactions on medical imaging **23(4)** (2004)

[50] Zana, F., Klein, J.: Segmentation of vessel-like patterns using mathematical morphology and curvature evaluation. IEEE transactions on image processing **10(7)** (2001)

[51] Mendonca, A., Campilho, A.: Segmentation of retinal blood vessels by combining the detection of centerlines and morphological reconstruction. IEEE Trans. On Medical Imaging **25(9)** (2006) 1200–13

[52] Jiang, Y., Bainbridge-Smith, A., Morris, A.: Blood vessel tracking in retinal images. In: Proceedings of Image and Vision Computing. (2007) 126–131

[53] Lalonde, M., Gagnon, L., Boucher, M.: Non-recursive paired tracking for vessel extraction from retinal images. In: Proceedings of the Conference Vision Interface. (2000) 61–68

[54] Cree, M., Cornforth, D., Jelinek, H.: Vessel segmentation and tracking using a two-dimensional model. In: IVC New Zealand (2005) 345–350

[55] Kochner, B., Schuhmann, D., Michaelis, M.: Course tracking and contour extraction of retinal vessels from color fundus photographs: most efficient use of steerable filters for model-based image analysis. In: Proceedings Medical Imaging: Image Processing. Volume 3338. (1998) 755–761

[56] Grisan, E., Pesce, A., Giani, A., Foracchia, M., Ruggeri, A.: A new tracking system for the robust extraction of retinal vessel structure. In: Conf Proc IEEE Eng Med Biol Soc. Volume 3. (2004) 1620–3

[57] Joshi, V., Garvin, M., Reinhardt, J., Abramoff, M.: Identification and reconnection of interrupted vessels in retinal vessel segmentation. In: IEEE, ISBI, Image Segmentation Methods. Volume FR-PS3a.7. (2011) 1416–1420

[58] Koreen, S., Gelman, R., Martinez-Perez, M.: Evaluation of a computer-based system for plus disease diagnosis in retinopathy of prematurity. Ophthalmology **114(12)** (2007) e59–e67

[59] Joshi, V., Reinhardt, J., Garvin, M., Abramoff, M.: Automated method for identification and artery-venous classification of vessel trees in retinal vessel networks. Submitted to IEEE Transactions on Medical Imaging

[60] : Grading diabetic retinopathy from stereoscopic color fundus photographs, an extension of the modified airlie house classification. Ophthalmology **98**

[61] Davis, M., Bressler, S., Aiello, L., Bressler, N., Browning, D., Flaxel, C.: Comparison of time-domain oct and fundus photographic assessments of retinal thickening in eyes with diabetic macular edema. Invest Ophthalmol Vis Sci **49**

[62] Walter, T., Klein, J., Massin, P., Erginay, A.: A contribution of image processing to the diagnosis of diabetic retinopathy-detection of exudates in color fundus images of the human retina. IEEE transactions on medical imaging **21**(10) (october 2002)

[63] Fleming, A., Goatman, K., Philip, S., Olson, J., Sharp, P.: Automatic detection of retinal anatomy to assist diabetic retinopathy screening. Phys. Med. Biol. **52**

[64] Pinz, A., Bernogger, S., Datlinger, P., Kruger, A.: Mapping the human retina. IEEE transactions on medical imaging **17**(4) (August 1998)

[65] Foracchia, M., Grisan, E., Ruggeri, A.: Detection of optic disc in retinal images by means of a geometrical model of vessel structure. IEEE transactions on medical imaging **23**(10) (2004)

[66] Abrmoff, M., Niemeijer, M.: The automatic detection of the optic disc location in retinal images using optic disc location regression. In: Conf Proc IEEE Eng Med Biol Soc. (2006) 4432–4435

[67] M.Larsen, Godt, J., Larsen, N., Andersen, H.: Automated detection of fundus photographic red lesions in diabetic retinopathy. Inv Ophthalmology and Visual Science **44**

[68] Sinthanayothin, C., Boyce, J., Williamson, T.: Automated detection of diabetic retinopathy on digital fundus images. Diabet Med. **19**(2) (February 2002) 105–12

[69] N.Larsen, J.Godt, Grunkin, M., Andersen, H., Larsen, M.: Automated detection of diabetic retinopathy in a fundus photographic screening population. Investigative Ophthalmology and Visual Science **44**

[70] Spencer, T., Phillips, R., Sharp, P., Forrester, J.: Automated detection and quantification of microaneurysms in fluorescein angiograms. Graefe's Arch Clin Exp Ophthalmol **230**

[71] Cree, M., Olson, J., McHardy, K., Sharp, P., Forrester, J.: A fully automated comparative microaneurysm digital detection system. Eye **11**

[72] Kylstra, J., Wierzbicki, T., Wolbarsht, M.: The relationship between retinal vessel tortuosity, diameter, and transmural pressure. Graefes Arch Clin Exp Ophthalmol **224**(5) (1986) 477–80

[73] Patasius, M., Marozas, V., Lukosevicius, A., Jegelevicius, D.: Model based investigation of retinal vessel tortuosity as a function of blood pressure: preliminary results. In: Proceedings of the 29th Annual International Conference of the IEEE EMBS. (2007) 6459 – 6462

[74] Bedell, A.: Retinal vessel proliferation in diabetes. Trans Am Ophthalmol Soc **43**

[75] Pries, A., Reglin, B., Secomb, T.: Remodeling of blood vessels: responses of diameter and wall thickness to hemodynamic and metabolic stimuli. Hypertension **46**(4) (October 2005) 725–31

[76] Azegrouz, H., Trucco, E., Dhillon, B.: Thickness dependent tortuosity estimation for retinal blood vessels. In: Annual International Conference of the IEEE Engineering in Medicine and Biology Society. (2006) 4675–8

[77] Taarnhj, N., Munch, I., Sander, B.: Straight versus tortuous retinal arteries in relation to blood pressure and genetics. Br J Ophthalmol **92**

[78] Owen, C., Newsom, R., Rudnicka, A.: Diabetes and the tortuosity of vessels of the bulbar conjunctiva. Br J Ophthalmol **115**(6) (June 2008) e27–e32

[79] Dougherty, G., Johnson, M., Wiers, M.: Measurement of retinal vascular tortuosity and its application to retinal pathologies. Med Biol Eng Comput. **48**(1) (January 2010) 87–95

[80] Lim, L., Cheung, C., Lin, X.: Influence of refractive error and axial length on retinal vessel geometric characteristics. Invest. Ophthalmol. Vis. Sci. **10**

[81] Kristinsson, J., Gottfredsdottir, M., Stefansson, E.: Retinal vessel dilatation and elongation precedes diabetic macular oedema. Br J Ophthalmol. **81(4)** (1997) 274–278

[82] Wilson, C., Cocker, K., Moseley, M.: Computerized analysis of retinal vessel width and tortuosity in premature infants. Invest Ophthalmol Vis Sci. **49(8)** (2008) 3577–3585

[83] Capowski, J., Kylstra, J., Freedman, S.: A numeric index based on spatial frequency for the tortuosity of retinal vessels and its application to plus disease in retinopathy of prematurity. Retina **15(6)** (1995) 490–500

[84] Hart, W., Goldbaum, M., Ct, B., Kube, P.: Measurement and classification of retinal vascular tortuosity. Int. J. Med. Informatics **53**(2)

[85] Bullitt, E., Gerig, G., Pizer, S., Lin, W., Aylward, S.: Measuring tortuosity of the intracerebral vasculature from mra images. IEEE Trans Med Imaging. **22**(9) (2003) 1163–71

[86] Kaupp, A., Toonen, H., Wolf, S.: Automatic evaluation of retinal vessel width and tortuosity in digital fluorescein angiograms. Invest. Ophthalmol. Vis. Sci. **32(952)** (1991)

[87] Grisan, E., Foracchia, M., Ruggeri, A.: A novel method for the automatic grading of retinal vessel tortuosity. IEEE Transactions on Medical Imaging **27**(3) (March 2008) 310–319

[88] Chapman, N., Dell'omo, G., Sartini, M., Witt, N., Hughes, A., Thom, S., Pedrinelli, R.: Peripheral vascular disease is associated with abnormal arteriolar diameter relationships at bifurcations in the human retina. Clin Sci (Lond). **103(2)** (2002) 111–6

[89] Witt, N., Chapmana, N., Thom, S.: A novel measure to characterise optimality of diameter relationships at retinal vascular bifurcations. Artery Research **4**(3) (September 2010) 75–80

[90] Kifleya, A., Wanga, J., Cugatia, S.: Retinal vascular caliber, diabetes, and retinopathy. Am J Ophthalmol. **143**(6) (June 2007) 1024–1026

[91] Klein, R., Klein, B., Moss, S., Wong, T.: Retinal vessel caliber and microvascular and macrovascular disease in type 2 diabetes: Xxi: the wisconsin epidemiologic study of diabetic retinopathy. Ophthalmology **114**(10) (October 2007) 1884–92

[92] Zhou, P., Wang, M., Cao, H.: Research on features of retinal images associated with hypertension and diabetes. IEEE-EMBS 27th Annual International Conference

[93] Wang, X., Cao, H., Zhang, J.: Analysis of retinal images associated with hypertension and diabetes. In: Conf Proc IEEE Eng Med Biol Soc. (2005) 6407–10

[94] Brinchmann-Hansen, O., Heier, H.: Theoretical relations between light streak characteristics and optical properties of retinal vessels. Acta Ophthalmologica **64** (September 1986) 33–37

[95] Lowell, J., Hunter, A., Steel, D.: Measurement of retinal vessel widths from fundus images based on 2-d modeling. IEEE Trans Med Imaging. **23**(10) (October 2004) 1196–204

[96] Gregsona, P., Shen, Z., Scott, R., Kozousek, V.: Automated grading of venous beading. Computers and Biomedical Research **28**(4) (August 1995) 291–304

[97] Al-Diri, B., Hunter, A., Steel, D.: An active contour model for segmenting and measuring retinal vessels. IEEE Trans Med Imaging. **28**(9) (September 2009) 1488–97

[98] Xu, X., Neimeijer, M., Song, Q., Garvin, M., Reinhardt, J., Abramoff, M.: Retinal vessel width measurements based on a graph theoretic method. Biomedical Imaging: From Nano to Macro, 2011 IEEE International Symposium

[99] Martinez-Perez, M., Highes, A., Stanton, A.: Retinal vascular tree morphology: a semi-automatic quantification. Biomedical Engineering, IEEE Transactions **49**(8) (August 2002) 912–917

[100] Stanton, A., Wasan, B., Cerutti, A.: Vascular network changes in the retina with age and hypertension. J Hypertens. **13**(12)

[101] Vickerman, M., Keith, P., McKay, T., Gedeon, D.: Vesgen 2d: automated, user-interactive software for quantification and mapping of angiogenic and lymphangiogenic trees and networks. Anat Rec (Hoboken). **292**(3) (March 2009) 320–32

[102] Yau, J., Kawasaki, R., Islam, F.: Retinal fractal dimension is increased in persons with diabetes but not impaired glucose metabolism: the australian diabetes, obesity and lifestyle (ausdiab) study. Diabetologia **53**(9) (September 2010) 2042–5

[103] Zamir, M.: Nonsymmetrical bifurcations in arterial branching. The Journal of General Physiology **72**(6) (December 1978) 837–845

[104] Witt, N., Wong, T., Hughes, A.: Abnormalities of retinal microvascular structure and risk of mortality from ischemic heart disease and stroke. Hypertension **47(5)** (2006) 975–981

[105] Grauslund, J., Green, A., Kawasaki, R.: Retinal vascular fractals and microvascular and macrovascular complications in type 1 diabetes. Ophthalmology **117**(7) (July 2010) 1400–5

[106] Cheung, N., Donaghue, K., Liew, G.: Quantitative assessment of early diabetic retinopathy using fractal analysis. Diabetes Care. **32**(1) (January 2009) 106–110

[107] Daxer, A.: The fractal geometry of proliferative diabetic retinopathy: implications for the diagnosis and the process of retinal vasculogenesis. Current Eye Research **12**

[108] Daxer, A.: Characterisation of the neovascularisation process in diabetic retinopathy by means of fractal geometry: diagnostic implications. Graefes Arch Clin Exp Ophthalmol. **231**(12) (December 1993) 681–6

[109] Avakian, A., Kalina, R., Sage, E.: Fractal analysis of region-based vascular change in the normal and non-proliferative diabetic retina. Curr Eye Res. **24**(4) (April 2002) 274–80

[110] Stosic, T., Stosic, B.: Multifractal analysis of human retinal vessels. IEEE Trans Med Imaging. **25**(8) (August 2006) 1101–7

[111] Niemeijer, M., Ginneken, B., Abramoff, M.: A linking framework for pixel classification based retinal vessel segmentation. Proc. SPIE **7262** (2009)

[112] Joshi, V., Reinhardt, J., Abramoff, M.: Automated measurement of retinal blood vessel tortuosity. In: Proc. SPIE Medical Imaging, Computer-Aided Diagnosis. Volume 7624, 76243A. (2010)

[113] Joshi, V., Maude, R., Reinhardt, J., Tang, L., Garvin, M., Abramoff, M.: Automated detection of malarial retinopathy associated retinal hemorrhages. Submitted to Investigative ophthalmology and Visual science (2012)

[114] Niemeijer, M., Xu, X., Dumitrescu, A., Gupta, P., Ginneken, B., Folk, J., Abramoff, M.: Automated measurement of the arteriolar-to-venular width ratio in digital color fundus photographs. IEEE Transactions on Medical Imaging **30(11)** (2011) 1941 – 1950

[115] Forkert, N., Richberg, A., Saring, D.: Closing of interrupted vascular segmentations: An automatic approach based on shortest paths and level sets. Proc. SPIE **7623** (2010)

[116] Otsu, N.: A threshold selection method from gray-level histograms. IEEE Trans. Sys., Man., Cyber. **9(1)** (1979) 6266

[117] Rockett, P.: An improved rotation-invariant thinning algorithm. IEEE Trans. Pattern Anal. Mach. Intell. **27**(10) (Oct 2005) 16711674

[118] Vickerman, M., Keith, P., Mckay, T.: Vesgen 2d: Automated, user-interactive software for quantification and mapping of angiogenic and lymphangiogenic trees and networks. The Anatomical record **292**

[119] Aylward, S., Jomier, J., Vivert, C.: Spatial graphs for intra-cranial vascular network characterization, generation, and discrimination. Med Image Comput Comput Assist Interv **3749(1)** (2005) 59–66

[120] Rothaus, K., Jiang, X., Rhiem, P.: Separation of the retinal vascular graph in arteries and veins based upon structural knowledge. Image and Vision Computing **27(7)** (2009) 864–875

[121] Tramontan, L., Grisan, E., , Ruggeri, A.: An improved system for the automatic estimation of the arteriolar-to-venular diameter ratio (avr) in retinal images. In: Proc. 30th Annual International Conference of the IEEE Engineering in Medicine and Biology Society EMBS. (2008) 3550–3553

[122] Grisan, E., Ruggeri, A.: A divide et impera strategy for automatic classification of retinal vessels into arteries and veins. In: Proceedings of the 25th Annual International Conference of the IEEE. Volume 1. (2003) 890–893

[123] Vazquez, S.G., Barreira, N., Penedo, M.G., Ortega, M., Pose-Reino, A.: Improvements in retinal vessel clustering techniques: Towards the automatic computation of the arterio venous ratio. In: Computing. Volume 90(34). (2010) 197217

[124] Kondermann, C., Kondermann, D., Yan, M.: Blood vessel classification into arteries and veins in retinal images. In: Med. Imag. Image Process. Volume 6512. (2007) 651247651249

[125] Lee, S., Reinhardt, J., Abrmoff, M.: Retinal image mosaicing using the radial distortion correction model. In: SPIE Proceedings, Medical Imaging. (2008) 6914

[126] Sun, Y.: Knowledge-based segmentation and correspondence of vascular structures from biplane angiograms. In: SPIE Proceedings, Medical Imaging, Newport Beach, CA, USA (1990) 1233: 257

[127] Zhou, L., Rzeszotarski, M., Singerman, L., Chokreff, J.: The detection and quantification of retinopathy using digital angiograms. IEEE Trans Med Imaging **13**(4) (December 1994) 619–26

[128] Faber, D., Aalders, M., Mik, E.: Oxygen saturation-dependent absorption and scattering of blood volume. Physical review letters **93**(2) (2004)

[129] Abramoff, M., Niemeijer, M., Suttorp-Schulten, M., Viergever, M., Russell, S., van Ginneken, B.: Evaluation of a system for automatic detection of diabetic retinopathy from color fundus photographs in a large population of patients with diabetes. Diabetes Care **31**(2) (Feb 2008) 193– 198

[130] Al-Diri, B., Hunter, A., Steel, D., Habib, M.: Joining retinal vessel segments. The 8th IEEE International Conference on BioInformatics and BioEngineering

[131] Joshi, V., Garvin, M., Reinhardt, J., Abramoff, M.: Automated method for the identification and analysis of vascular tree structures in retinal vessel network. In: Proc. SPIE Medical Imaging, Computer-Aided Diagnosis. Volume 7963, 79630I. (2011)

[132] Joshi, V., Garvin, M., Reinhardt, J., Abramoff, M.: Automated artery-venous classification of retinal blood vessels based on structural mapping method. In: SPIE Proceedings and conference, Medical Imaging. Volume 8315, 83150I., San Diego, USA (2012)

[133] Wolffsohn, J., Napper, G., Ho, S.: Improving the description of the retinal vasculature and patient history taking for monitoring systemic hypertension. Ophthalmic Physiol. Opt. **21**(6) (November 2001) 441–449

[134] Lotmar, W., Freiburghaus, A., Bracher, D.: Measurement of vessel tortuosity on fundus photographs. Exp Ophthalmol. **211**(1) (1979) 49 –57

[135] Martinez-Perez, M., Hughes, A., Thom, A., Bharath, A., Parker, K.: Segmentation of blood vessels from red-free and fluorescein retinal images. Medical Image Analysis **11**

[136] Li, Q., You, J., Zhang, L., Zhang, D.: A new approach to automated retinal vessel segmentation using multiscale analysis. The 18th International Conference on Pattern Recognition

[137] Longmuir, S., Mathews, K., Longmuir, R., Joshi, V., Olson, R., Abramoff, M.: Retinal arterial but not venous tortuosity correlates with facioscapulohumeral muscular dystrophy (fshd) severity. Journal of American Association for Pediatric Ophthalmology and Strabismus **13**(1) (2009) e21

[138] Bracher, D.: Changes in peripapillary tortuosity of the central retinal arteries in newborns. Graefe's Arch. Clin. Exp. Opthalmol. **218**

[139] Goldbaum, M., Hart, W., Raphaelian, B.C.P.: Automated measures of retinal blood vessel tortuosity. Invest. Opthalmol. Vis. Sci. **35**

[140] Zhou, L., Rzeszotarski, M., Singerman, L., Chokreff, J.: The detection and quantification of retinopathy using digital angiograms. IEEE-TMI **13**

[141] Wallace, D., Zhao, Z., Freedman, S.: A pilot study using roptool to quantify plus disease in retinopathy of prematurity. Journal of American Association for Pediatric Ophthalmology and Strabismus **11(4)** (2007) 381–387

[142] Saunders, R., Donahue, M., Berland, J.: Non-ophthalmologist screening for retinopathy of prematurity. Br J Ophthalmol **84** (2000) 130–134

[143] Smedby, O., Hogman, N., Nilsson, S., Erikson, U., Olsson, A., Walldius, G.: Two-dimensional tortuosity of the superficial femoral artery in early atherosclerosis. J.Vascular Research **30**

[144] Kochar, D., Shubhakaran, Kumawat, B.: Ophthalmoscopic abnormalities in adults with falciparum malaria. QJM: An International Journal of Medicine **91**(12) (December 1998) 845–52

[145] Maude, R., Beare, N., Sayeed, A.: The spectrum of retinopathy in adults with plasmodium falciparum malaria. Trans R Soc Trop Med Hyg. **103**(7) (July 2009) 665–71

[146] Molyneux, M., Taylor, T., Wirima, J., Borgsteinj, A.: Clinical features and prognostic indicators in paediatric cerebral malaria: A study of 131 comatose malawian children. Quarterly International Journal of Medicine **71**(2) (December 1988) 441–459

[147] Tang, L., Niemeijer, M., Abrmoff, M.: Splat feature classification: Detection of the presence of large retinal hemorrhages. In: In Proceedings of ISBI, Chicago, USA (2011) 681–684

[148] Niemeijer, M., Ginneken, B., Abrmoff, M.: Automated detection and differentiation of drusen, exudates, and cotton-wool spots in digital color fundus photographs for diabetic retinopathy diagnosis. Investigative Ophthalmology and Visual Science **48**

[149] Xu, X., Niemeijer, M., Song, Q., Sonka, M., Garvin, M., Reinhardt, J., Abrmoff, M.: Vessel boundary delineation on fundus images using graph-based approach. IEEE Trans Med Imaging. **30**(6) (June 2011) 1184–1191

[150] Mortensen, E.: Simultaneous multi-frame subpixel boundary definition using Toboggan-based intelligent scissors for image and movie editing. PhD thesis, Brigham Young Univ, Provo, UT (2000)

[151] Lin, Y., Tsai, Y., Hung, Y., Shih, Z.: Comparison between immersion-based and toboggan-based watershed image segmentation. Image Processing, IEEE Transactions **15**(3) (March 2006) 632–640

[152] Parvati, K., Rao, B., Das, M.: Image segmentation using gray-scale morphology and marker-controlled watershed transformation. Discrete Dynamics in Nature and Society

[153] Cover, T., Hart, P.: Nearest neighbor pattern classification. IEEE Trans. Inform. Theory **13**(1) (1967) 21–27

[154] E. Fix, J.H.: Discriminatory analysis, nonparametric discrimination: Consistency properties, technical report 4. USAF School of Aviation Medicine

[155] J. Eng: ROC analysis: web-based calculator for ROC curves. Hypertext Document (May 2006)

[156] Park, S., Goo, J., Jo, C.: Receiver operating characteristic (roc) curve: Practical review for radiologists. Korean J Radiol. **5**(1) (Jan-Mar 2004) 11–18

[157] Maude, R., Dondorp, A., Sayeed, A.: The eye in cerebral malaria: what can it teach us? Trans R Soc Trop Med Hyg. **103**(7) (July 2009) 661–4

[158] Stolov, W.C., ed.: Handbook of severe disability. U.S. Department of education, Washington, DC (1981)

[159] Dijkstra, E.: A note on two problems in connexion with graphs. Numerische Mathematik **1**

[160] Dunn, J.C.: A fuzzy relative of the isodata process and its use in detecting compact well-separated clusters. Journal of Cybernetics **3**

[161] Bezdek, J.C., ed.: Pattern Recognition with Fuzzy Objective Function Algoritms. Plenum Press, New York (1981)